IMAGE DENOISING AND IMAGE ENHANCEMENT ON THE APPLICATIONS OF CONFOCAL LASER SCANNING MICROSCOPY

by

Yunus Engin Gökdağ

B. Sc., Electrical and Electronics Engineering, Hacettepe University, 2010

Submitted to the Institute of Biomedical Engineering
in partial fulfillment of the requirements
for the degree of
Master of Science
in
Biomedical Engineering

Boğaziçi University
2016

ACKNOWLEDGMENTS

There are a number of people without whom and without their support and encouragement this thesis could not have been possible. Firstly, I would like to offer my sincere gratitude and appreciation to Dr. Yiğit Dağhan Gökdel for his guidance, ethusiasm and patience he has provided throughout this study. Dr. Gökdel's insights into and patient endurance throughout this project have been a true blessing. I feel very lucky to be a member of his Micro-Systems Lab since the very beginning of my master's study. I would also like to thank my thesis advisor Dr. Özgür Kocatürk for his discerning comments, recommendations and benevolently providing the conveniences to be graduated. Besides my advisors, Dr. Ata Akın is the other mentor and the milestone of my academic life. I can't thank him enough for his inspirational ideas and persuasion to continue in academy.

I am thankful to my dearest friend Fırat Şansal for being as a great brother since I first came to Istanbul. The Force in him has always made me confident on both my real and academic life. I couldn't have imagine this research period without him. I would like to thank my other dearest friend Ayşegül Tümer for never ending friendship and her assistance in thesis writing.

I should thank my labmates Mert Aktürk who has also made a lot of effort on gathering image data and Hilal Kızılcabel for the order she has restored in our lab every time. I also want to thank all Micro-Systems Lab members.

Lastly, I have my special appreciation to the most important person in my life, my mother Dilek Aksümer for her trust on my choices and her endless love. She has always supported me not only during my academic life but throughout my life. She is the perfect love, patience, and gift that are the real strength behind all my accomplishments.

This work was sponsored in part by TUBITAK Project No's: 113S114.

ACADEMIC ETHICS AND INTEGRITY STATEMENT

I, Yunus Engin Gökdağ, hereby certify that I am aware of the Academic Ethics and Integrity Policy issued by the Council of Higher Education (YÖK) and I fully acknowledge all the consequences due to its violation by plagiarism or any other way.

Name : Signature:

_____ _____

Date:

_____

ABSTRACT

IMAGE DENOISING AND IMAGE ENHANCEMENT ON THE APPLICATIONS OF CONFOCAL LASER SCANNING MICROSCOPY

Confocal laser scanning microscopy (CLSM) is a developing optical imaging device enabling non-invasive examination of live biological tissues with laser light in real-time. CLSM provides optical sectioning of samples. Image can get corrupted with noise of different levels due to out-of-focus light back-scattered above and below the focal plane. Construction of the CLSM setup is established and several images are captured. This work attempts to analyze the effects of different denoising and contrast enhancement techniques by using real CLSM images with the help of different image quality metrics. Additive white Gaussian noise (AWGN) is used as a noise model. A reliable method for estimating the standard deviation of AWGN in a single image is also performed on real CLSM images. Wavelet transform is the most effective candidate for noise suppression since it is capable of preserving energy conservation during inverse transformation. A denoising algorithm is developed to make it applicable on CLSM. An important issue that affects the performance of 2D-DWT is the selection of components employed in the algorithm along with their parameter selection. This study examines the effect of employing different combinations of 2D-DWT components and tuning parameter values on different image quality assessments. Design of Experiments (DOE) is presented as a systematic approach to catch the best combination of these parameter values. Analysis of variance (ANOVA) is used to inspect the main effect and interaction effects of the treated parameters. Computational results verified the efficacy of the proposed algorithm and the methodical approach for the image denoising of CLSM images. After denoising, several histogram equalization methods are put into practice for contrast enhancement. The comparison of methods that give better enhancement result is provided with the means of different quantative measures for better visualization.

Keywords: confocal microscopy, denoising, wavelet, thresholding, contrast enhancement, histogram equalization, noise estimation, image quality, design of experiments.

ÖZET

LAZER TARAMALI KONFOKAL MİKROSKOP UYGULAMALARINDA GÖRÜNTÜ GÜRÜLTÜSÜNÜN GİDERİMİ VE GÖRÜNTÜ İYİLEŞTİRİMİ

Lazer taramalı konfokal mikroskobu (LTKM) lazer ışını ile biyolojik canlı dokuların gerçek zamanlı ve non-invaziv incelemesini sağlayan gelişmekte olan bir optik görüntüleme cihazıdır. LTKM örnek dokuların optik kesitlemesini sağlar. Alınan görüntüler odak düzleminin altından veya üstünden geri yansıyan odak dışı ışınlardan kaynaklı çeşitli seviyelerde gürültüye maruz kalır. Bu çalışmada LTKM optik düzeneğinin kurulumu yapılmış ve birtakım görüntüler elde edilmiştir. Gerçek LTKM görüntüleri kullanılarak farklı gürültü giderimi ve kontrast iyiliştirimi tekniklerinin etkileri, farklı görüntü kalite ölçüleri altında incelenmiştir. Gürültü modeli olarak eklenebilir beyaz Gauss gürültüsü (EBGG) kullanılmıştır. EBGG'nin standart sapmasının tek bir görüntüyü kullanarak kestirilmesinde güvenilir bir yöntem gerçek LTKM görüntülerinde kullanılmıştır. Ters dönüşümde sağladığı enerji korunumundan dolayı dalgacık dönüşümü gürültü gideriminde en etkili adaydır. LTKM'de uygulanmak üzere bir gürültü giderimi algoritması geliştirilmiştir. Algoritmada kullanılan parametre bileşenlerinin seçimi iki boyutlu ayrık dalgacık dönüşümünün (2B-ADD) performansını etkileyen önemli bir husustur. Bu çalışmada kullanılan 2B-ADD bileşenlerinin ve uyarlanan parametrelerin farklı kombinasyonlarının etkileri, farklı görüntü kalite değerlendirmeleri altında incelenmiştir. Deney Tasarımı (DT), bu en iyi parametre kombinasyonlarını bulmak için sistematik bir yaklaşım olarak sunulmuştur. Varyans analizi (VA) ile işleme alınan parametrelerin temel etkisi ve etkileşim etkileri incelenmiştir. Hesaplama sonuçları önerilen algoritmanın ve LTKM görüntü gürültülerinin giderilmesinde kullanılan düzenli yaklaşımın etkinliğini ortaya koymuştur. Gürültü gideriminden sonra kontrast iyileştirimi amacıyla çeşitli histogram eşitleme teknikleri uygulanmıştır. Farklı nicel ölçümler vasıtasıyla daha iyi iyileştirme sonucunu veren yöntemlerin karşılaştırılması yapılmıştır.

Anahtar Sözcükler: konfokal mikroskop, gürültü giderimi, dalgacık, eşikleme, kontrast iyiliştirimi, histogram eşitleme, gürültü kestirimi, görüntü kalitesi, deney tasarımı.

TABLE OF CONTENTS

LIST OF FIGURES

LIST OF TABLES

LIST OF SYMBOLS

C_ψ	Admissibility constant
J	Wavelet Decomposition Level
L	The dynamic range of pixel intensities
N_0	The number of coefficients under threshold
N_w	Number of pixels in window
R	Coherence
T	Sampling period
$T_{L,U}$	Lower and Upper Histogram clip limit
X_G	The middle gray level of all grayscale
X_m	The mean brightness of the input image
X_T	Gray level Threshold
$c_{X,Y}$	The local contrast values of the original and enhanced image
$d_{a,b}$	Analysis coefficient
e_{ij}	Edge Value
$g_{x_{i,j}}$	Gradient component
p_k	Probability of pixels
s_{ij}	The local standard deviation
w_{ij}	Window size
$\hat{x}$	Estimation of x
x_{ij}	Clean image
y_{ij}	Noisy image
Γ	Gamma Function
α	Scale parameter of CWT
β	Shape parameter
δ	Threshold value or Significance parameter
η	Thresholding function
μ	Mean
σ	The standard deviation

$\hat{\sigma}$	Estimated noise standard deviation
τ	Translation parameter of CWT or threshold
ψ	The mother wavelet
ω	Wavelet coefficients

LIST OF ABBREVIATIONS

2D-DWT	Two Dimensional Discrete Wavelet Transform
AMBE	Absolute Mean Brightness Error
ANOVA	ANalysis Of VAriances
AWGN	Additive White Gaussian Noise
BBHE	Brightness preserving Bi-Histogram Equalization
BHEPL	Bi-Histogram Equalization with Plateau Limited value
cdf	Cumulative Distribution function
CIR	Contrast Improvement Ratio
CLAHE	Contrast Limited Adaptive Histogram Equalization
CLSM	Confocal Laser Scanning Microscopy
CWT	Continuous Wavelet Transform
DAQ	Data Acquisition
DOE	Design of Experiment
DWT	Discrete Wavelet Transform
EME	Measure of Enhancement
FIR	Finite Impulse Response
FOV	Field of View
GCV	Generalized Cross Validation
GGD	Generalized Gaussian Distribution
HE	Histogram Equalization
HMD	Homogeneity Mean Difference
HO	Homogeneity
HPF	High Pass Filter
IDWT	Inverse Discrete Wavelet Transform
LPF	Low Pass Filter
MBE	Mean Brightness Error
MMBEBHE	Minimum Mean Brightness Error Bi-Histogram Equalization
MSE	Mean Squared Error

NA	Numerical Aperture
PCA	Principal Component Analysis
pdf	Probability Distribution Function
PMT	Photo Multiplier Tube
PSNR	Peak Signal-to-Noise Ratio
ROI	Region of Interest
SNR	Signal to Noise Ratio
SSIM	Structure Similarity Index Measure
SURE	Stein's Unbiased Risk Estimator
SVD	Singular Value Decomposition
WT	Wavelet Transform

1. INTRODUCTION

Optical imaging devices are being increasingly used to survey and diagnose tissue pathology *in-vivo*. Confocal Laser Scanning Microscopy (CLSM) is a powerful, integrated electronic microscope technique which has been frequently used to obtain high-resolution images of living cells and serial optical sections in biomedical research including clinical biology [1–3]. This optical sectioning property of CLSM enables cellular structures, histological images of cell morphology and tissue architecture to be viewed without taking biopsies from the living bodies. The main principle of confocal microscopy was developed by Marvin Minsky in 1957 (i.e.; pinhole aperture point-by-point illumination of the specimen) for obtaining high-resolution images [4]. In this manner, sequentially acquired 2D images from different depth allow us to obtain 3D volumetric images by image reconstruction. Compared to the conventional microscopy methods, CLSM has the principal advantage of capability of to acquire each slice of the depth,i.e. the cell-layers. It is also a useful tool for biologist to track and localize intracellular particles in dissociated cells.

When an intense beam of light emitted by an excitation source is focused and rastered across the surface of the specimen with the use of x-y scanning mechanism, the intensity can be recorded into an array to create an image. Rastered point source across a field of view back-scatters and is fed into a detector that measures the spatial intensity. Hence these intensities in an array of pixels create image of this optical section. Collected light intensity is related to the index variability of surrounding tissue. These grayscale intensity values are recorded and quantized at an 8-bit resolution ranging from 0 to 255. CLSM images have the information of refractive index variation within the tissue of specimen. These refractive index variations are caused by the chemical variations within the tissue. Structures that back-scatter more light appear brighter than less scattering structures. When focusing deep inside the specimen, much of the light is evanesced due to scattering and various image distortions may occur due to differences of the optical index inside the specimen. A consequential processing of the CLSM images is required to cope with these problems.

There are also some issues concerned with CLSM performance and acquired image quality depends on these limitations [5]. When light source is pointed onto specimen an airy disk formed in the focal plane and the disk size depends on the wavelength and the numerical aperture of the objective lens. Airy disk effects resolution quality of the image. Besides the pinhole size involves in blocking unwanted out-of-focus light but by doing that it also reduces the signal intensity which increases noise in the image. Another factor affecting the image quality is the photodetector, i.e. Photo multiplier tube (PMT) which collects the light filtered out by the pinhole. Variations in the number of detected photons results with a shot noise which has a Poisson distribution for small numbers of photon. But for large numbers of photon, the Poisson distribution approaches a symmetrical normal distribution making the shot noise in actual observations indistinguishable from a Gaussian noise [6]. Therefore the noise model in CLSM is determined not choosing the Poissonian model over the traditional Gaussian model and the method in this study aims to restore acquired data contaminated Gaussian noise.

As a noise filtering approach, wavelet transformation is used for the purpose of image denoising. Wavelet transformation represents a further extension Fourier transformation and is commonly applied for both image compression and denoising [7–12] since it gives a better representation of 2D images in time and frequency domains. A wavelet is a fast-decaying wave-like oscillation that starts with an amplitude of a given (non-zero) amount and decreases rapidly to zero. This means that a wavelet is zero-valued outside of a defined interval. It can typically be visualized as a brief oscillation. The main procedure of wavelet denoising follows that it firstly decomposes the image into wavelet space by using a certain wavelet family and obtains coefficients of the image up to a predefined decomposition level. Afterwards coefficients are subjected of a threshold depending on the noise level using several methods. Method plays a main role due to the nature of the signal. Hence handling with CLSM images requires excessive attention. Subsequently the inverse transformation takes place using thresholded coefficients and reconstructs noisy-free estimated image. Since the visual perception of the result of denoising method can be deceptive, various evaluation criteria (i.e. metrics) are needed. Objective image quality metrics can be group into two main categories: no-reference and full-reference. Parameter tuning of the denoising algorithm is an important issue and in practice the choice usually is made empirically with trial and er-

ror when there is no ground truth reference. Therefore to evaluate denoised CLSM images properly, a no reference metric is also needed hence Q-Metric [13, 14] and an algorithm for the estimation of noise level from single image [15] have been utilized for this purpose. Q-Metric is based on singular value decomposition of local image gradients and provides a measure of ground truth image. Estimation of standard deviation of the additive white Gaussian noise in a single image is done using local variance calculation which provides a robust statistical measure of the noise.

Alongside the image denoising, a fundamental contrast enhancement is needed in CLSM for better image contrast, especially for dense tissues in tumor detection [16]. Contrast enhancement is a operation which enhances human perception of details and improves rapid recognition of interested targets. The brightness of pixel in CLSM image correlates with relative intensity of the reflected light. Therefore the contrast is a result of variations in the refractive index due to structures within the biological specimen. To overcome poor and low-contrast images several histogram equalization techniques have been employed for remapping the gray levels based on the probability distribution of the image. These techniques make use of simple linear/non-linear intensity level transformation functions and it can result with over-enhanced or mean brightness shifted image. The intensification of the existing noise is of concern too. Different algorithms are developed to deal with these problems [17–21]. Using these methods experimental studies are carried on along with different evaluation metrics.

The novelty of this study is that different kind of denoising and enhancement methods are applied to enhance images acquired using optical microscope and real biological images of biological samples are evaluated under different performance metrics. The images are acquired from the optical setup and from a image database for comparison. For noise filtering 2D discrete wavelet transform (DWT) is developed. Similar to other denoising techniques, the matter is that affects the performance of 2D-DWT is the selection of components employed in the algorithm along with their parameters values. With the help of ANOVA statistics, this study also investigates the effect of employing different combinations of tuning parameter selections for 2D-DWT denoising in the manner of different metric improvements.

2. BACKGROUND

2.1 Laser Scanning Confocal Microscopy

Confocal Laser Scanning Microscopy (CLSM) is a radiation-free optical scanning and imaging method which enables us to obtain high resolution and high contrast images. Confocal sections of few hundred micrometers under the tissue can be acquired to make 3D imaging and diagnosis of the abnormal developments in both cell morphology and the structure of tissue with the help of in-vivo optical imaging. The reason for using laser is that it provides very high intensity and the certain band of wavelength of light source. The main principle of CLSM was pioneered and later patented by Marvin Minsky in 1957 by focusing laser light onto a single point at a time. Unwanted scattered light is avoided when the light returns from the illuminated specimen and passes through a pinhole aperture. Desirable light arrays are gathered by a PMT to construct image formation. Minsky performed scanning the specimen by moving its stage rather than directing rays onto a vertically and horizontally scanning mirrors. The word "confocal" is derived from a contraction of "conjugate" and "focal" which means that a single point can both be illuminated by a point source and imaged by a detector at the same time in the same plane. Serial optical sections can be collected in CLSM by scanning the specimen using a focused intense beam of light and then collecting the back-reflected signal to the detector from each spot via a pinhole aperture which blocks scattered light from out-of-focus areas as seen in Figure 2.1. Focused beam from laser source is reflected by a dichroic mirror into objective lens. The point illumination of laser beam is carried through by an objective lens at the desired focal plane in the specimen. Some of the emitted light signals in all directions from the specimen are captured by the objective lens and pass through the dichroic mirror. The confocal pinhole prevents out-of-focus light originating from above and below the focal plane in the specimen from reaching the photodetector, i.e. Photo Multiplier Tube. Finally PMT generates a signal related to the brightness of the light from the specimen. Despite the point illumination and the presence of the pinhole have an impact on improved lateral and axial resolution there are some limitations of CLSM. Pinhole size plays a main role on the strength of optical sectioning. The diameter of the pin-

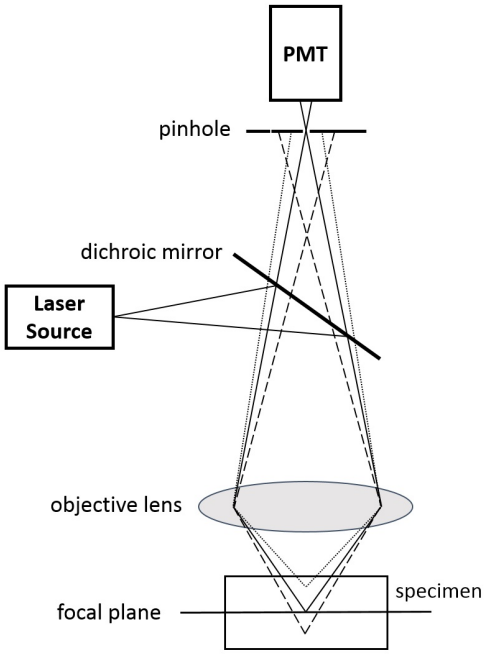

Figure 2.1 Basic Light Pathways of CLSM, showing how out-of-focus lights are eliminated by pinhole aperture.

hole determines how much of the back-scattered light emitted by the specimen is collected, and the thickness of the optical section. A 3D diffraction pattern occurs in the focal plane and its cross section is an Airy disk which is a circular diffraction pattern. For the sake of gaining resolution, choosing a pinhole size less than the diameter of that Airy disk reduces the total signal content, i.e. reducing Signal to Noise ratio (SNR). A trustworthy eradication of the noise of LSCM images can improve the SNR and prevent blurring. As a result CLSM images demands a denoising task for image recovery. Different researches have been conducted for that purpose. A study is presented to denoise 3D confocal microscope scans of neuronal cells with quality measure developed specifically for confocal images of nerve cell [22]. Another used a wavelet denoising technique in combination with classical deconvolution algorithms and applied it to 3D confocal images [23]. The other one used complex wavelet transform to eliminate noise whose distribution is approximated to a Gaussian distribution and they performed simulations on real biological data [24]. So, wavelet thresholding provides a reasonable results to estimate signal. In my thesis 2D discrete wavelet transform (DWT) will be used as a tool for the analysis of CLSM images.An insight is presented to show which thresholding technique and optimum threshold selection to which noise on the real CLSM images are more sensitive to.

2.2 Continuous Wavelet Transform

The Wavelet transform is a compelling tool that splits non-stationary signal or data into different frequency components. Simple building blocks named as wavelets mean a small wave and are used to perform the transform by the translation and the dilation of the signal along time axis [25]. The term mother wavelet implies that the functions with different region of support that are used in the transformation process are derived from one main function, or the mother wavelet. Hence the mother wavelet is a prototype for generating the other window functions [26]. By the reason of infinite support of sine and cosine functions it is insufficient for Fourier analysis to localize edges. Therefore WT can be thought of as an extension of Fourier Transform instead of a single scale of time or frequency. The definition of the continuous wavelet transform (CWT) of a signal $x(t)$ is as in

$$\begin{aligned} CWT(\alpha,\tau) &= \langle x(t), \psi_{\alpha,\tau}(t)\rangle \\ &= \int_{-\infty}^{+\infty} x(t)\psi_{\alpha,\tau}(t)\mathrm{d}t \end{aligned} \tag{2.1}$$

$$\psi_{\alpha,\tau}(t) = \frac{1}{\sqrt{\alpha}}\psi^*\left(\frac{t-\tau}{\alpha}\right) \tag{2.2}$$

where $*$ denotes complex conjugation and α is the scale parameter that stretches or compresses the function, τ is the translation factor for time shifting mother wavelet along the axis and also $\alpha > 0, \tau \in \Re$. The mother wavelet is denoted as $\psi_{\alpha,\tau}(t)$ and it is window function of the scale and translation parameter. The term $\psi\left(\frac{t-\tau}{\alpha}\right)$ is a shifted and scaled base term of the mother wavelet to be used in decomposition and reconstruction of the signal. The signal $x(t)$ can be reconstructed by using the synthesis formula given by

$$x(t) = \frac{1}{C_\psi}\int_\alpha\int_\tau CWT(\alpha,\tau)\psi\left(\frac{t-\tau}{\alpha}\right)\frac{d\alpha d\tau}{\alpha^2} \tag{2.3}$$

where C_ψ is the admissibility constant and inverse transform exist only if it should satisfy the admissibility condition

$$C_\psi = 2\pi \int_{-\infty}^{\infty} \frac{|\hat{\psi}(\omega)|^2}{|\omega|} d\omega < \infty \tag{2.4}$$

where $\hat{\psi}(t)$ is the Fourier Transform of the oscillatory wavelet function $\psi(t)$ and it should be satisfied that $\int \psi(t)dt = 0$. Therefore a good mother wavelet is a key element due to its ability to reconstruct the signal from the wavelet decomposition.

2.3 Discrete Wavelet Transform

Calculation of wavelet coefficients for each scale needs a substantial computational time and result in a vast amount of data. For this reason Discrete Wavelet Transform (DWT) is often used. The discrete $x[n]$ function can be expressed as so in Fourier Series expansion by basic orthonormal Ψ_k terms. These are sines and cosines in Fourier Expansion whereas in DWT they are simply the translated and scaled versions mother wavelets Ψ. The variety of mother wavelet examples can be found in the work of [25]. The linear expression of discrete function $x[n]$ based on DWT can be expressed as;

$$x[n] = \sum_{a,b} d_{a,b} \Psi_{a,b}[n] \tag{2.5}$$

where $d_{a,b}$ is analysis coefficient, $\Psi_{a,b}$ represents the analysis function (basic). DWT is the sampled version of the CWT on a dyadic grid, i.e., selecting the parameters as $\alpha = 2^a, \tau = 2^a b$ in Eq. 2.2. For a sampling period T, $t = nT$, the DWT of the discrete signal of x[n] is given as

$$\begin{aligned} DWT(a,b) &= \langle x[n], \psi_{a,b}[n] \rangle \\ &= \sum_n x[n] \psi_{a,b}[n] \end{aligned} \tag{2.6}$$

$$\psi_{a,b}[n] = 2^{-\frac{a}{2}} \psi^* \left(2^{-a} n - b\right) \tag{2.7}$$

where $n, a, b \in \mathbb{Z}$. The orthogonality of mother wavelets Ψ_k in $\mathscr{L}^2(\Re)$ can be shown as

$$\langle \Psi_k[n], \Psi_l[n] \rangle = \sum_n \Psi_k[n], \Psi_l[n] = 0 \text{ for } k \neq l \tag{2.8}$$

The inverse DWT can be used to resynthesize x[n]

$$x[n] = \sum_a \sum_b DWT(a,b) 2^{-\frac{a}{2}} \psi \left(2^{-a} n - b\right) \tag{2.9}$$

Signals are decomposed to lower and higher frequency components at each level by doing a dyadic transform. As seen in the Figure 2.2 signal decomposition is equivalent to high and low frequency filtering. Downsampling by 2 is performed after each level of decomposition to preserve the number of data points in the original signal. The high-frequency (detail) coefficients have smaller signal energy and correspond to the noise components. The low-frequency (approximation) coefficients have larger signal energy and then reused for next stages. The Eq. 2.6 can be seen as a FIR filter whose general expression is

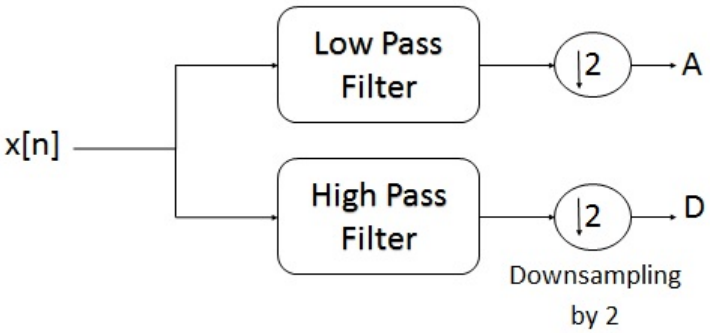

Figure 2.2 Wavelet Decomposition A: Approximation D: Detail

$$y[n] = \sum_k x[k] h[2n - k] \tag{2.10}$$

Half-band filtering reduces resolution by a factor of two and doubled in scale due to down-sampling by a factor of two [7]. Therefore mathematical expression of filtered (by low-pass

h[n] and high-pass g[n]) and downsampled (by 2) x[n] can be expressed as;

$$y_{low}[n] = \sum_k x[k]h[2n-k] \tag{2.11}$$

$$y_{high}[n] = \sum_k x[k]g[2n-k] \tag{2.12}$$

The maximum decomposition level depends on the length of the discrete signal. Coefficients obtained by DWT correspond to energy distribution in time and frequency [27].

2.4 Two-Dimensional Discrete Wavelet Transform

Two-dimensional wavelets are a natural extension of the one dimensional case in rows and columns. They can be used as a tool for many two-dimensional situations such as image denoising. DWT of image signals produces a non-redundant image representation providing better spatial and spectral localization of image formation. Multiresolution analysis and wavelets can be generalized to higher dimensions [28]. Therefore 2D scaling function (wavelet) can be thought as a product of two 1D functions such as [29],

$$\phi(x,y) = \phi(x)\phi(y) \tag{2.13}$$

and the dilation equation assumes the form as,

$$\phi(x,y) = 2\sum_{k,l} h(k,l)\phi(2x-k,2y-l) \tag{2.14}$$

Since both $\phi(x), \phi(y)$ satisfy the dilation equation by $h(k,l) = h(k).h(l)$ then we can analogously construct the wavelets instead of using one single wavelet function but three wavelet

functions [30]:

$$\begin{aligned}\psi^{I}(x,y) &= \phi(x)\psi(y)\\ \psi^{II}(x,y) &= \psi(x)\phi(y)\\ \psi^{III}(x,y) &= \psi(x)\psi(y)\end{aligned} \tag{2.15}$$

The corresponding dilation equations are:

$$\begin{aligned}\psi^{I}(x,y) &= 2\sum_{k,l} g^{I}_{k,l}\phi(2x-k,2y-l)\\ \psi^{II}(x,y) &= 2\sum_{k,l} g^{II}_{k,l}\phi(2x-k,2y-l)\\ \psi^{III}(x,y) &= 2\sum_{k,l} g^{III}_{k,l}\phi(2x-k,2y-l)\end{aligned} \tag{2.16}$$

where $g^{I}(k,l) = h(k)g(l), g^{II}(k,l) = g(k)h(l), g^{III}(k,l) = g(k)g(l)$. Hence new wavelet equation in 2D takes the form as:

$$\psi^{(S)}_{a,b,c}[n,m] = 2^{-\frac{a}{2}}\psi^{(S)}(2^{-a}n-b, 2^{-a}m-c) \tag{2.17}$$

where $S = h,v,d$ corresponds h-horizontal, v-vertical, d-diagonal details respectively. The discrete approximation and detail coefficients can be computed in a similar manner as:

$$\begin{aligned}\underbrace{d_{a,b,c}}_{\text{approximation}} &= \sum_{n,m} 2^{-\frac{a}{2}}\phi(2^{-a}n-b, 2^{-a}m-c)x[n,m]\\ \underbrace{d^{(S)}_{a,b,c}}_{\text{detail}} &= \sum_{n,m} 2^{-\frac{a}{2}}\psi^{(S)}(2^{-a}n-b, 2^{-a}m-c)x[n,m]\end{aligned} \tag{2.18}$$

An image can be decomposed into a sequence of different spatial resolution images using DWT as seen Figure 2.3. For N-level decomposition of 2D image it yields $(3N+1)$ different frequency sub-bands namely LL (approximation), LH (vertical-detail), HL (horizontal-detail) and HH (diagonal-detail) subbands as in the Figure 2.4. After rows are passed through low and high pass filter, downsampling by 2 is performed resulting with LL, LH, HL and HH coefficients in 2D image. For the decomposition of the next stage approximation (LL) image

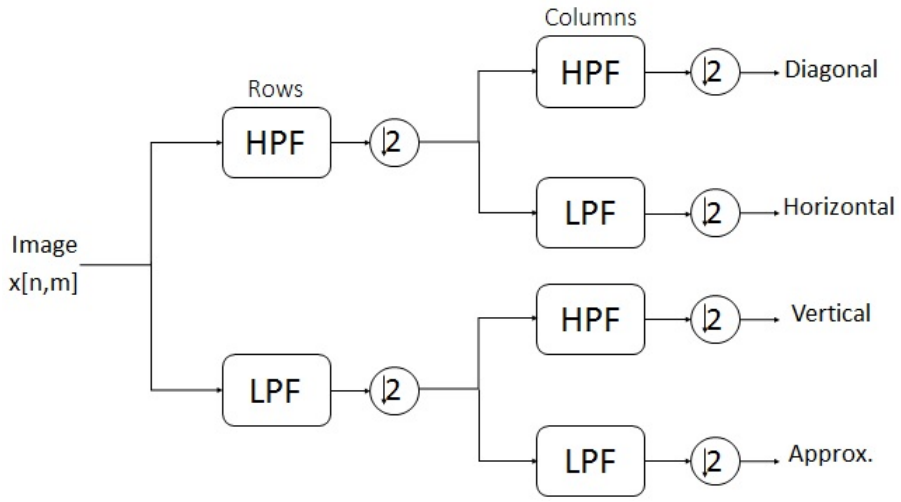

Figure 2.3 2D-Wavelet Decomposition

is to be used. The Additive Gaussian noise will nearly be averaged out in low frequency wavelet coefficients. Therefore the coefficients in the higher frequencies need to be thresholded.

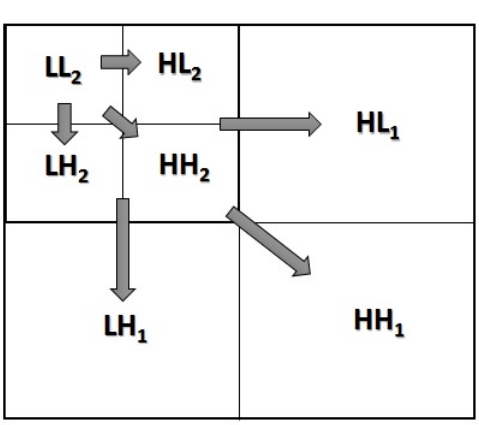

(a) 2D-DWT with Two-level Decomposition

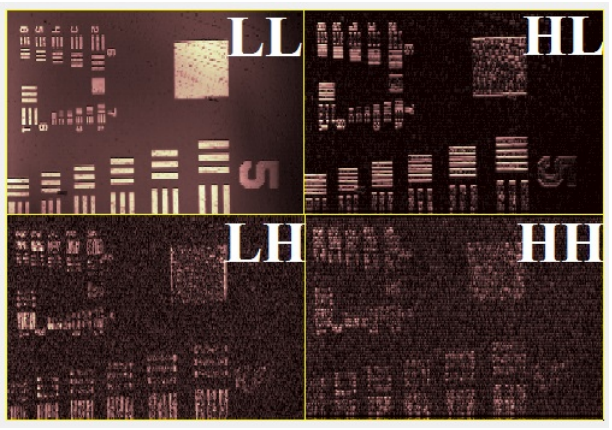

(b) Single-Level Image Decomposition

Figure 2.4 Subbands of the 2-D Wavelet Transform

3. METHOD

3.1 Optical Setup

Confocal laser scanning microscope mechanism is established for the first time within our research group. Figure 3.3 illustrates the configuration of the established CLSM setup where actual setup is shown in Figure 3.4 with basic components. The system is based on a custom-built confocal laser scanning microscope. The excitation source used for laser microscope is Thorlabs-LP660-SF60 60mW 658nm pigtail laser diode with 2 mm spot size seen in Figure 3.1 which mounted by Thorlabs-LM9LP in is driven by Thorlabs-ITC4001 which has a maximum operating currents from 0 to 1 A. The controller ITC4001 Figure 3.2 are compatible with all laser diodes therefore enables us to utilize different wavelength laser diodes and to built up a setup of two photon confocal microscopy in future.

(a) Input Pins

(b) Single Mode Pigtail

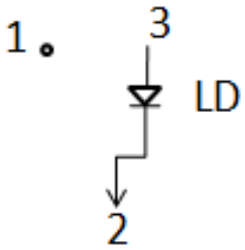

(c) Pin Diagram

(d) Diode Mount

(e) Mounted Pigtail in Laser Diode Mount LM9LP

(f) Close up of Mounted Pigtail

Figure 3.1 Pigtailed Laser Diode - Thorlabs LP660-SF60

Figure 3.2 Laser Diode Current and Temperature Controller - Thorlabs ITC4001

Light is focused to the sample by 20x 0.4 NA oil immersive objective (Olympus). The objective is placed after relay lens system in which 50mm and 150mm lenses are used. This configuration enables us to have 150 μm field of view (FOV). Reflected light is filtered by dichroic mirror and in order to focus a 25mm lens is placed before the pinhole with 75 μm aperture. At final stage photo multiplier tube is placed after pinhole to detect the signal intensity. 800x1000x^2 FOV and 2μm resolution is achieved by this configuration. XY raster scanning is performed with mirrors mounted on fast galvanometers. The target tissue is scanned in real-time using a 658nm laser excitation source. Collected data was processed in MATLAB software and an image is formed accordingly.

3.1.1 2D Galvo Scanner

One of the most important components of the CLSM is galvanometric mirror which provides the fast scanning axis. There are two scanning mirrors mounted on the galvo system, each of them are responsible for scanning a given direction of the imaging plane, x-axis and y-axis, shown in the Figure 3.5. Thorlabs GVSM002/M 2D Galvo System is attached to the setup as scanner and has the maximum scanning angle of $\pm 12.5^{\circ}$. XY-raster scanning is used to scan the target with 1Hz vertical scanning frequency where lateral scanning frequency is 100Hz. Galvo scanner is driven by the program which is constructed by using MATLAB.

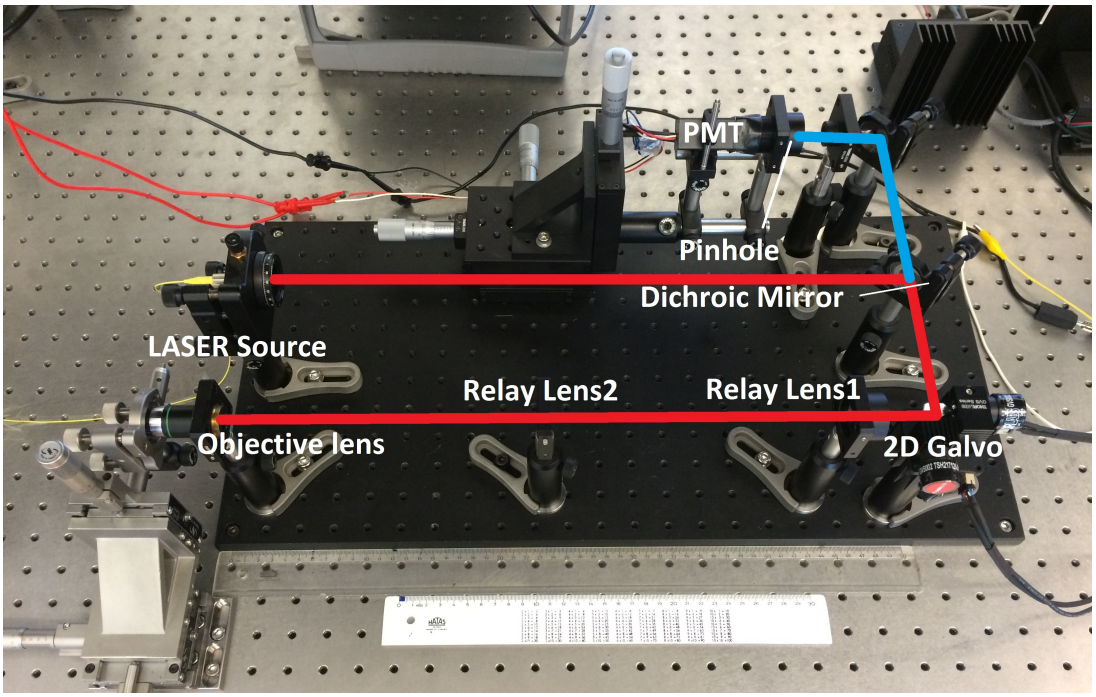

Figure 3.3 CLSM optical setup.

3.1.2 Data acquisition and processing

Data is acquired from PMT via National Instruments NI PCI-6239 data acquisition (DAQ) card with 10^6Hz sampling rate. Since the sampling rate is so high, no pre-processing is applied. DAQ card is also used to control 2D Galvo mirror movement and laser scanning data storage of image data of each scan. Figure 3.6 shows a representative test image taken of a negative 1951-USAF resolution test target using the CLSM system in Figure 3.3. The collected image data is often noisy either as a result of the data acquisition process or due to the disturbance of biological systems. This noise amount must be eliminated from the data before the acquired image is analyzed. Denoising process can be considered as constructing an optimal estimate of the unknown noise-free signal from the observed noisy data. In this study wavelet-based denoising techniques are performed.

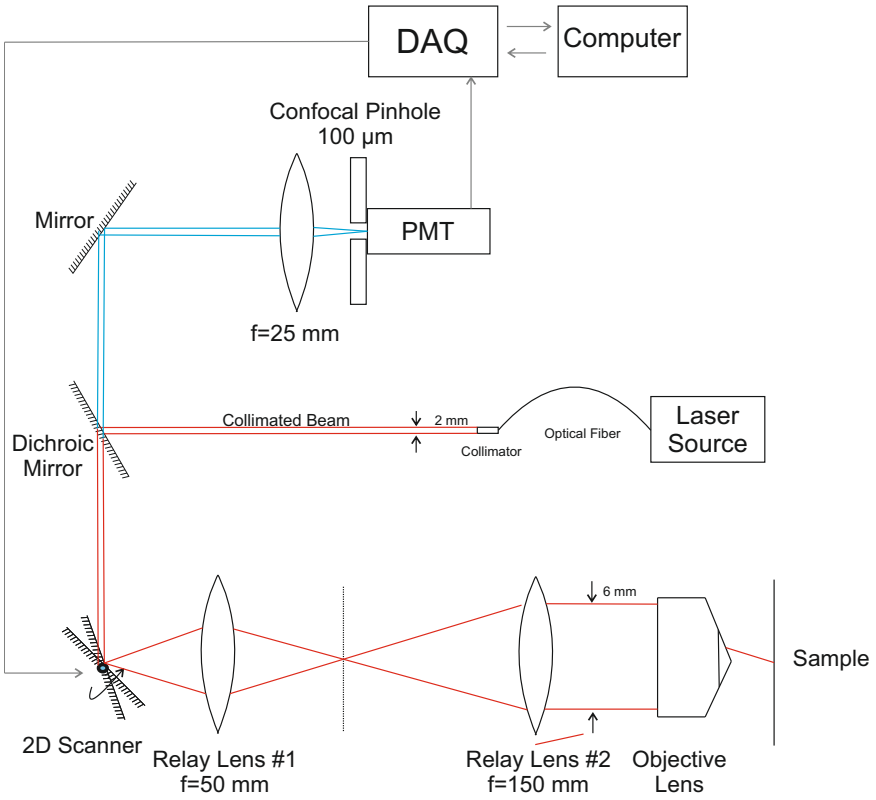

Figure 3.4 Scheme of established setup.

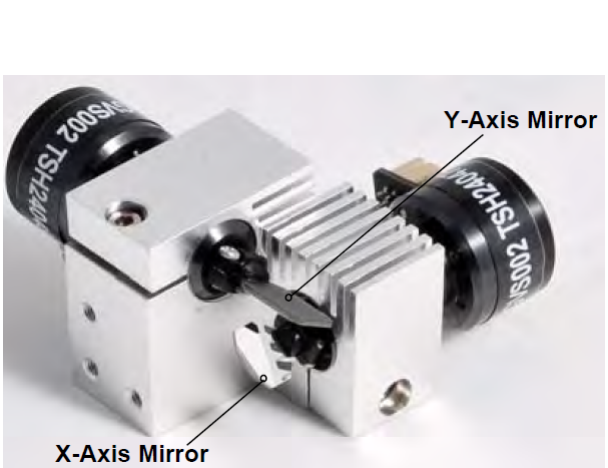

(a) Dual-Axis Galvo Assembly -Thorlabs GVSM002

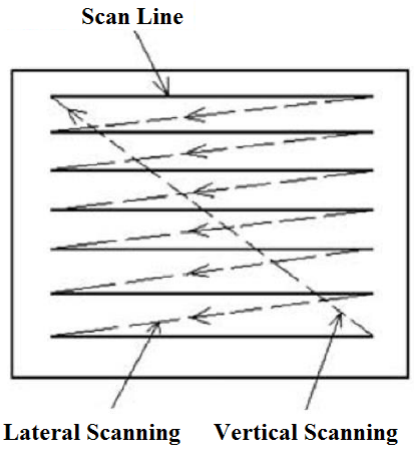

(b) XY-Raster Scanning by Galvo

Figure 3.5 2D-Scanning System

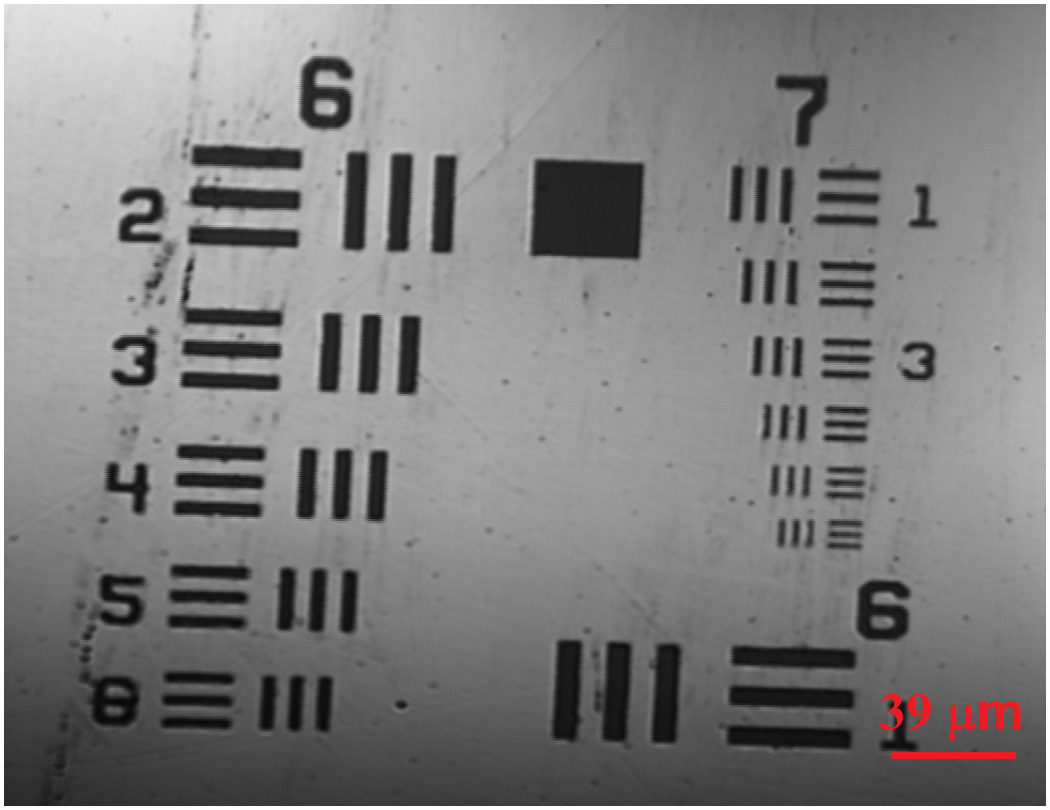

(a) Acquired image scan of the resolution target from optical setup

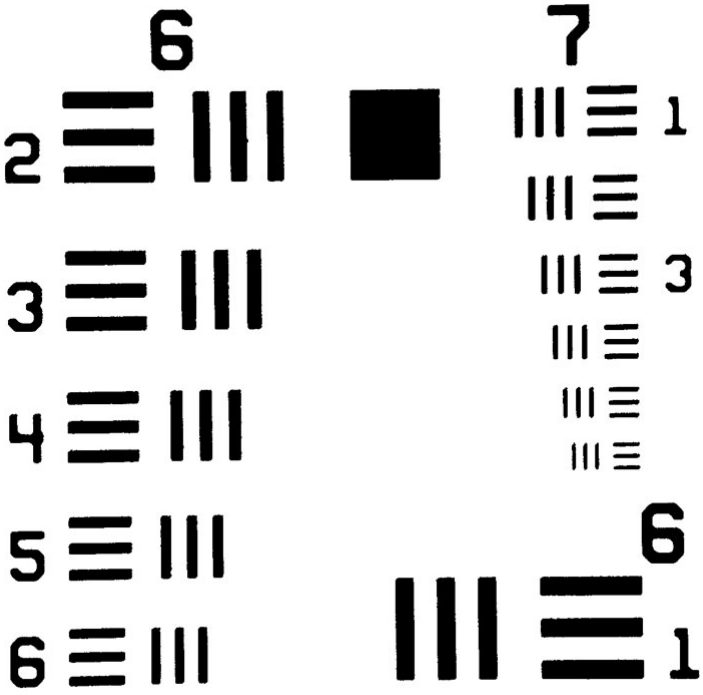

(b) 1951 USAF pattern of resolution test target

Figure 3.6 Example image generated by the 2D confocal scanning system

3.2 Estimation of Noise in a Single Image

Estimating the standard deviation of AWGN in confocal images is necessary to see the performance of denoising applications. Assuming that the noise distribution is additive zero mean Gaussian noise, i.e, AWGN. The aim of noise level estimation is to estimate the unknown standard deviation σ, of a given single observed noisy image. There are many algorithms proposed for this goal. Immerkær presented a fast method which only requires 3×3 convolutions and averaging [31]. It is computationally less expensive and works well with high level noise. A 7×7 patch-based algorithm is presented by Liu et al. and they used principal component analysis (PCA) to estimate noise level based on a texture strength [32,33]. In their algorithm they calculate a metric depending on the eigenvalues of the image gradient covariance matrix. Thereafter they use it for texture strength analysis with different noise levels. Roodt et al. proposed another novel method in [15] and in this study their algorithm is utilized for the purpose of estimating the noise level in single confocal images. The algorithm of the noise estimation for a single image is provided in Fig.Figure 3.7.

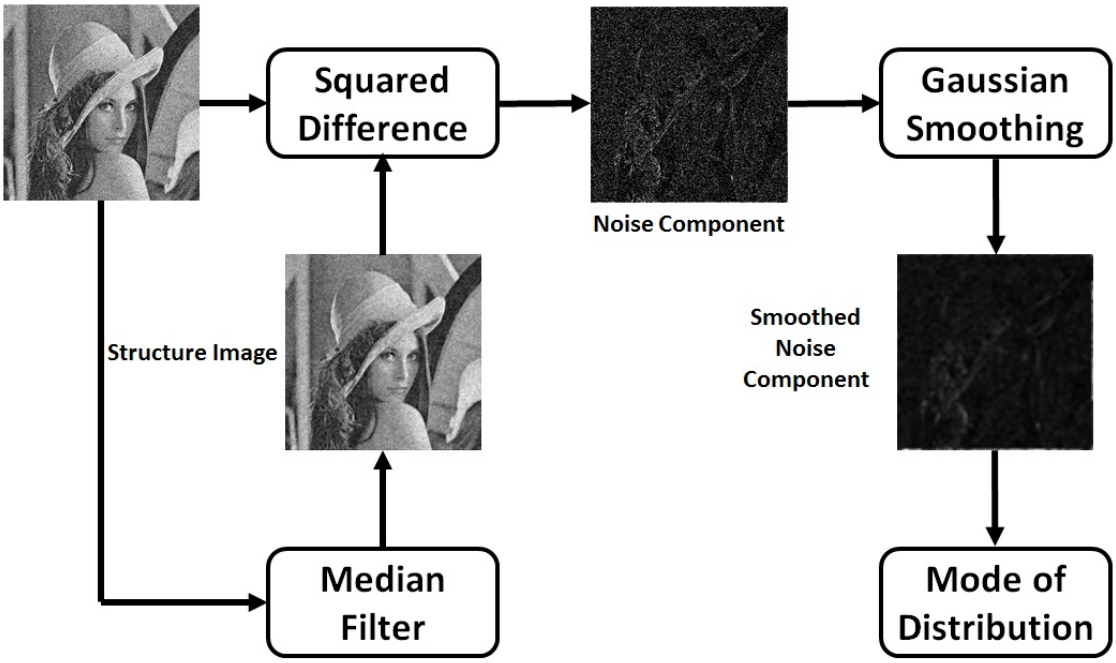

Figure 3.7 Algorithm of noise estimation in a single image [15]

In brief, the procedure can be summarized as:

1. Perform one dimensional 3×1 and 1×3 median filtering of the input image respectively. The resulting image is an approximation of noise-free image and it is called as structure image.

2. Extract the noise component by taking squared difference of the input image and the structure image. Noise Component=(Structure Image-Input Image)^2

3. Perform one dimensional 13×1 and 1×13 Gaussian filtering, i.e., smoothing of the noise component respectively. The standard deviation of Gaussian smoothing kernel is empirically selected as $\sigma = 5$.

4. Generate a histogram by partitioning the smoothed noise component values into bins, and return counts in each bin, as well as the bin edges. Specify number of bins using the Eq. 3.1

$$N_{bins} = \left\lfloor \frac{N}{bin\ size} \right\rfloor \tag{3.1}$$

   where $\lfloor . \rfloor$ is floor function and N is the total number of pixels in the input image. *bin size* is the minimum number of values that would have been placed in each bin if the values were uniformly distributed. A *bin size* of 10 was empirically selected to obtain better results.

5. The statistical Mode operation is performed after binning histogram. The mode is the value that appears most often in a set of data, thereby, the bin containing the most of the values is selected. The middle of the bin edges of the largest bin corresponds the variance estimate. Take the square root of it yielding standard deviation σ, of the noise in the image.

The accuracy of three proposed noise estimators was examined by adding AWGN with several noise levels to Lena image seen in Figure 3.8(a) and to a image of living heart tissue using fiber-optics and laser-scanning confocal microscopy in Figure 3.8(c) [34]. Lena and

a confocal image are of the size of 512×512 and 570×630 respectively. Each pixel has an integer value 0,...,255. Both images are tested with AWGN with zero mean the noise levels ranging from $\sigma = 1$ to $\sigma = 20$. Estimators then had to estimate the amount of noise contained in noisy images and this process was repeated 20 times. At each iteration a new random noise with same noise level was generated, added to noise-free images and rounded to nearest integer, i.e, clipping. The percentage error rate of the estimated noise levels are calculated by

$$Error(\%) = \frac{|Estimated\ Value - Exact\ Value|}{|Exact\ Value|} \times 100 \tag{3.2}$$

(a) Noise Free 512×512 Lena Image

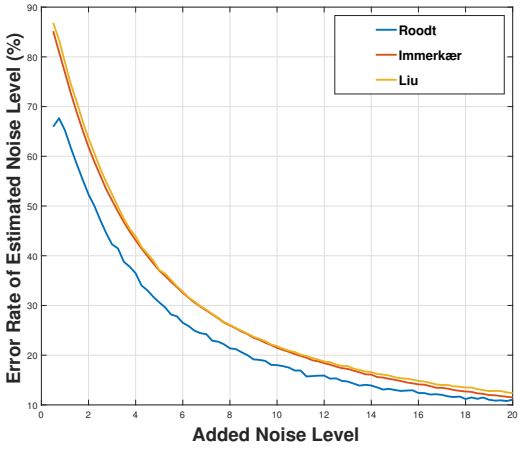

(b) Lena Image

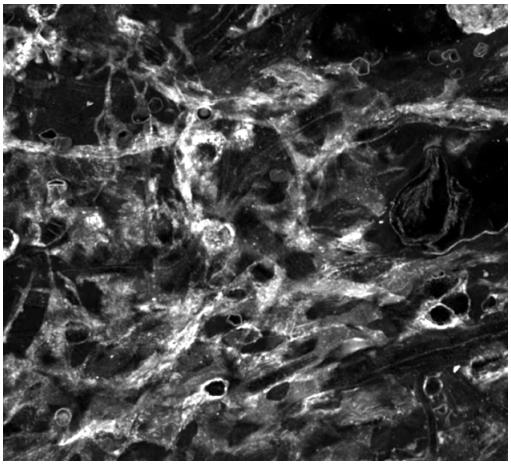

(c) Noise Free 570×630 Confocal Microscopy Image [34]

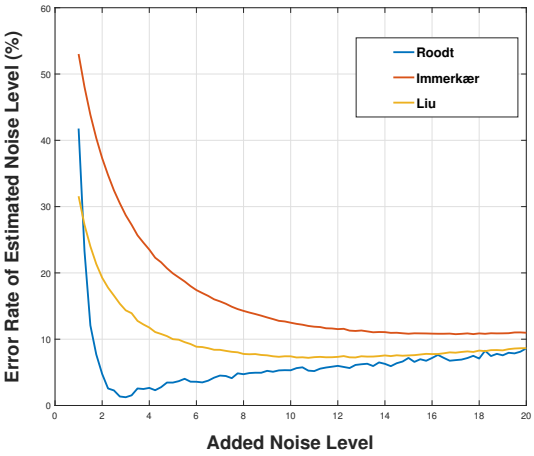

(d) Confocal Image

Figure 3.8 The average estimation error rates for various degrees of AWGN

The average percentage errors are plotted in Figure 3.8. The existing small amount of noise in original images is negligible and hence initial values are substracted from estimation values. The method from [15] gives the highest accuracy for both test and henceforth it will be used as a reliable noise level estimator.

3.3 Image Denoising with Wavelet Thresholding

Assuming that an clean image $x_{i,j}$ where $1 \leq i, j \leq n, m$ consists of $N = n \times m$ pixels and they are exposed to AWGN [12, 35, 36].

$$y_{i,j} = x_{i,j} + \varepsilon_{i,j} \tag{3.3}$$

where ε is the noise term $\sim N(0, \sigma^2)$ which has iid and zero mean. The main purpose of filtration is to estimate $\hat{x}_{i,j}$ of clean x image from noisy y image so that minimum Mean Squared Error (MSE) is obtained.

$$MSE = \frac{1}{N}\|\hat{\mathbf{x}} - \mathbf{x}\|^2 = \frac{1}{N}\sum_{i,j}^{N=n\times m}\left(\hat{x}_{i,j} - x_{i,j}\right)^2 \tag{3.4}$$

The 2D-DWT and its inverse transform can be symbolized as $\mathscr{W}$ (decomposition) and $\mathscr{W}^{-1}$ (reconstruction). One can create the matrix form of the original,noisy and noise image including subband coefficients in transformation domain as

$$\mathbf{Y} = \mathscr{W}\mathbf{y}, \qquad \mathbf{X} = \mathscr{W}\mathbf{x}, \qquad \mathbf{N} = \mathscr{W}\varepsilon \tag{3.5}$$

Therefore the noisy image in spatial domain takes the form in transformation domain as:

$$\mathbf{Y} = \mathbf{X} + \mathbf{N} \tag{3.6}$$

where $\mathbf{Y}, \mathbf{X}$ and $\mathbf{N}$ represents noisy, clean, noise image respectively. The orthogonality of the transformation assures that the noise in the transformation domain also shows Gaussian

distribution. Then denoised estimation is as:

$$\hat{\mathbf{x}} = \mathscr{W}^{-1}\hat{\mathbf{Y}} \tag{3.7}$$

In Eq. 3.7 $\hat{\mathbf{Y}}$ means denoised noise image of $\mathbf{Y}$ whose coefficients are thresholded.

The main denoising procedure contains these steps:

1. Choose a wavelet base and the number of decomposition level, J.
2. Obtain Horizontal, Vertical and Diagonal coefficients of the noisy image by applying J-level decomposition.
3. Perform thresholding of coefficients
   (a) Determine Threshold Calculation Method (δ)
   (b) Select Thresholding function $\eta(\omega, \delta)$
   (c) Apply the threshold on either globally, level-wise or detail-wise sub-bands.
4. Reconstruct the image by 2D-IDWT using estimated coefficients

Figure 3.9 Denoising Using 2D-DWT

The wavelet coefficients calculated by the wavelet transform represent change in the time series at a particular resolution. To filter out noise thresholding has an important role in the denoising process. Thresholding is performed to remove the low energy coefficients as their contribution to the wavelet spectra is very low. A small threshold retains the noisy coefficients whereas a large threshold leads to the loss of original image signal details. There are two types of thresholding used in this work; Hard Thresholding and Soft Thresholding.

Hard thresholding is a "keep or kill" procedure that sets any coefficient less than or equal to the threshold to zero as in the following:

$$\eta_H(\omega,\delta) = \omega_\delta = \begin{cases} \omega & |\,\omega\,| \geq \delta \\ 0 & |\,\omega\,| < \delta \end{cases}$$

The modified wavelet coefficients, ω_δ are obtained after applying a threshold, δ. In the soft thresholding, the threshold is substracted from coefficients that are greater than the threshold:

$$\eta_S(\omega,\delta) = \omega_\delta = \begin{cases} \omega - \delta & \omega \geq \delta \\ 0 & |\,\omega\,| < \delta \\ \omega + \delta & \omega \leq -\delta \end{cases}$$

To each individual wavelet coefficients we apply this threshold rule, either soft (a continuous function of the data which shrinks each observation) or hard (which retains unchanged only large observations above the threshold). It is known that soft thresholding yields smoother and visually pleasant results in comparison with the hard thresholding due to continuity. On the other hand hard thresholding provides better edge preservation with respect to the soft one.

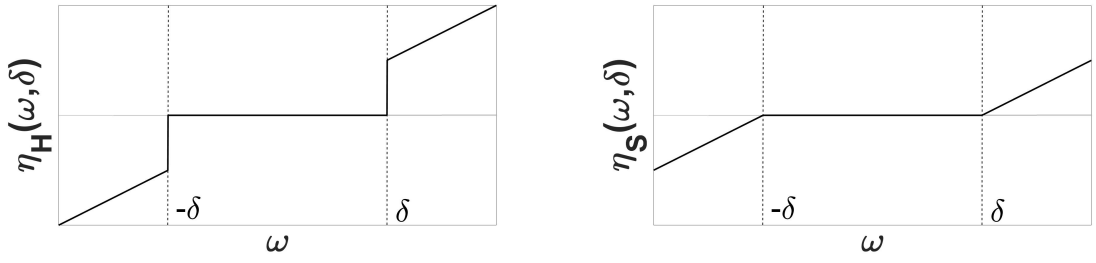

Figure 3.10 Hard and Soft Thresholding

3.3.1 Threshold Calculation Methods

The choice of threshold is very crucial to the success of the denoising and is currently subject to an intense effort there are various ways to determine the threshold value δ. Small

threshold may result with noise being in effect on the other hand large threshold produces a smooth signal by killing (or zeroing) details which causes blur and artifact. In this work we have used several methods to choose threshold. It is critical to find an optimal threshold such that the MSE is minimized.

(Universal) In *VisuShrink* procedure Donoho and Johnstone proposed a universal threshold that is near-optimal in the minimax sense (minimizing the maximum error) and defined its expression as a function of the estimated noise standard deviation $\hat{\sigma}$ from the coefficients [37]. The universal threshold is

$$\delta_{Universal} = \hat{\sigma}\sqrt{2\log N} \tag{3.8}$$

where N is the number of samples. In practice since $\hat{\sigma}$ is unknown, a robust median estimator is used to estimate the noise standard deviation in different ways depend on the employed coefficients due to dependence on the number of samples, N.

$$\hat{\sigma} = \frac{median\left(\mid y_{i,j} \in \mathbf{Y} \mid\right)}{0.6745} \tag{3.9}$$

Generally universal threshold performs an over-smoothing effect and usually underfits the data. Estimation is done in three different ways to determine the threshold level [35], the thresholding can be:

i. *global threshold*: The coefficients in the diagonal subband of the first level, $y_{ij} \in HH_1$ are employed and resulting single threshold in Eq. 3.8 is calculated in which N is equal to the number of wavelet coefficients that belong to sub-band HH_1. The threshold is applied globally to all empirical wavelet coefficients at different scales. (Global Median Estimator)

ii. *level-dependent threshold*: The coefficients of a corresponding level, $y_{ij} \in \{HL_j \cup LH_j \cup HH_j\}$ are used to calculate level-based thresholds to separately apply on every coefficient of the related level. In Eq. 3.8 N is equal to the number of wavelet coefficients of the corresponding level. (Level-Dependent Estimator)

iii. *detail-dependent threshold*: The coefficients are taken from the corresponding type of details $y_{ij} \in \{HL_j\}, y_{ij} \in \{LH_j\}$ or $y_{ij} \in \{HH_j\}$ in each level and then the resulting threshold is applied to corresponding detail coefficients. In Eq. 3.8 N is equal to the number of wavelet coefficients of the corresponding detail. (Detail-Dependant Estimator)

(SURE) Another threshold related to the minimization of Stein's unbiased risk estimation [38] was presented by Donoho and Johnstone in [39] and the procedure is called as *SureShrink*. The SURE threshold is data-driven and resolution level adaptive. In SURE method the threshold is calculated by estimating the loss $\|(\hat{\mu} - \mu)^2\|$ in an unbiased way where $\hat{\mu} = \hat{\mu}(\omega)$ is a fixed estimate of μ (real mean) based on the observations ω and $\hat{\mu}$ is the soft threshold estimator where $\hat{\mu}(\omega) = \eta_S(\omega, \delta)$. Hence if one applies Stein's argument in [38] to obtain an unbiased estimate of the risk:

$$SURE(\omega, \delta) = \sigma^2 - \frac{2.\sigma^2}{N}.\#\{i : |\omega_i| < \delta\} + \frac{1}{N}\sum_{i=1}^{N} min(|\omega_i|, \delta)^2 \tag{3.10}$$

where N is the number of coefficients, σ^2 is the noise variance, ω_i is the set of noisy observation wavelet coefficients in a subband, δ is the threshold and $\#\{i : |\omega_i| < \delta\}$ indicates the number of coefficients under the threshold δ. Since we desire to obtain the threshold δ_{SURE} that minimizes the risk function in Eq. 3.10, the optimization problem:

$$\delta_{SURE} = \underset{\delta}{\operatorname{argmin}} SURE(\omega, \delta) \tag{3.11}$$

is solved using a conventional minimization method such as Fibonacci Search by a fixed number of evaluations. In [39] Donoho and Johnstone showed that *SureShrink* is optimally and automatically smoothness-adaptive hence forth the reconstruction is resulted as smooth as the mother wavelet will allow. It is again important to estimate the noise level σ from the subband coefficients as using the Eq. 3.9.

(Bayes) As you recall that the method of wavelet thresholding performs denoising by filtering each detail coefficients $\mathbf{Y}$ with a thresholding function to estimate $\mathbf{X}$ as in Eq.

3.7. The rule of *BayesShrink* in [11] adopts a Bayesian statistical structure to determine the threshold for each subband under the Generalized Gaussian Distribution (GGD) which is given by

$$GG_{\sigma_X,\beta}(x) = C(\sigma_X,\beta)exp\{-[\alpha(\sigma_X,\beta)|x|]^{\beta}\} \tag{3.12}$$

where $-\infty < x < \infty$, $\sigma_X > 0$, $\beta > 0$ and

$$\alpha(\sigma_X,\beta) = \sigma_X^{-}\left[\frac{\Gamma(3/\beta)}{\Gamma(1/\beta)}\right]^{1/2}$$

and

$$C(\sigma_X,\beta) = \frac{\beta.\alpha(\sigma_X,\beta)}{2\Gamma\left(\frac{1}{\beta}\right)}$$

and $\Gamma(t) = \int_0^{\infty} e^{-u}u^{t-1}du$ is the gamma function. In Eq. 3.12 σ_X is the standard deviation and β is the shape parameter. In *BayesShrink* we desire to find a threshold δ_{Bayes} which minimizes *Bayesian Risk* by empirically estimating β and σ_X for the wavelet coefficients in each subband having such a distribution. *Bayesian Risk* is given by

$$Bayes(\delta) = E\left(\hat{Y} - X\right)^2 = E_X E_{Y|X}\left(\hat{Y} - X\right)^2 \tag{3.13}$$

where $\hat{Y} = \eta(Y,\delta)$, $Y|X \sim N(x,\sigma^2)$ and $X \sim GG_{\sigma_X,\beta}$. The optimal threshold δ^* is given by

$$\delta_{Bayes} = \delta^*(\sigma_X,\beta) = \underset{\delta}{\text{argmin}} Bayes(\delta) \tag{3.14}$$

The Eq. 3.14 is a function of the parameters σ_X and β and it has no closed form solution for $\delta^*(\sigma_X,\beta)$ therefore some numerical calculations are done in [11] by examining different cases of β. Numerical results showed that,

$$\delta_{Bayes}(\sigma_X) = \frac{\sigma^2}{\sigma_X} \tag{3.15}$$

which is nearly optimal and very close to $\delta^* \approx \delta_{Bayes}$. The parameter β is put out of action in the expression. In the case of $\sigma/\sigma_X \ll 1$ the signal dominates the noise whereas $\sigma/\sigma_X \gg 1$ the noise suppresses the signal and the normalized threshold, δ_{Bayes}/σ is largely selected to remove the noise. The GGD parameters, σ_X and β, need to be estimated to determine the data-driven and subband-adaptive threshold $\delta_{Bayes}(\sigma_X)$. And once again we need to obtain the noise estimate by using robust median estimator Eq. 3.9. Recall that in the Eq. 3.6, **X** and **N** is independent of each other, thence,

$$\sigma_Y^2 = \sigma_X^2 + \sigma^2$$

where σ_Y^2 is the variance of observed signal **Y** whose empirical expression is given by,

$$\hat{\sigma}_Y^2 = \frac{1}{N}\sum_{i=1}^{N} \omega_i^2$$

with N being the number of the wavelet coefficients ω_i of the relevant subband. Our final *Bayesian* threshold becomes as,

$$\hat{\delta}_{Bayes}(\hat{\sigma}_X) = \frac{\hat{\sigma}^2}{\hat{\sigma}_X} \tag{3.16}$$

where

$$\hat{\sigma}_X = \sqrt{max\left(\hat{\sigma}_Y^2 - \hat{\sigma}^2, 0\right)} \tag{3.17}$$

In Eq. 3.17 if $\hat{\sigma}^2 \geq \hat{\sigma}_Y^2$ then $\hat{\sigma}_X$ becomes zero and makes the Eq. 3.16 ∞. In that case we practically set the threshold, $\hat{\delta}_{Bayes}(\hat{\sigma}_X) = max(|\omega_i|)$ which concludes all coefficients under threshold and set them to zero.

(GCV) The one more threshold calculation based on another MSE approximation is the *Generalized Cross Validation* (GCV) method. Minimization of *Generalized Cross Validation* asymptotically offers an optimal threshold as described in [12, 40, 41]. Furthermore GCV procedure does not require any noise level estimation as in Eq. 3.9. The definition of

the generalized cross validation:

$$GCV(\delta) = \frac{\frac{1}{N}\|\omega - \omega_\delta\|^2}{(N_0/N)^2} \tag{3.18}$$

where N_0 is the number of coefficients under the threshold and N is the total number of wavelet coefficients. In the study of [40] Jansen and Bultheel proved that the threshold that minimizes the Eq. 3.18 is asymptotically optimal for a large number of coefficients and also minimizes the Eq. 3.4.

$$\delta_{GCV} = \underset{\delta}{\text{argmin}} GCV(\delta) \tag{3.19}$$

The both functions Eq. 3.18 and Eq. 3.4

$$\underset{\delta}{\text{argmin}} GCV(\delta) \approx \underset{\delta}{\text{argmin}} MSE(\delta)$$

have approximately the same minimum points for the same value of δ as $N \to \infty$. As it used to be in SURE procedure, with a certain accuracy of Fibonacci Search algorithm was performed to minimize Eq. 3.19. Since it is proven that the wavelet transform of a stationary correlated noisy signal is again stationary at each resolution level [41]. Accordingly the GCV method can be both applied to correlated and uncorrelated noisy images by the resolution-level dependent choice of the threshold in three different type of subbands or components such as horizontal, vertical and diagonal.

3.3.2 Objective Assessments for Performance Measuring in Wavelet Denoising

Different wavelet denoising algorithms are compared based on the following criteria:

(PSNR)

The objective image quality of the reconstruction is determined by Peak Signal-to-Noise Ratio. It is a full-reference measure to show quantitative results for comparison and it can be obtained in decibel unit, dB, by using the following [42]:

$$PSNR = 10\log_{10}\frac{(L-1)^2}{MSE} \tag{3.20}$$

where L is the dynamic range of pixel intensities. For our case grayscale images are represented by 8-bit therefore $(L-1) = 255$. MSE is the mean square error between original and the denoised image and it is calculated as in Eq. 3.4 where all image pixels are treated equally and calculation does not reflect the image content and structural features.Higher PSNR indicates better denoising performance.

(HMD)

Homogeneity Mean Difference is an objective full-reference metric which was proposed by [43, 44] to accurately describe the visual quality and to measure the performance of denoising methods together with contrast enhancement algorithms. HMD uses the homogeneity property of an image in which the local structural information of each pixel specifies the regional uniformity. HMD is defined by three terms: the edge value, local standard deviation and entropy of each pixel.

Let $x_{i,j}$ denote the gray level intensity of a pixel at the position of (i, j) in an image $\mathbf{X}$ of size $n \times m$. A window, $w_{i,j}$, of size $d \times d$ is centered at (i, j) for calculating those three terms:

1. The Edge Value is calculated by using Sobel Operator which uses two derivative kernels used for edge detection. The Sobel kernels are named after Irwin Sobel and they can be thought as 3×3 approximations to first derivatives of Gaussian kernels [45]. The edge value is defined by gradient magnitude as in:

$$e_{i,j} = \sqrt{g_{x_{i,j}}^2 + g_{y_{i,j}}^2} \tag{3.21}$$

where $g_{x_{i,j}}$ and $g_{y_{i,j}}$ are two separate measurements of gradient components and each point contains the horizontal and vertical derivative approximations respectively. Two 3×3 Sobel kernels which are convolved with the original image,

$$\mathbf{G}_x = \{g_{x_{i,j}}\} = \begin{bmatrix} -1 & 0 & 1 \\ -2 & 0 & 2 \\ -1 & 0 & 1 \end{bmatrix} \star \mathbf{X} \tag{3.22}$$

$$\mathbf{G}_y = \{g_{y_{i,j}}\} = \begin{bmatrix} 1 & 2 & 1 \\ 0 & 0 & 0 \\ -1 & -2 & -1 \end{bmatrix} \star \mathbf{X} \tag{3.23}$$

where $\star$ denotes the 2-dimensional convolution. These two gradient components are then combined together in Eq. 3.21 to find the absolute magnitude at each point.

2. The Local Standard Deviation is computed as

$$s_{i,j} = \sqrt{\frac{1}{d^2} \sum_{p=i-\left(\frac{d-1}{2}\right)}^{i+\left(\frac{d-1}{2}\right)} \sum_{q=j-\left(\frac{d-1}{2}\right)}^{j+\left(\frac{d-1}{2}\right)} \left(x_{p,q} - \mu_{i,j}\right)^2} \tag{3.24}$$

where $0 \leq i \leq (n-1)$ and $0 \leq j \leq (m-1)$ and $\mu_{i,j}$ is the mean of intensity values inside window $w_{i,j}$.

3. The Entropy is a measure for the amount of information in an image [46]. Consider the pixel in the centre of $d \times d$ window $w_{i,j}$. The probability of each pixel in the window, we firstly compute the histogram of the window $w_{i,j}$. The number of pixels in $w_{i,j}$ will

be $N_w = d^2$. The probability of pixel $w_{i,j}$ denoted by p_k is given by,

$$p_k = \frac{n_k}{N_w} \tag{3.25}$$

where n_k is the number of pixels that have the same intensity as $w_{i,j}$ pixel has. The local entropy of a pixel is computed as

$$h_{i,j} = -\sum_{k=1}^{N_w} p_k \log_2 p_k \tag{3.26}$$

where k represents the index of the intensity levels of the pixels inside window $w_{i,j}$. Hence $h_{i,j}$ is the entropy of its neighbours including itself. For each centre point in the window Eq. 3.26 gives the uncertainty of the image structure in the local neighbourhood $w_{i,j}$.

After obtaining three terms we normalize each term for computation consistency:

$$E_{i,j} = \frac{e_{i,j}}{\max\{e_{i,j}\}}, S_{i,j} = \frac{s_{i,j}}{\max\{s_{i,j}\}}, H_{i,j} = \frac{h_{i,j}}{\max\{h_{i,j}\}} \tag{3.27}$$

Then using these normalized three terms the value of homogeneity (HO) of a pixel at the location of (i, j) is calculated as:

$$\begin{aligned} HO_{i,j}(\mathbf{X}) &= \overline{E}_{i,j} \cdot \overline{S}_{i,j} \cdot \overline{H}_{i,j} \\ &= (1 - E_{i,j}) \times (1 - S_{i,j}) \times (1 - H_{i,j}) \end{aligned} \tag{3.28}$$

Lastly HMD is obtained by taking the difference between the mean homogeneities of processed and reference images.

$$HMD(\mathbf{X}, \mathbf{Y}) = \frac{1}{M \times N} \sum_{(i,j=0)}^{(M-1,N-1)} \left| HO_{i,j}(\mathbf{X}) - HO_{i,j}(\mathbf{Y}) \right| \tag{3.29}$$

where $HO_{i,j}(\mathbf{X})$ and $HO_{i,j}(\mathbf{Y})$ denote the homogeneity values of pixels at (i,j) in the input $\mathbf{X}$ and the processed output $\mathbf{Y}$ image, respectively. As stated in [43, 44] HMD is insensitive to

contrast enhancement but sensitive to the performance of denoising filters hence it is suitable for using as an objective criterion. HMD increases up to 1 with the noise level and when there is no noise it becomes zero.

(Q Metric)

This is a no-reference image content measure proposed in [13] based on the singular value decomposition (SVD) of local image gradients. Q Metric is sensitive to any type of noise and it does not require a reference image for calculation but using only anisotropic patches of the input image. It produces an indication about the content of the noise-free image such as sharpness and edge properties regardless of noise. Consider an image of interest $\mathbf{P} = \{p_{i,j}\}$ and the image gradient matrix is formed from the differences in pixels. The gradient matrix of a region within an $N \times N$ local analysis window $w_{i,j}$ is defined as:

$$\mathbf{G} = \begin{bmatrix} \vdots & \vdots \\ p_i(k) & p_j(k) \\ \vdots & \vdots \end{bmatrix}, \quad k \in w_{i,j} \tag{3.30}$$

where $[p_i(k), p_j(k)]^T$ is the gradient vector of the image at the location of (i_k, j_k). The SVD of the gradient matrix $\mathbf{G}$ results with the dominant orientation of the local window given by:

$$\mathbf{G} = \mathbf{USV}^T = \mathbf{U} \begin{bmatrix} s_1 & 0 \\ 0 & s_2 \end{bmatrix} [\mathbf{v_1 v_2}]^T \tag{3.31}$$

where $\mathbf{U}$ and $\mathbf{V}$ are the orthogonal matrices. The singular column vector $\mathbf{v_1}$ is the dominant orientation of the local gradient field and the second singular vector $\mathbf{v_2}$ which is the direction orthogonal to $\mathbf{v_1}$ represents the dominant edge orientation of the patch. The singular values $s_1 \geq s_2 \geq 0$ are the energy in the dominant orientation $\mathbf{v_1}$ and its perpendicular direction $\mathbf{v_2}$, respectively. The singular values can be seen as the strength of the gradients along both directions and they are easily affected by noise [14]. Furthermore the value of s_1 varies proportionally with the standard deviation σ of the corrupted noise. s_1 can serve as a sharpness metric, but cannot distinguish quality decay against high frequency behavior due to noise.

The definition of the Q metric is:

$$Q = s_1 \frac{s_1 - s_2}{s_1 + s_2} \tag{3.32}$$

with regard to s_1 there is normalizing quantitiy named as *coherence*

$$R = \frac{s_1 - s_2}{s_1 + s_2} \tag{3.33}$$

The coherence R shows the relative size between s_1 and s_2 and it is used to determine patch characteristics and to measure quantity for locally dominant orientation of patches. For some patches s_1 is significantly greater than s_2 and the value of Q drops with respect to noise level hence such structured patches (where $s_1 \gg s_2$) are called as *anisotropic*. For a noise-free anisotropic patch such as an edged patch, the absence of noise makes the value of R equal to near 1. The presence of noise drops that R value which means that the patch is less structured. However for *isotropic* patches that is $s_1 \approx s_2$ and $R = 0$ the Q metric is not able to reflect the image content. Therefore Q metric is only calculated for anisotropic patches where the calculated R for the patch is compared with a predefined threshold τ. If the local coherence $R \geq \tau$ then it is labeled as "anisotropic". τ depends on a significance parameter $0 < \delta < 1$ and their relation expressed by the integration of the pdf of R in [13], the result is:

$$\delta = \left(\frac{1 - \tau^2}{1 + \tau^2} \right)^{N^2 - 1} \tag{3.34}$$

In brief the total procedure of computing Q metric for a given image can be summarized as:

1. Noisy input image is divided into M non-overlapping patches of size $N \times N$ (for our case $N = 8$)

2. The local coherence values, R_k are calculated for each patch $k = 1, \ldots, M$ by using Eq. 3.33

3. Threshold in Eq. 3.34 is calculated for a determined significance level (for our case $\delta = 0.001$) and using this threshold level identify each patch whether "anisotropic" or

not as $R_k \geq \tau$.

4. Calculate the Q_k metric using Eq. 3.32 for each anisotropic patches. $Q_k = 0$ for isotropic patches.

5. Output the final metric value for whole image using $Q = \frac{1}{M}\sum_{k=1}^{M} Q_k$

For any given image the Q metric reduces with respect to noise level or when the image becomes blurry and it is most suitable for parameter tuning of denoising algorithms.

(SSIM)

Structure Similarity Index Measure is a full-reference method for measuring image quality and likeness between original and enhanced image by using three characteristics of an image: luminance measure, contrast measure and structure measure. The overall index is a multiplicative combination of three terms and noise is regarded as a distortion by SSIM. The definition of the index is [47]:

$$SSIM(\mathbf{X},\mathbf{Y}) = \frac{(2\mu_X\mu_Y + C_1)(2\sigma_{XY} + C_2)}{(\mu_X^2 + \mu_Y^2 + C_1)(\sigma_X^2 + \sigma_Y^2 + C_2)} \tag{3.35}$$

where μ_X is the mean intensity of the input reference image $\mathbf{X}$, μ_Y is the mean intensity of the output enhanced image $\mathbf{Y}$, σ_X and σ_Y are the standard deviations, σ_{XY} is the cross-covariance of the input and output images. C_1 and C_2 are the constants where taken as $C_1 = (k_1 L)^2$ and $C_2 = (k_2 L)^2$. In this study other constants are taken as $k_1 = 0.01$, $k_2 = 0.03$ and L is the dynamic range of the pixel values and is 255 for 8-bit grayscale images. The SSIM value between two images $\mathbf{X}$ and $\mathbf{Y}$ is in the range of $[0,\ 1]$. If both images are identical the index becomes 1 and if they are uncorrelated the index goes towards zero.

3.4 Denoising of CLSM Images Using 2D-DWT

Design of the experiment (DOE) is a systematic and rigorous approach to evaluate the efficiency and the effectiveness of multiple factors on our denoising performance [48]. Hence DOE will be used for analyzing the effect of several tuning parameters of 2D-DWT on the performance of denoising confocal images measured by different image quality measures.

3.4.1 Factors affecting the performance of 2D-DWT

Despite the fact that the performance of an algorithm is affected by various parameters. Inherently it is essential to give full attention to those which are expected to have a significant effect. As follows, the first step is to describe these parameters and their levels. The identified factors used within this study together with their selected levels are shown in Table 3.1 and are mentioned in the following.

Decomposition Levels: The wavelet decomposition level is an effective factor in denoising and it influences the result. In the first level, the original image signal using 2D-DWT is decomposed into 4 sub-bands, namely approximations (i.e. LL) and details (i.e. HH,HL and LH) by using a successive low-pass and high-pass filtering. The maximum level of 2D-DWT depends on how many data points contained in a data set, due to the down-sampling operation by 2 from one level to another. We introduced four different levels that are from J=1 up to J=4 and they are selected for this factor.

Wavelet Bases: The next step in denoising procedure is the selection of the appropriate wavelet function. There are many functions available however we included the well-known orthogonal and biorthogonal wavelets such as the Daubechies family, the least asymmetric families of Symmlets and Coiflets and the discrete approximation of the Meyer wavelet.

If you painted a picture with a sky, clouds, trees, and flowers, you would use a different size brush depending on the size of the features. Wavelets are like those brushes.

Ingrid Daubechies

As Daubechies stated that the given wavelet is capable of representing the signal and in addition to theoretical knowledge, choosing the proper wavelet is a ticklish experimental

approach. So one should test the performance of the different wavelets with the image signal due to the fact that different types of signals behave differently. In regard to a study [49] in which various wavelet bases are compared to their performances (PSNR) in image denoising, the wavelet families are restricted and are picked among them. We evaluated nine wavelet basis functions such as: Daubechies (db4, db8 with four and eight vanishing moments), Symmlets (sym8, sym12 with eight and twelve vanishing moments), Coiflets (coif4, coif5 with four and five vanishing moments), Biorthogonal (bior4.4, bior6.8 with four and six primal and four and eight dual vanishing moments) and discrete Meyer (dmey) wavelets are used as seen in Table 3.1.

Threshold Calculation Methods: Several methods are performed to make an optimal choice of threshold in the denoising algorithm. The aim of this study is also to find out the best method on confocal images. Five threshold calculation methods are comprised of *VisuShrink*-Universal with hard thresholding and Universal with soft thresholding, *SureShrink*, *BayesShrink* and *GCVShrink*. They are investigated with different performance metrics for the denoising confocal images. Hard thresholding is only used for Universal threshold method. In compliance with that the rest of methods has only been proposed for use with soft thresholding, the hard thresholding is only reserved for the Universal threshold calculation method.

Threshold Types: Besides the thresholding function and its calculation, the application also concerns the quality of denoising techniques. Different threshold application methods could lead to different results. Therefore, it is important to understand the application area of thresholds on detail coefficients. The first one is the global-threshold (unique) in which the threshold value is calculated uniquely for all wavelet coefficients of the noisy image [50]. The second type refers level-dependent coefficients and the threshold value is selected differently for each level [11,39]. In the last type, subband-adaptive detail-thresholds are calculated and each detail wavelet coefficient has its own threshold value [8]. In this study all of these three threshold types are considered and will be investigated as levels of this selection factor.

Table 3.1
Factors and their levels

Factors	Levels
Decomposition Level	J=1,2,3 and 4
Wavelet Base Type	db4, db8, sym8, sym12, coif4, coif5, bior4.4, bior6.8 and dmey
Threshold Calculation Method	Universal-Hard, Universal-Soft, SURE, Bayes and GCV
Threshold Type	Global, Level and Detail

3.5 Image Contrast Enhancement

Low contrast decreases human perception of details hidden in CLSM images and need to be resolved for improving visual quality of images acquired with poor illumination. In this part several contrast enhancement methods are performed that changes the pixel intensities of the input image in order that the output image subjectively and objectively looks better or provides much perception required.

3.5.1 HE - Histogram Equalization

The procedure of HE is widely used and easy to implement. It is simply done by reassigning the pixel values of gray levels based on their probability distribution [42]. The probability density function (pdf), $p(X_i)$ is defined as

$$p(X_i) = \frac{n_i}{N} \tag{3.36}$$

where $i = 0, 1, \ldots, L-1$ and n_i represents the total number of pixels that is equal to the value i and $N = n \times m$ is the total number of pixels in the input image. Therefore it stretches the dynamic range of the image histogram and results with redistribution pixels values on the overall histogram. Let $\mathbf{X} = \{x_{i,j}\}$ denote the intensity levels of the image where $x_{i,j}$ represents the gray level of a pixel at the spatial domain (i, j) and it is composed of L discrete gray levels ($L = 256$) in the range of $[0,\ (L-1)]$ and denoted as $x_{i,j} \in \{X_0, X_1, \ldots, X_{L-1}\}$. The cumulative distribution function (cdf), $c(X_i)$, is defined by using Eq. 3.36

$$c(X_i) = \sum_{k=0}^{i} p(X_k) \tag{3.37}$$

cdf is used as a transformation function to map the input image into dynamic range $[X_0,\ X_{L-1}]$ and $c(X_{L-1}) = 1$ by definition. Let $f(X_i)$ be a transformation function defined as

$$f(X_i) = X_0 + (X_{L-1} - X_0)c(X_i) \tag{3.38}$$

The histogram equalized image, $\mathbf{Y} = \{y_{i,j}\}$, can be expressed as

$$\mathbf{Y} = \lfloor f(\mathbf{X}) \rfloor = \lfloor f(x_{i,j}) \mid \forall x_{i,j} \in \mathbf{X} \rfloor \tag{3.39}$$

where $\lfloor . \rfloor$ is floor function that rounds each element to the nearest integer less than or equal to that element. The Eq. 3.38 spreads the histogram of the input image hence histogram equalized image will be enlarged and span whole range of the gray scale. HE ends up with a significant brightness change because of the homogeneous bright or dark areas in the background and it can make some parts of the input image too bright in which some details may disappear due to decreased gray levels of the over-enhanced image. All along the HE, minor gray levels in the histogram are neglected so that causing the loss of information such as artifacts, false contours and unnatural over-enhancement which degrades visual quality of the image. HE has also a "mean shift" problem, it shifts mean brightness of the input image to the middle gray level of the intensity range regardless of the input mean [42]. The output of the HE produces an image who pixel values have a uniform density

$$p(x) = \frac{1}{X_{L-1} - X_0} \tag{3.40}$$

where $x = X_i$ and $X_0 \leq x \leq X_{L-1}$. The mean brightness of the output image is always equal to

$$E(\mathbf{Y}) = \int_{X_0}^{X_{L-1}} x p(x) dx = \frac{1}{2}(X_0 + X_{L-1}) \tag{3.41}$$

in which $E(\mathbf{Y}) = X_G$ is the middle gray level of $[X_0,\ X_{L-1}]$. Since the HE does not preserve the mean brightness and it tends to drastically change the brightness, better contrast algorithms have been proposed based on the HE to overcome saturation problem .

3.5.2 CLAHE - Contrast Limited Adaptive Histogram Equalization

HE overenhances image by increasing visibility of noise in input image. CLAHE is an adaptive extension of HE and it adapts local contrast requirements and minor contrast

differences [17]. The algorithm was invented for medical imaging to overcome limitations of HE for low-contrast images [18]. The input image is divided into contextual regions (sub-images) in which adaptive HE is applied separately plus with histogram clipping and redistribution of local contextual histogram values over clip-limit. In this study input image is divided to 8×8 contextual regions. For every pixels in each single region local histograms

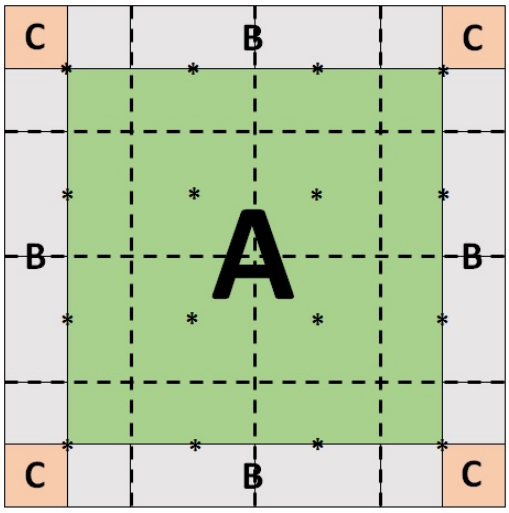

Figure 3.11 Region-based Interpolation in CLAHE. Image division is 4×4 in this example and each star shows the middle point of its related region. The green region marked as A is the centre area where bi-linear interpolation is applied. The khaki region marked as B is the border area where only linear interpolation takes place and finally the red region marked as C is the corner area where pixels are left as they are.

are calculated. To reduce the noise enhancement we use contrast limitation, a clip-limit, which determines the maximum point histogram can take. The histogram values over the clip-limit are uniformly redistributed in all histogram bins and this can cause some bins to be pushed over the clip-limit again. The procedure of clipping and redistributing of that portion are performed many times until bins cannot exceed an effective clip-limit as it can be seen in Figure 3.12. After obtaining clipped and equally distributed local histograms, the corresponding cumulative histograms (cdf) are calculated to perform gray-level assignment same as in the procedure of HE. Lastly to avoid artifacts arising from the neighboring regions the new pixel values are calculated by bi-linear interpolation according to each of the surrounding contextual regions. The points A, B, C and D in Figure 3.13 are the centre of the regarding contextual regions. Let $f_A(x_{i,j})$, $f_B(x_{i,j})$, $f_C(x_{i,j})$ and $f_D(x_{i,j})$ be region-specific gray-level transformation functions which are based on local histograms. The pixel intensity is $x_{i,j}$ and its bi-linear interpolated new gray value is calculated by using transformation

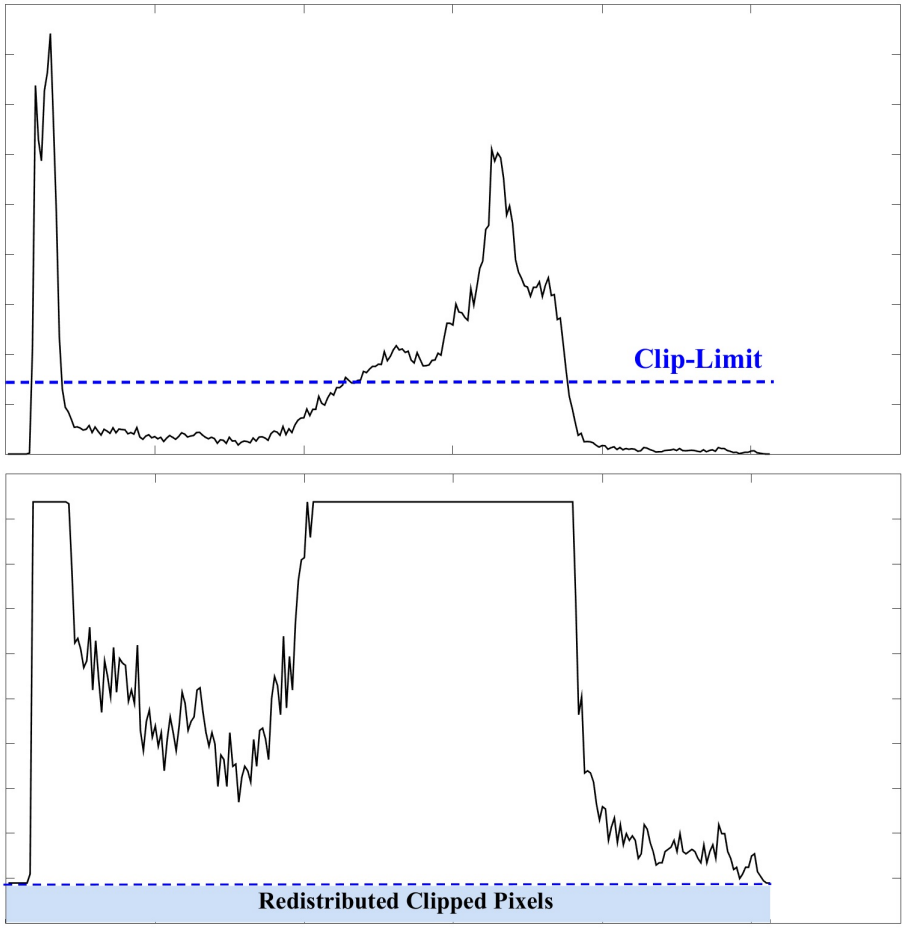

Figure 3.12 Original and Clipped Histograms

functions of neighboring regions as

$$\begin{aligned} \hat{x}_{i,j} &= (1-b)\left[(1-a).f_A(x_{i,j}) + a.f_B(x_{i,j})\right] \\ &\quad + b.\left[(1-a).f_C(x_{i,j}) + a.f_D(x_{i,j})\right] \end{aligned} \tag{3.42}$$

where a and b are normalized distances with respect to centre point (i.e. A) of upper-left region. Interpolation is performed in three different ways based on areas seen in Figure 3.11. The inner green area is subjected to Eq. 3.42. Pixels in the khaki-coloured side parts are only linearly interpolated. Remaining corner pixels in the red area are left as they are just transformed with their related region-based transformation function. At the end resulting output image is continuous and boundary artifacts are removed. In brief CLAHE procedure can be summarized as

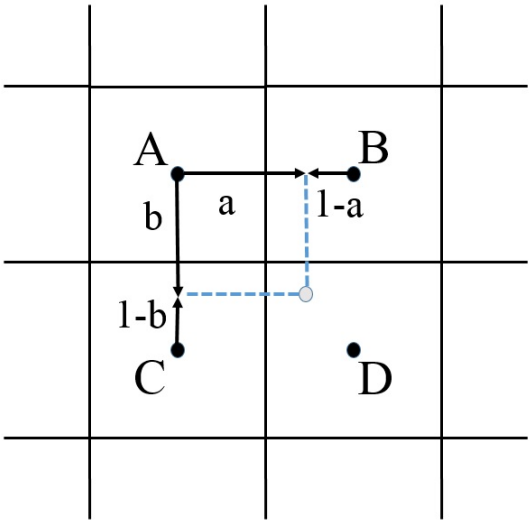

Figure 3.13 The gray-level assignment at the pixel position by a white dot. Bi-linear interpolation using neighboring contextual regions.

1. Divide the input image into contextual regions (blocks) seen in Figure 3.11. The number of blocks is chosen as 8×8 for our case.

2. Local histograms are calculated for each block then clipping and redistribution are performed for the local histograms of each region.

3. Local cdfs are calculated based on local image data to transform pixel values as the same as in HE.

4. Interpolation performed to remove boundary artifacts due to region based HE

The main parameters of CLAHE are the clip-limit and the number of blocks (i.e. contextual regions). The clip-limit avoids the over-amplification of noise. The use of contextual regions provides better contrast enhancement because it spatially ignores pixels that have little effects.

3.5.3 BBHE - Brightness preserving Bi-Histogram Equalization

Another method has been proposed by [20] to overcome the brightness problem of HE. Keeping the mean brightness of the image reduces the saturation effect and prevents

artifacts of the output image. BBHE firstly divides pixel intensity values of the input image into two parts by using its mean. Then it performs a typical HE procedure and uniformly equalizes two sub-images independently. Let X_m be the brightness mean of input image $\mathbf{X}$

$$E(\mathbf{X}) = \sum_{k=0}^{L-1} k.p(X_k) = \mu_{\mathbf{X}} \tag{3.43}$$

and $X_m = \lfloor \mu_{\mathbf{X}} \rfloor \in \{X_0, X_1, \ldots, X_{L-1}\}$. Using this X_m value input image is split into two subsets as $\mathbf{X_L}$ and $\mathbf{X_U}$ and after this separation two parts are independently equalized by HE.

$$\begin{aligned} & \mathbf{X} = \mathbf{X_L} \cup \mathbf{X_U} \\ \text{where} \quad & \mathbf{X_L} = \{x_{i,j} \mid x_{i,j} \leq X_m, \forall x_{i,j} \in \mathbf{X}\} \\ & \mathbf{X_U} = \{x_{i,j} \mid x_{i,j} > X_m, \forall x_{i,j} \in \mathbf{X}\} \end{aligned} \tag{3.44}$$

Then, the corresponding pdf of both parts are given by

$$p_L(X_i) = \frac{n_L^i}{N_L} \quad \text{for} \quad i = 0, 1, \ldots, m \tag{3.45}$$

$$p_U(X_i) = \frac{n_U^i}{N_U} \quad \text{for} \quad i = m+1, m+2, \ldots, L-1 \tag{3.46}$$

in which n_L^i and n_U^i represents the number counts of pixels that is equal to the value of i and the total numbers of pixels in two subset $\mathbf{X_L}$ and $\mathbf{X_U}$ are $N_L = \sum_{i=0}^{m} n_L^i$ and $N_U = \sum_{i=m+1}^{L-1} n_U^i$ where $N = N_L + N_L$.

In common with the HE method both respective cdfs are computed to be used in transformation function

$$c_L(X_i) = \sum_{k=0}^{i} p_L(X_k) \quad \text{for} \quad i = 0, 1, \ldots, m \tag{3.47}$$

$$c_U(X_i) = \sum_{k=m+1}^{i} p_U(X_k) \quad \text{for} \quad i = m+1, \ldots, L-1 \tag{3.48}$$

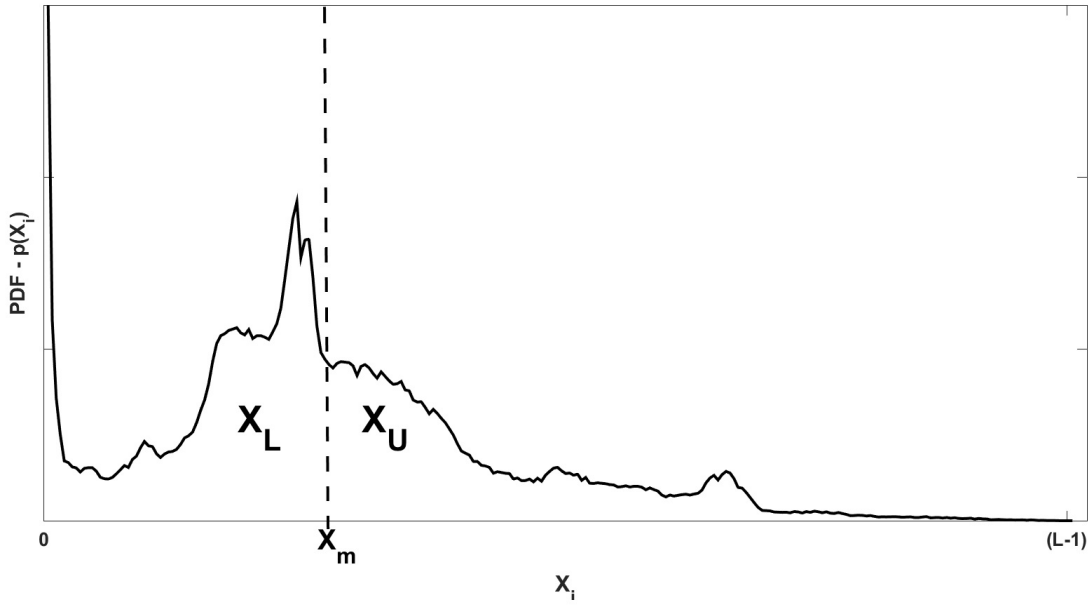

Figure 3.14 The division of input image histogram into two portions based on X_m

where $c_L(X_m) = c_L(X_{L-1}) = 1$ by definition. Based on these cdfs following transformation functions for lower and upper part become

$$f_L(X_i) = X_0 + (X_m - X_0)c_L(X_i) \tag{3.49}$$

$$f_U(X_i) = X_{m+1} + (X_{L-1} - X_{m+1})c_U(X_i) \tag{3.50}$$

The resulting histogram equalized output image using two sub-image, $\mathbf{Y} = \{y_{i,j}\}$ can expressed as

$$\mathbf{Y} = \lfloor f_L(\mathbf{X_L}) \cup f_U(\mathbf{X_U}) \rfloor \tag{3.51}$$

$$\text{where} \quad f_L(\mathbf{X_L}) = \{f_L(x_{i,j}) \mid \forall x_{i,j} \in \mathbf{X_L}\} \tag{3.52}$$

$$f_U(\mathbf{X_U}) = \{f_U(x_{i,j}) \mid \forall x_{i,j} \in \mathbf{X_U}\} \tag{3.53}$$

As a result the sub-images $\mathbf{X_L}$ and $\mathbf{X_U}$ are equalized in the range of $[X_0, X_m]$ and $[X_{m+1}, X_{L-1}]$ respectively. The mean brightness of the BBHE output image is equal to

$$\begin{aligned} E(\mathbf{Y}) &= E(\mathbf{Y} \mid \mathbf{X} \leq X_m) Pr(\mathbf{X} \leq X_m) \\ &\quad + E(\mathbf{Y} \mid \mathbf{X} > X_m) Pr(\mathbf{X} > X_m) \end{aligned} \tag{3.54}$$

as in the same manner in Eq. 3.41 one can also obtain by substituting $Pr(\mathbf{X} \leq X_m) = Pr(\mathbf{X} > X_m) = c(X_m) = \frac{1}{2}$ into Eq. 3.54

$$\begin{aligned} E(\mathbf{Y} \mid \mathbf{X} \leq X_m) &= \frac{1}{2}(X_0 + X_m) \\ E(\mathbf{Y} \mid \mathbf{X} > X_m) &= \frac{1}{2}(X_m + X_{L-1}) \end{aligned}$$

and it ends up with

$$E(\mathbf{Y}) = \frac{1}{2}(X_G + X_m) \tag{3.55}$$

which also depends on the mean of the input image X_m. This shows that BBHE produces an output image whose mean is always equal to the average of the middle gray level (X_G) and the image mean (X_m).

3.5.4 MMBEBHE - Minimum Mean Brightness Error Bi-Histogram Equalization (modified version of BBHE)

This method is proposed by [21] to take BBHE a step further. Since in BBHE the histogram of $\mathbf{X}$ is assumed to be a symmetrical around X_m so using the mean brightness does not always offer the best brightness preservation. X_m can be seen as a histogram threshold that splits it in two portion. Instead of using X_m MMBEBHE proposes a technique to determine a threshold X_T in order to minimize and approximate the absolute mean brightness error (AMBE) in Eq. 3.77. Starting with the approximation of the output mean, let's denote $E_T(\mathbf{Y})$ as the output mean with any histogram threshold X_T. As in Eq. 3.54 it can be written

as

$$\begin{aligned} E_T(\mathbf{Y}) &= E(\mathbf{Y} \mid \mathbf{X} \leq X_T) Pr(\mathbf{X} \leq X_T) \\ &\quad + E(\mathbf{Y} \mid \mathbf{X} > X_T) Pr(\mathbf{X} > X_T) \\ &= \frac{1}{2}(X_0 + X_T) \sum_{i=0}^{T} p(X_i) \\ &\quad + \frac{1}{2}(X_{T-1} + X_{L-1}) \sum_{i=T+1}^{L-1} p(X_i) \end{aligned} \tag{3.56}$$

and by substituting $X_{L-1} + 1 = L$ and changing indices using $\sum_{i=0}^{L-1} p(X_i) = 1$ hence we obtain

$$E_T(\mathbf{Y}) = \frac{1}{2}\left[(X_0 + X_T) + L\left(1 - \sum_{i=0}^{T} p(X_i)\right)\right] \tag{3.57}$$

If the threshold is set as X_{T+1} then Eq. 3.57 becomes

$$\begin{aligned} E_{T+1}(\mathbf{Y}) &= \frac{1}{2}\left[(X_0 + X_{T+1}) + L\left(1 - \sum_{i=0}^{T+1} p(X_i)\right)\right] \\ &= \frac{1}{2}\left[(X_0 + X_T) + L\left(1 - \sum_{i=0}^{T} p(X_i)\right)\right] + \\ &\quad \frac{1}{2}\left[1 - L.p(X_{T+1})\right] \\ E_T(\mathbf{Y}) &= E_{T-1}(\mathbf{Y}) + \frac{1}{2}\left[1 - L.p(X_T)\right] \\ \text{where} \quad & E_0(\mathbf{Y}) = \frac{1}{2}\left[2.X_0 + L(1 - p(X_0))\right] \end{aligned} \tag{3.58}$$

Mean Brightness Error (MBE) can be calculated for each threshold

$$\begin{aligned} MBE_T &= E_T(\mathbf{Y}) - E(\mathbf{X}) \\ MBE_0 &= \frac{1}{2}\left[X_0 + L(1 - p(X_0))\right] - E(\mathbf{X}) \\ MBE_1 &= E_1(\mathbf{Y}) - E(\mathbf{X}) \\ &= E_0(\mathbf{Y}) + \frac{1}{2}\left[1 - L.p(X_1)\right] - E(\mathbf{X}) \\ &= MBE_0 + \frac{1}{2}\left[1 - L.p(X_1)\right] \end{aligned} \tag{3.59}$$

which requires the initial value for $T = 0$ then the recursive expression with threshold level X_T can be written as

$$MBE_T = MBE_{T-1} + \frac{1}{2}[1 - L.p(X_T)] \tag{3.60}$$

Based on the derivations above, MMBEBHE algorithm is defined by the following steps

1. Calculate MBE in Eq. 3.60 for each level of threshold.
2. Determine X_T that yields minimum value of MBE
3. Based on X_T, perform the same procedure same as in BBHE

Consequently MMBEBHE is a good solution for enhancing asymmetrical input images $\mathbf{X}$ and it optimally produces minimum difference between input and output mean by choosing a histogram separating threshold X_T.

3.5.5 BHEPL - Bi-Histogram Equalization with Plateau Limited Value

In order to maintain the mean brightness BPHEPL, proposed by [19], is the another method that divides the histogram into two potions plus with clipping these sub-histograms based on the calculated plateau limit (i.e. clip-limit). BHEPL performs the same procedure of BBHE seen in Eq. 3.45 which uses X_m to obtain lower and upper histograms denotes as h_L and h_U. Then using two sub-histograms clip-limits denoted as T_L and T_U are determined for $\mathbf{X}_L$ and $\mathbf{X}_U$.

$$T_L = \frac{1}{X_m + 1} \sum_{i=0}^{m} h_L(X_i) \tag{3.61}$$

and

$$T_U = \frac{1}{(L-1) - X_m} \sum_{i=m+1}^{L-1} h_U(X_i) \tag{3.62}$$

Each limit is the average value of corresponding portion. Afterwards sub-histograms are clipped without redistributing excessive pixels and clipped histograms are denoted as h_{CL} and h_CU.

$$h_{CL}(X_i) = \begin{cases} h_L(X_i) & \text{if } h_L(X_i) \leq T_L \\ T_L & \text{elsewhere} \end{cases} \tag{3.63}$$

and

$$h_{CU}(X_i) = \begin{cases} h_U(X_i) & \text{if } h_U(X_i) \leq T_U \\ T_U & \text{elsewhere} \end{cases} \tag{3.64}$$

Clipping operation restricts the enhancement rate of BHEPL and prevents intensity saturation in the output image. The corresponding pdfs are calculated from the clipped sub-histograms by using

$$p_{CL}(X_i) = \frac{h_{CL}(X_i)}{N_{CL}} \quad \text{for} \quad i = 0,1,\ldots,m \tag{3.65}$$

$$p_{CU}(X_i) = \frac{h_{CU}(X_i)}{N_{CU}} \quad \text{for} \quad i = m+1,m+2,\ldots,L-1 \tag{3.66}$$

where $N_{CL} = \sum_{i=0}^{m} h_{CL}(X_i)$ and $N_{CU} = \sum_{i=m+1}^{L-1} h_{CU}(X_i)$ are total number of pixels in lower ($\mathbf{X}_L$) and upper ($\mathbf{X}_U$) portions respectively. The respective cdfs, $c_L(X_i)$ and $c_U(X_i)$, are computed as the same way in Eq. 3.48 to be used in transformation function

$$c_{CL}(X_i) = \sum_{k=0}^{i} p_{CL}(X_k) \quad \text{for} \quad i = 0,1,\ldots,m \tag{3.67}$$

$$c_{CU}(X_i) = \sum_{k=m+1}^{i} p_{CU}(X_k) \quad \text{for} \quad i = m+1,\ldots,L-1 \tag{3.68}$$

where $c_{CL}(X_m) = c_{CU}(X_{L-1}) = 1$ by definition. Based on these cdfs following transformation functions are defined as

$$f_{CL}(X_i) = X_0 + (X_m - X_0)c_{CL}(X_i) \tag{3.69}$$

$$f_{CU}(X_i) = X_{m+1} + (X_{L-1} - X_{m+1})c_{CU}(X_i) \tag{3.70}$$

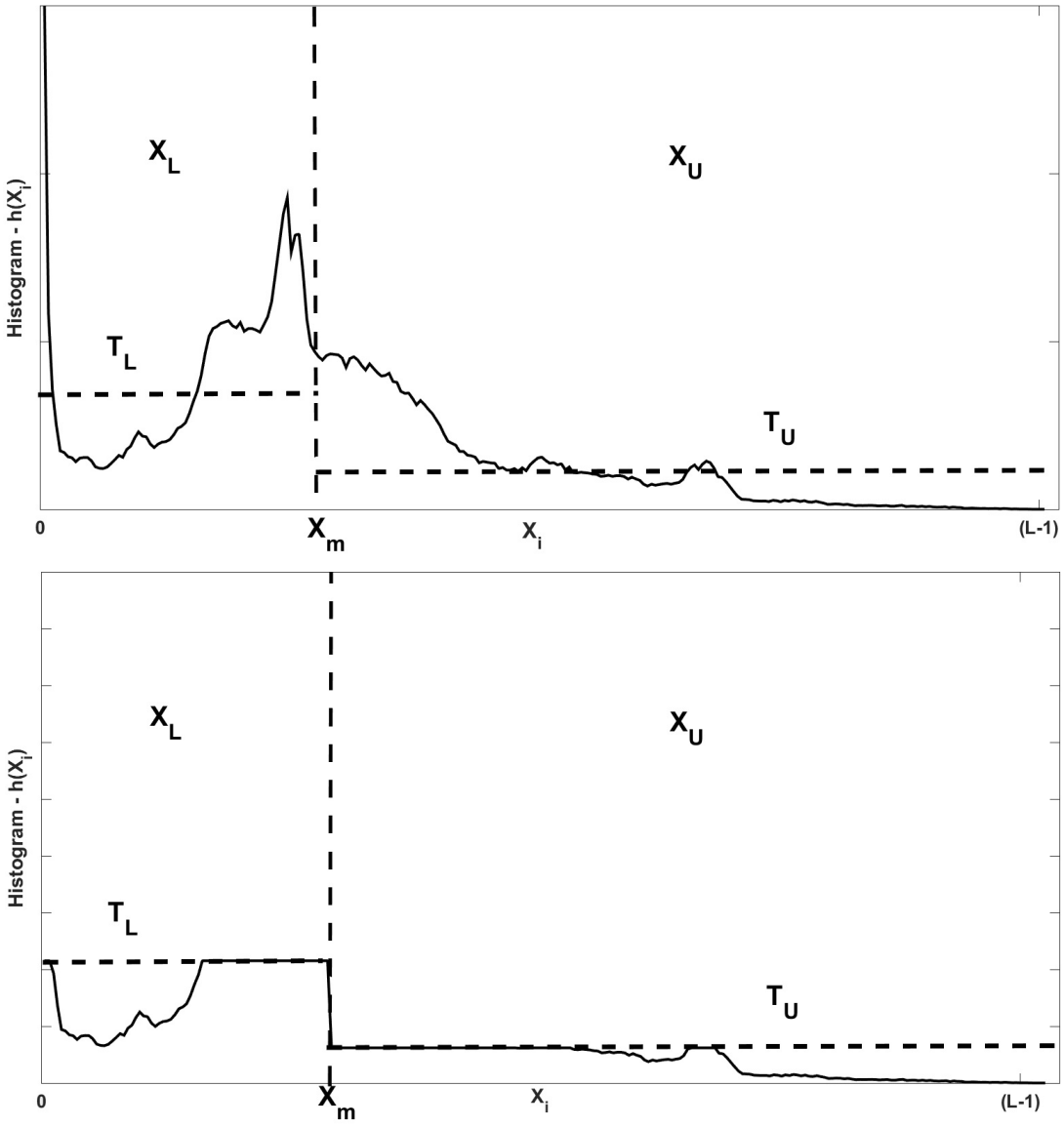

Figure 3.15 Original (above) and Clipped (below) Histograms. The original input histogram is divided into two portion based on X_m and two clip-limits are set to each portion. Then histogram is clipped without redistributing the clipped parts back into the histogram.

The resulting output image of BPEHL procedure, $\mathbf{Y} = \{y_{i,j}\}$ can be expressed as

$$\mathbf{Y} = \lfloor f_{CL}(\mathbf{X_L}) \cup f_{CU}(\mathbf{X_U}) \rfloor \tag{3.71}$$

where

$$f_{CL}(\mathbf{X_L}) = \{f_{CL}(x_{i,j}) \mid \forall x_{i,j} \in \mathbf{X_L}\} \tag{3.72}$$

$$f_{CU}(\mathbf{X_U}) = \{f_{CU}(x_{i,j}) \mid \forall x_{i,j} \in \mathbf{X_U}\} \tag{3.73}$$

BHEPL is a histogram clipping version of BBHE and the whole procedure of BHEPL can briefly be summarized as

1. Use X_m as a histogram separation point similar to BBHE and decompose input image into two sub-images $\mathbf{X}_L$ and $\mathbf{X}_U$ as done in Eq. 3.45.

2. Obtain the corresponding histograms of each part, h_L and h_U. Then set the average of portion as a clip-limit, T_L and T_U.

3. Perform clipping but no redistribution of excess pixels.

4. Calculate cdf for each clipped portion then apply transformation function.

3.5.6 Objective Assessments for Performance Measuring in Contrast Enhancement

Contrast by definition is a mean luminance difference between an object and its surrounding. Different quality metrics is used to show the performance of contrast enhancement procedures mentioned above.

(CIR)

Contrast Improvement Ratio is a full-reference measure for the quantification of contrast enhancement. It is defined as the ratio of the enhanced and original image within the region of interest (ROI) [51]:

$$CIR(\mathbf{X},\mathbf{Y}) = \frac{\sum\sum_{i,j\in ROI} \mid c_X(i,j) - c_Y(i,j) \mid^2}{\sum\sum_{i,j\in ROI} c_X(i,j)^2} \tag{3.74}$$

where c_X and c_Y are the local contrast values of the original and the enhanced image. In this study ROI is taken as the whole image. The local contrast $c_X(i,j)$ is defined by the difference of mean values in two different sized square windows centered on a pixel of (i,j) as seen

below

$$c_X(i,j) = \frac{|\,\mu_X^{3\times3}(i,j) - \mu_X^{7\times7}(i,j)\,|}{|\,\mu_X^{3\times3}(i,j) + \mu_X^{7\times7}(i,j)\,|} \tag{3.75}$$

$$\mu_X^{3\times3}(i,j) = \frac{1}{3^2}\sum_{k=-1}^{1}\sum_{l=-1}^{1} X(i+k,j+l)$$

$$\mu_X^{7\times7}(i,j) = \frac{1}{7^2}\sum_{k=-1}^{1}\sum_{l=-1}^{1} X(i+k,j+l)$$

where $\mu_X^{3\times3}$ and $\mu_X^{7\times7}$ are the average values of gray level pixels of image X in a 3×3 and 7×7 square window whose centre is located in (i,j). The contrast measure c is in the range of $[0,\ 1]$. The greater CIR value, the better contrast enhancement.

(EME)

The Measure of Enhancement, or the measure of improvement is a no-reference metric that indicates the contrast level of an image. Let the image $\mathbf{Y}$ be partitioned by $k_1 \times k_2$ blocks of $w_{k,l}$ of size $l_1 \times l_2$ pixels (8×8 is the chosen size for our case) and hence the definition is [52]

$$EME = \frac{1}{k_1 k_2}\sum_{k=1}^{k_1}\sum_{l=1}^{k_2} 20\log\frac{I^w_{max;k,l}}{I^w_{min;k,l}} \tag{3.76}$$

where $I^w_{max;k,l}$ and $I^w_{min;k,l}$ are the maximum and minimum pixel values in the window block $w_{k,l}$ of the enhanced image $\mathbf{Y}$. This metric simply measures the mean ratio between maximum and minimum intensities in decibels. Higher (EME) value generates a better contrast enhancement.

(AMBE)

Absolute Mean Brightness Error is the absolute difference and it is a full-reference measure to indicate brightness preservation of the processed image.

$$\begin{aligned} AMBE(\mathbf{X},\mathbf{Y}) &= \mid E(\mathbf{Y}) - E(\mathbf{X}) \mid \\ &= \mid \mu_{\mathbf{Y}} - \mu_{\mathbf{X}} \mid \end{aligned} \tag{3.77}$$

where $\mu_{\mathbf{Y}}$ and $\mu_{\mathbf{X}}$ is the mean intensity of the processed and original image respectively. At the stage of image contrast enhancement we desire minimum AMBE (i.e. ideally zero) for better brightness preservation.

(Entropy)

The total amount of information contained in an image is represented by the entropy. Entropy measure has been used for no-reference image quality assessment. For an image which has $L-1$ different gray levels and the probability of i_{th} gray level is p_i, the entropy of that gray level can be defined as the logarithm of the probability of long sequences [46]

$$e(i) = -p_i \log p_i \tag{3.78}$$

The total of each individual entropies of the whole image (X_i) at all gray levels, i.e. discrete entropy, is defined as [46]

$$H(x) = -\sum_{i=0}^{L-1} e(i) = -\sum_{i=0}^{L-1} p(x_i) \log p(x_i) \tag{3.79}$$

The discrete entropy delineates the abundance of the image details and concludes its maximum when it has a uniform distribution. The bigger entropy an image possesses, the more information and details of the image are.

4. RESULTS and DISCUSSION

This chapter deals with the comparison of the wavelet based denoising techniques with different tuning parameters. There are four methods calculated for determining the quality of denoised images which acts as a quantitative metric for comparison, namely, PSNR, HMD, Q-Metric, and SSIM.

4.1 Analysis of Results

This section presents the results of the 2D-DWT based image denoising experiments performed with different combinations of factors' levels. Four sets of experiments are implemented to screen out the effect of different factors on the performance of denoising algorithms for each test case, i.e. different noise levels. A confocal test image used in the experiment is borrowed from a database [34]. The existing noise amount is measured by using the estimator [15] and found out being $\sigma = 0.0224$ which is negligible. The noise-free image in Figure 3.8(c) is acquired from fixed and living heart tissue using a conventional laser-scanning confocal microscope (Zeiss LSM5 Duo; Zeiss, Jena, Germany) with a 40x oil immersion lens (NA 1.3). The first set of experiment examines the performance of the algorithm in terms of PSNR. The second deals with the HMD which describes the textual and structural information. The third one is a no-reference image metric named as Q-Metric based on the SVD of local image gradients. Q-Metric is sensitive to quality changes arising from blur and noise. The last set of the experiment is based on SSIM which compares patterns of pixel intensities for images. SSIM indicates the visual quality improvement and it provides a useful standard on how local image quality is improved over space. Experiments are performed on an Intel(R) Core(TM) i7 2.20 GHz with 8GB of RAM. Algorithms and analysis are executed with MATLAB Version 2016. Each experiment contains 20 replications for each of 540 different combinations in Table 3.1 according to levels which are considered for each factor. In the first part, the effect of various factors which we assume that are significant is determined. In the second part of this section, the values which are au-

thenticated as the best values for the significant parameters are applied to perform 2D-DWT denoising of various CLSM images both obtained from the database and our optical setup.

4.1.1 Analysis of Variance: PSNR

This section will first examine the main effects of decomposition level, i.e. J, wavelet base type, threshold calculation method and threshold type, as well as their interactions on the PSNR measure of obtained result. Totally, for each test case 10800 experiments are carried out (540 for a full factorial design times 20 replications). Table 4.1 shows the ANOVA results from the experiments. Table 4.1 consists of different test cases, i.e. noise levels such as $\sigma = \{5, 10, 15, 20\}$, F-ratio, and P-value of ANOVA. In comparison with the results, for the first test case, decomposition level is the most effective parameter in the algorithm and threshold calculation method and threshold type comes after it. Interaction of these three factors is also of importance too. For this reason, different combinations of these three factors lead to dissimilar performances of the algorithm. As the noise level in the image grows and the denoising problem becomes demanding, for the rest of problems the situation does not change so much but the importance of threshold method increases along with the noise level while other important factors start to loose their significance. For all cases, decomposition level is still the most important factor in the PSNR performance of the algorithm. The interaction between level and method bears more significance than before and it seems to be more important than other interactions and threshold type itself due to its higher F-ratio. In the meantime, the interaction between level and type loses its rank and lags behind. Threshold calculation method is still the second important factor.

To select the best suitable values for factors and to achieve best PSNR of the denoised images, it is necessary to survey averages of each treatment in Figures A.1 to A.4. As the problem is a maximization problem of the PSNR, the factor level should be selected that leads to maximum average. Figure A.1 shows the average results for each significant factor. As seen on the left side of Figure A.1, $J = 1$, GCV and Global can be the candidate as the best levels for decomposition level, threshold calculation method and threshold type, respectively, in the algorithm for this problem. Furthermore, interactions of these three factors are of

concern. When we examine in the right side of Figure A.1, the first two plots can verify that selecting $J = 1$ and Global leads to the best PSNR for the first case. But in the last plot, there is a disordinal (crossover) interaction, therefore, interpreting the main effects involving method and type would be misleading. We must look at the settings of two factors at once, rather than independent factors one at a time. Hence applying SURE method along with and $J = 1$ and Global leads to very good results for the first test case.

In the second test case with $\sigma = 10$ as the noise level increases the method GCV along with the type Detail shows better results than SURE with the type Global. The range of the mean plot of threshold type decreases. The interaction between level and method becomes more important.

For the third and the fourth cases, the threshold type becomes less important factor while the interaction between level and method outdistances the threshold type. As the noise level increases it becomes difficult to clean noise in the first level of decomposition, i.e. $J = 1$, so next decomposition level is needed. As seen in Figures A.3 and A.4, disordinal interaction shows that $J = 1$ is no longer capable of denoising and yielding better PSNR. The method GCV together with $J = 2$ and the type Detail performs better solution in maximizing PSNR.

Table 4.1
ANOVA results in regard to PSNR

	$\sigma = 5$		$\sigma = 10$		$\sigma = 15$		$\sigma = 20$	
	F-ratio	P-value	F-ratio	P-value	F-ratio	P-value	F-ratio	P-value
A	**34188.91**	0	**36155.78**	0	**33163.37**	0	**27917.93**	0
B	42.35	0	55.98	0	61.55	0	60.51	0
C	**12626.74**	0	**18109.48**	0	**20623.58**	0	**19608.58**	0
D	**9830.46**	0	**5447.79**	0	**3041.88**	0	**1593.79**	0
$A \times B$	23.42	0	27.66	0	29.79	0	30.59	0
$A \times C$	**1326.77**	0	**2563.11**	0	**3507.18**	0	**3927.70**	0
$A \times D$	**2152.22**	0	**1812.51**	0	**1453.66**	0	**1114.09**	0
$B \times C$	4.69	0	5.13	0	5.89	0	6.26	0
$B \times D$	5.86	0	6.27	0	5.89	0	5.02	0
$C \times D$	**1859.93**	0	**1699.09**	0	**1638.45**	0	**1493.46**	0

A: Decomposition Level, B: Wavelet Base Type, C: Threshold Calculation Method, D: Threshold Type

4.1.2 Analysis of Variance: HMD

For the study of HMD metric, the factors in this experiment are the same as the previous study, i.e., decomposition level, wavelet base type, threshold calculation method and threshold type as shown in Table 3.1. Again four different levels of noise are applied and for each case 10800 experiments are performed. In this experiment a full factorial design is used and factors and two-factor interactions are presented in the result. Table 4.2 shows the relevant ANOVA results.

All of the four test cases results coherently shows that decomposition level, threshold calculation method and threshold type have main impacts on the HMD. It is again obvious that decomposition levels have the most significant effect on HMD since they are heavily involved after every noise increment in the image and the denoising procedure demands a next level wavelet decomposition to clean out noise in wavelet coefficients in each decomposition level. For the selection of the best values, averages of levels of each significant factor are concerned and plotted in Figures A.5 to A.8. Despite PSNR and the following other metrics, this problem is a minimization problem. Thus, the level should be chosen that produces minimum average of HMD. In the first case $\sigma = 5$, decomposition level can be chosen as $J = 1$ by just looking at main effect plot but since there is a disordinal interaction in the right side of Figure A.5 we are not permitted to interpret the main effects involved in the interaction. For the rest of test cases $J = 2$ becomes more explicit. GCV can be selected as the best method yielding minimum hmd result for all cases. As seen from the ANOVA results, interaction between level and method starts to play main role rather than threshold type. Without regard to main effect of threshold type we can conclude that Level can be chosen as best choice for threshold type along with GCV. To sum up briefly $J = 2$, GCV and Level leads to the least HMD on average for all cases.

Table 4.2
ANOVA results in regard to HMD

	$\sigma = 5$		$\sigma = 10$		$\sigma = 15$		$\sigma = 20$	
	F-ratio	P-value	F-ratio	P-value	F-ratio	P-value	F-ratio	P-value
A	**16619.87**	0	**16788.58**	0	**23214.11**	0	**31399.44**	0
B	2.72	0.0054	7.36	0	17.41	0	34.08	0
C	**5913.22**	0	**8214.69**	0	**13100.05**	0	**19300.90**	0
D	**2007.33**	0	**985.38**	0	**1030.63**	0	**1422.54**	0
$A \times B$	2.51	0.0001	5.16	0	9.23	0	16.17	0
$A \times C$	**1449.38**	0	**2477.10**	0	**4485.64**	0	**7181.82**	0
$A \times D$	**1036.03**	0	**714.05**	0	**834.54**	0	**1112.93**	0
$B \times C$	2.44	0	3.32	0	6.45	0	9.87	0
$B \times D$	0.83	0.6515	0.60	0.8877	1.55	0.0726	1.78	0.0277
$C \times D$	**1390.91**	0	**1176.77**	0	**1060.28**	0	**884.00**	0

A: Decomposition Level, B: Wavelet Base Type, C: Threshold Calculation Method, D: Threshold Type

4.1.3 Analysis of Variance: Q-Metric

In this problem maximizing Q-metric is our goal. According to the ANOVA results including same test procedures applied to Q-Metric outcomes the situation in the first test case is different for wavelet base type which firstly rises to the importance ranking by outstripping threshold type. However along with the noise level it is left behind by threshold type. $J = 2$, bior6.8 and GCV are effective parameters in the first case. For the second and third problem the situation is different. $J = 2$ is still the most important factor; however the interaction between method and threshold type bears more significance. Consideringly taking account of the disordinal interaction in Figures A.10 and A.11 we can conclude selecting Universal-Soft, $J = 2$ and Global for the second and third test case. For the last one again by concerning the disordinal interaction $J = 3$ slightly moves ahead and plays more important role in maximizing Q-metric. As a result $J = 3$, Universal-Soft and Detail are selected as the best values.

4.1.4 Analysis of Variance: SSIM

In this experiment ANOVA results for full factorial design is shown in Table 4.4. For the first three cases threshold type have main impacts on the SSIM outcomes which

Table 4.3
ANOVA results in regard to Q-Metric

	$\sigma = 5$		$\sigma = 10$		$\sigma = 15$		$\sigma = 20$	
	F-ratio	P-value	F-ratio	P-value	F-ratio	P-value	F-ratio	P-value
A	**16137.11**	0	**10568.16**	0	**10547.72**	0	**13548.82**	0
B	**249.72**	0	247.16	0	211.82	0	228.64	0
C	**1592.93**	0	**2136.77**	0	**2184.63**	0	**2493.38**	0
D	144.17	0	**1413.52**	0	**3188.68**	0	**4630.08**	0
$A \times B$	70.71	0	68.20	0	63.48	0	58.78	0
$A \times C$	**752.16**	0	**746.86**	0	**646.22**	0	**584.84**	0
$A \times D$	**1858.44**	0	**792.43**	0	**763.85**	0	**780.54**	0
$B \times C$	23.21	0	19.41	0	16.52	0	14.63	0
$B \times D$	10.19	0	7.36	0	8.40	0	10.05	0
$C \times D$	**2064.95**	0	**2417.36**	0	**2007.74**	0	**1828.68**	0

A: Decomposition Level, B: Wavelet Base Type, C: Threshold Calculation Method, D: Threshold Type

is targeted maximizing. But when noise levels increases its effect fades out and it is of importance no more. For the first test case seen in Figure A.13 the most maximizing results are parallel with the same results of PSNR of its first case. Hence $J = 1$, SURE and Global produces best result. In the second and third case SURE loses its role and lagged behind GCV. $J = 2$, GCV and Detail are chosen for the best again as in PSNR cases. In the last case threshold type loses its effectiveness but interaction between method and type retains its presence. As a final deduction we end up with $J = 2$ and GCV.

Parameters and their values are endorsed based on the ANOVA results for all image metrics such as PSNR, HMD, Q-Metric and SSIM, which are summarized in Table 4.5. To set the 2D-DWT denoising procedure in such away that yields an acceptable solutions in all metrics, a manner of working can be derived from Table 4.5. In case there is no contradiction among the recommended settings for all criteria, these settings can be put to use. But when there is a contradiction in recommendations, whichever setting appears the most and whichever criterion has more important then the settings for that criterion will be used.

In this study the importance order of four metrics is as Q-Metric, SSIM, HMD and PSNR respectively. For the first test case of $\sigma = 5$, parameters are tuned as $J = 2$, GCV, Global and bior6.8. In the test case of $\sigma = 10, 15$, GCV was chosen by three metrics and for

threshold type, Detail will be applied to due to it appears twice favor maximizing the SSIM and PSNR. Also $J = 2$ is selected for decomposition level. When $\sigma = 20$ $J = 2$,GCV and Detail will be applied.

Table 4.4
ANOVA results in regard to SSIM

	$\sigma = 5$		$\sigma = 10$		$\sigma = 15$		$\sigma = 20$	
	F-ratio	P-value	F-ratio	P-value	F-ratio	P-value	F-ratio	P-value
A	**14127.12**	0	**14101.20**	0	**11483.53**	0	**10704.28**	0
B	22.14	0	27.06	0	28.62	0	25.81	0
C	**7588.42**	0	**8885.91**	0	**8225.24**	0	**6668.33**	0
D	**4684.70**	0	**1805.31**	0	**419.81**	0	19.32	0
$A \times B$	8.29	0	10.59	0	11.95	0	10.30	0
$A \times C$	**1651.61**	0	**2133.61**	0	**2213.47**	0	**1983.63**	0
$A \times D$	**1547.95**	0	**951.96**	0	**504.95**	0	**220.77**	0
$B \times C$	1.69	0.0087	1.89	0.0017	2.23	0.0001	2.68	0
$B \times D$	4.04	0	2.82	0.0001	2.02	0.009	2.59	0.0005
$C \times D$	**1515.21**	0	**1542.26**	0	**1500.53**	0	**1374.56**	0

A: Decomposition Level, B: Wavelet Base Type, C: Threshold Calculation Method, D: Threshold Type

Table 4.5
Summary of Results

Test case	PSNR		HMD	
	Important Factors	Selected Component	Important Factors	Selected Component
$\sigma = 5$	• Dec. Level • Method • Thr. Type	– J=1 – SURE – Global	• Dec. Level • Method • Thr. Type	– J=2 – GCV – Level
$\sigma = 10, 15, 20$	• Dec. Level • Method • Thr. Type	– J=2 – GCV – Detail	• Dec. Level • Method • Thr. Type	– J=2 – GCV – Level

Test case	Q-METRIC		SSIM	
	Important Factors	Selected Component	Important Factors	Selected Component
$\sigma = 5$	• Dec. Level • Method • Wv. Type	– J=2 – GCV – bior6.8	• Dec. Level • Method • Thr. Type	– J=1 – SURE – Global
$\sigma = 10, 15$	• Dec. Level • Method • Thr. Type	– J=2 – Uni-S – Global	• Dec. Level • Method • Thr. Type	– J=2 – GCV – Detail
$\sigma = 20$	• Dec. Level • Method • Thr. Type	– J=3 – Uni-S – Detail	• Dec. Level • Method	– J=2 – GCV

4.2 Application of tuned 2D-DWT on real CLSM Images

To demonstrate the efficacy of the developed 2D-DWT after parameter tuning, it is necessary to compare its performance with different kind of several noisy CLSM images. There are two groups of images that the first group contains images obtained from the database of the Cell Image Library [53–56] and the second group images are from our CLSM setup.

In the first group, as seen in Figure 4.1 we have four different confocal images whose noise levels are estimated as $\sigma_a = 5.41$, $\sigma_b = 11.07$, $\sigma_c = 3.05$ and $\sigma_d = 7.79$ respectively. Furthermore their related Q-metric scores are as $Q_a = 5.67$, $Q_b = 0.50$, $Q_c = 0.12$ and $Q_d = 1.67$.

The first image in Figure 4.1(a) is a portion of dendrite and associated spines from a Purkinje neuron of the brown rat (i.e. Rattus norvegicus) cerebellum [53]. The second is recorded during leaf trichome development stage of a small flowering plant named as thale cress (i.e.Arabidopsis thaliana). Figure 4.1(b) shows the cellular component of actin cytoskeleton [54]. The third image in Figure 4.1(c) is a HeLa cell which the line was derived from cervical epithelium cancer cells taken on 1951. These human cells survive in vitro and named after a cancer patient Henrietta Lacks who died of cancer [55]. The last image seen in Figure 4.1(d) was collected from a fibroblast-like cell line derived from green monkey (i.e. Chlorocebus sabaeus) kidney tissue and it shows the cellular component of endoplasmic reticulum [56].

In the second group, as seen in Figure 4.4 we have four different confocal images obtained from optical setup in Figure 3.3 and alternate with they are chicken skin cell, red blood cell, yeast cell and onion epidermal cells. Their noise levels are estimated as follows $\sigma_a = 9.30$, $\sigma_b = 3.84$, $\sigma_c = 3.20$ and $\sigma_d = 2.26$ respectively. Furthermore their related Q-metric scores are $Q_a = 7.18$, $Q_b = 7.99$, $Q_c = 9.86$ and $Q_d = 2.18$.

As seen in Table 4.6 very good results are obtained by applying tuning parameters suggested from ANOVA results for both noise elimination and improvement in Q-metric.

Table 4.6
Results of noise levels and Q-Metrics of the confocal images before and after denoising application

	Before			After	
	σ	Q		σ	Q
Figure 4.1 Database Images					
Figure 4.1(a)	5.41	5.67		2.08	9.94
Figure 4.1(b)	11.07	0.50		0.67	3.13
Figure 4.1(c)	3.05	0.12		0.10	1.12
Figure 4.1(d)	7.79	1.67		0.16	4.91
Figure 4.4 Setup Images					
Figure 4.4(a)	9.30	7.18		3.74	17.60
Figure 4.4(b)	3.84	7.99		0.23	19.00
Figure 4.4(c)	3.20	9.86		0.34	18.90
Figure 4.4(d)	2.26	2.18		0.27	13.70

4.3 Comparison of Contrast Enhancement Methods Applied on Denoised CLSM Images

In this section five different histogram equalization techniques were implemented to eight denoised CLSM images seen in Figures 4.2(a), 4.2(c), 4.3(a), 4.3(c), 4.5(a), 4.5(c), 4.6(a) and 4.6(c) to evaluate their performance. The performance is assessed on the basis of contrast improvement ratio (CIR), the measure of enhancement (EME), absolute mean brightness error (AMBE) and the entropy. For no-reference metrics, i.e. EME and entropy, the percentage improvement is calculated using Eq. 4.1-4.2 for ease of comparison.

$$\text{Entropy}(\%) = \frac{\text{Entropy of Output Image}}{\text{Entropy of Input Image}} \times 100 \tag{4.1}$$

$$\text{EME}(\%) = \frac{\text{EME of Output Image}}{\text{EME of Input Image}} \times 100 \tag{4.2}$$

Using these measurements, five algorithms HE, CLAHE, BBHE, MMBEBHE and BHEPL are performed on eight CLSM images. Table 4.7 shows the mean and One-way ANOVA result of CIR, EME(%), AMBE and Entropy(%) for eight images. respectively. Figures 4.7 and 4.8 shows the boxplot representation of the outcomes of metrics. On each box, the

Table 4.7
Results of different performance metrics of the confocal images after contrast enhancement

	Mean of Performance Measures			
	CIR	EME(%)	AMBE	ENTROPY(%)
Methods				
HE	5.14	399.3	59.58	97.59
CLAHE	1.07	169.9	18.17	**109.87**
BBHE	**7.31**	**560.3**	17.32	97.87
MMBEBHE	6.73	539.8	7.88	97.06
BHEPL	3.31	438.7	**6.92**	99.38
One-way ANOVA				
F-ratio	9.39	2.83	20.26	76.04
P-value	0	0.0389	0	0

central red mark is the median and the edges of the box are the 25th and 75th percentiles (i.e. 1st and 3rd quantiles). The whiskers extend to the most extreme data points that are not considered outliers. The outliers are plotted individually by red '+' signs. Two medians are significantly different at the 5 significance level if their intervals do not overlap. This test is different from the F-test that ANOVA performs, but large differences in the center lines of the boxes correspond to large F-statistic values and correspondingly small p-values.

Starting with ANOVA results of CIR we can conclude that F-ratio=9.39 (p-value<0.05) indicates that the mean responses of CIR values is not the same. BBHE yields the best result for CIR among all methods and the median CIR value for BBHE is significantly different from only two methods including CLAHE and BHEPL. But the differences in CIR values among BBHE, HE and MMBEBHE are not.

For EME(%) results, BBHE comes out of other methods again but this time with a less F-ratio equal to 2.83 and we can conclude that mean responses are different. But as inspecting boxplot representation one can say that the median value of EME(%) for BBHE is only significantly different from the method CLAHE and others not.

In AMBE metrics we desire a method to have minimum value of AMBE (i.e. minimization problem) and BHEPL did well with an F-ratio=20.26 indicating mean AMBE

values are not the same. Only the method HE is significantly different from BHEPL but we cannot reject the hypothesis that other group means including BHEPL are different from each other.

In the last part, CLAHE has an outperforming result of Entropy(%). ANOVA rejects the null hypothesis that the mean entropy(%) values from all five methods are equal to each other. The other group means excluding CLAHE are not significantly different from each other.

To sum up, CLAHE is a good method for image entropy and also performs well for brightness preservation but it lags in the manner of contrast improvement. One possible reason is that the clip-limit should be adjusted carefully and for our case we have selected it as 0.01. An automatic contrast limiting algorithm is needed. BHEPL is the second candidate in entropy measurement and did the best in brightness preservation (i.e. AMBE). It also has a reasonable performance for contrast enhancement in the manner of both CIR and EME(%). The last candidate of best method is BBHE. On the contrary CLAHE, it shows better performance in contrast improvement by showing the best result in CIR. MMBEBHE exhibited no noteworthy results from other methods in experimental results. We can see that HE shows a good performance in contrast improvement by looking at CIR and EME(%). But HE is the worst on preserving mean brightness and it is obvious that it over-enhances images. Figures 4.9 and 4.10 show enhancement results of denoised CLSM images based on CLAHE, BHEPL and BBHE.

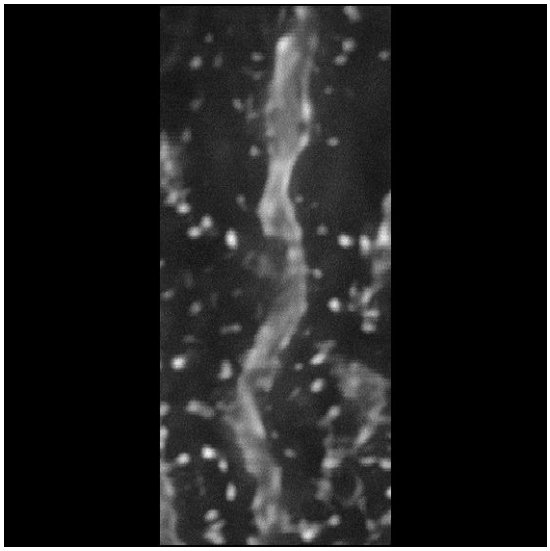

(a) Rattus Norvegicus - CNS Neuron/Purkinje cell [53]. Pixel Size:555×231, $\sigma_a = 5.41$ and $Q_a = 5.67$

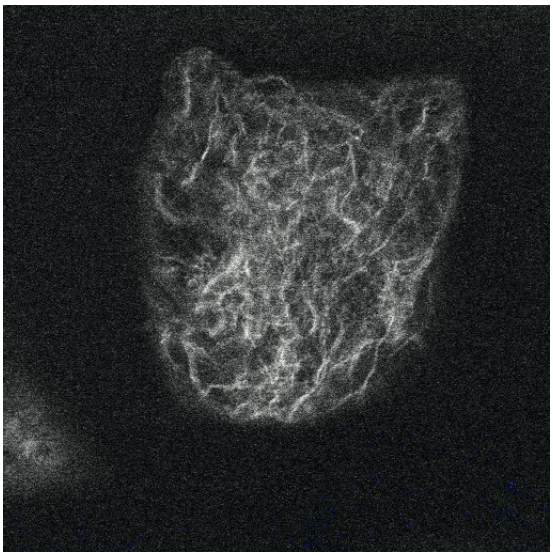

(b) Arabidopsis Thaliana - Actin cytoskeleton [54]. Pixel Size:512×512, $\sigma_b = 11.07$ and $Q_b = 0.50$

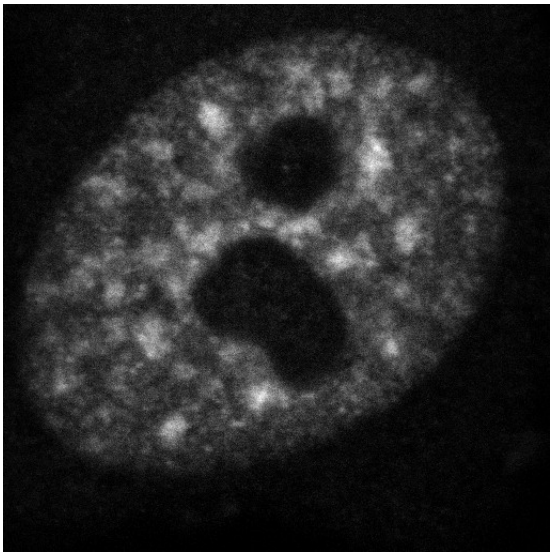

(c) Homo Sapiens - Cervical epithelium [55]. Pixel Size:512×512, $\sigma_c = 3.05$ and $Q_c = 0.12$

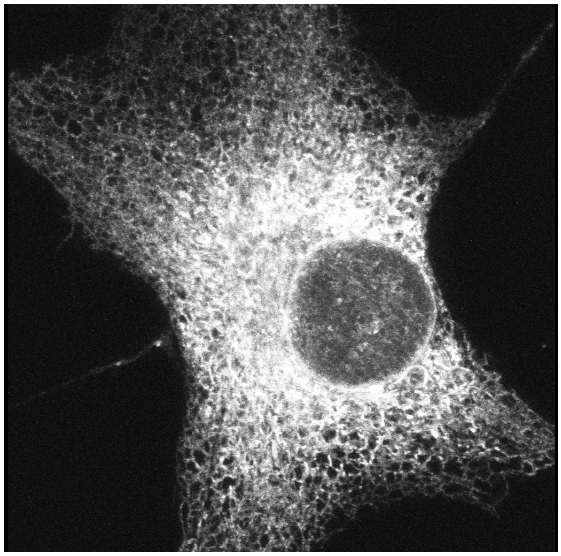

(d) Chlorocebus Sabaeus - COS7/ER [56]. Pixel Size:1024×1037, $\sigma_d = 7.79$ and $Q_d = 1.67$

Figure 4.1 Confocal Microscopy Images from Cell Image Library (First Group)

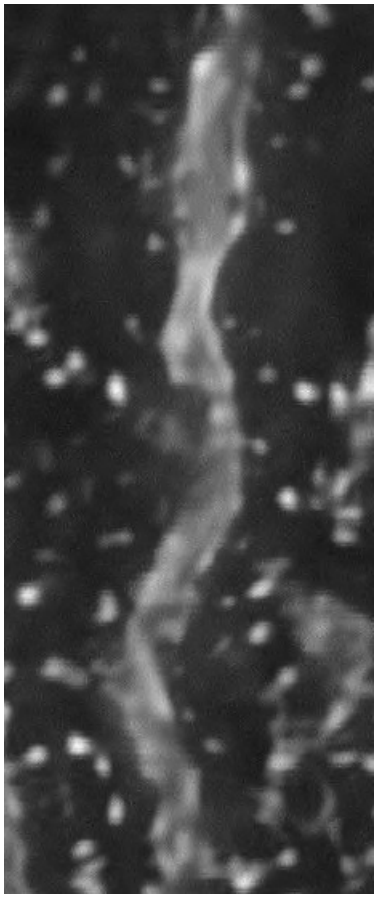

(a) Denoised Image with $\hat{\sigma}_a = 2.08$ and $\hat{Q}_a = 9.94$

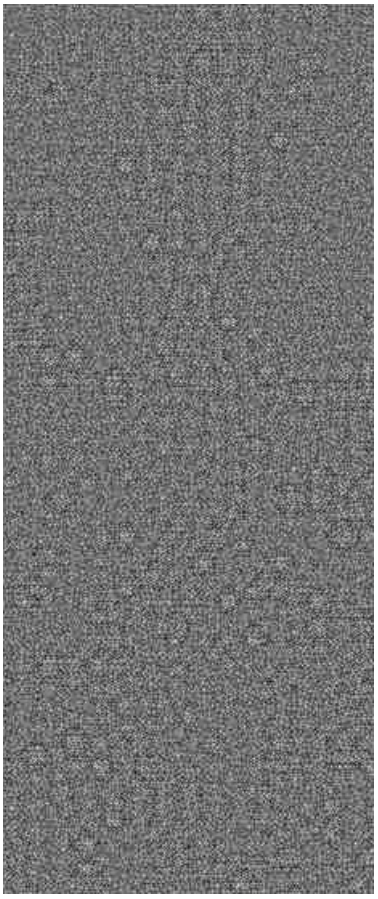

(b) Extracted noise

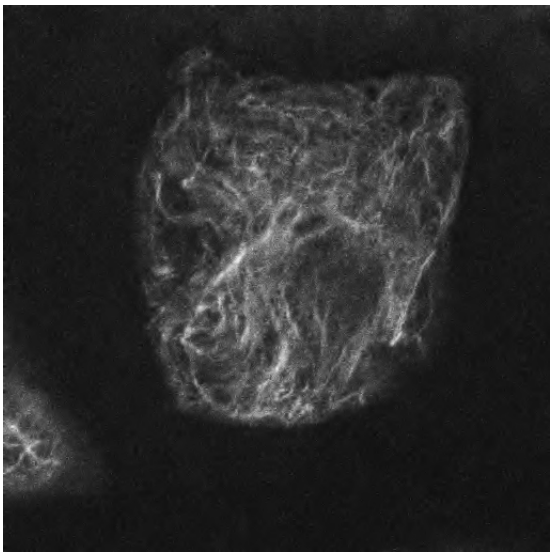

(c) Denoised Image with $\hat{\sigma}_b = 0.67$ and $\hat{Q}_b = 3.13$

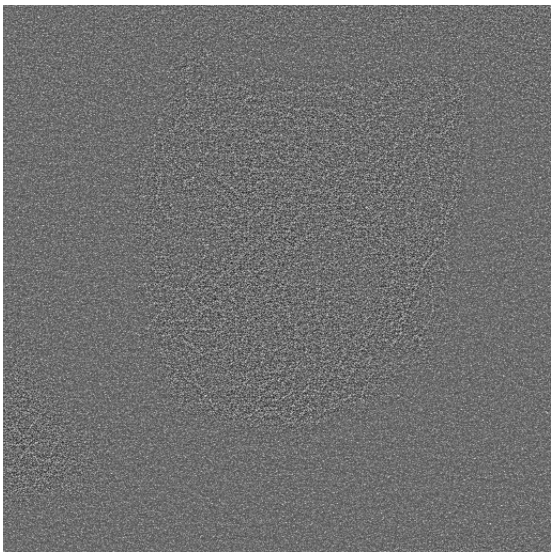

(d) Extracted noise

Figure 4.2 Denoised images in Figures 4.1(a) and 4.1(b) generated by using tuning parameters from ANOVA results

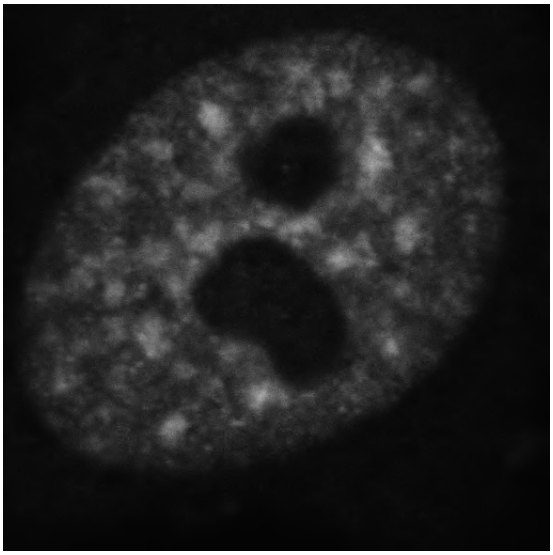

(a) Denoised Image with $\hat{\sigma}_c = 0.10$ and $\hat{Q}_c = 1.12$

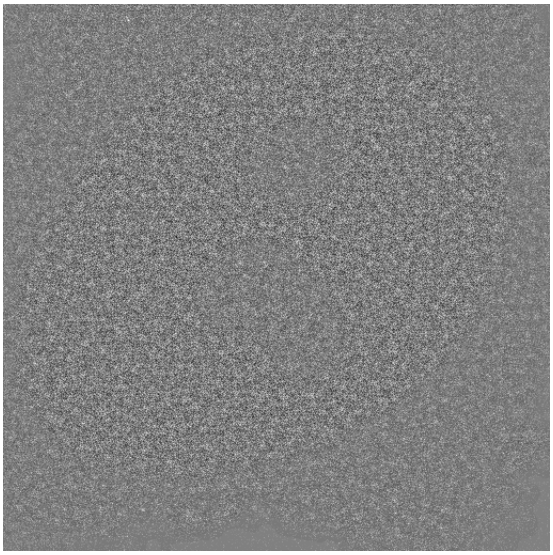

(b) Extracted noise

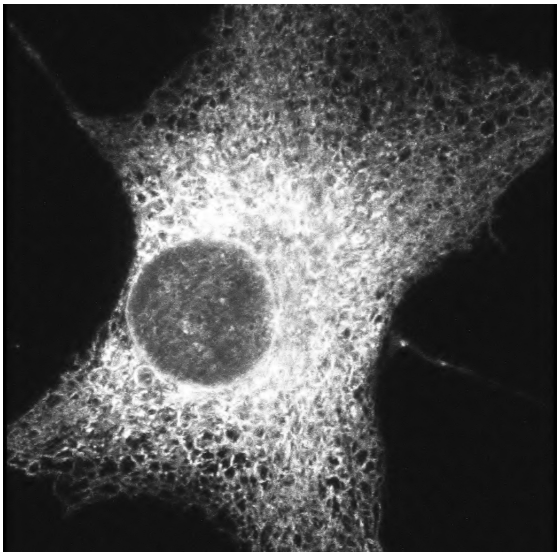

(c) Denoised Image with $\hat{\sigma}_d = 0.16$ and $\hat{Q}_d = 4.91$

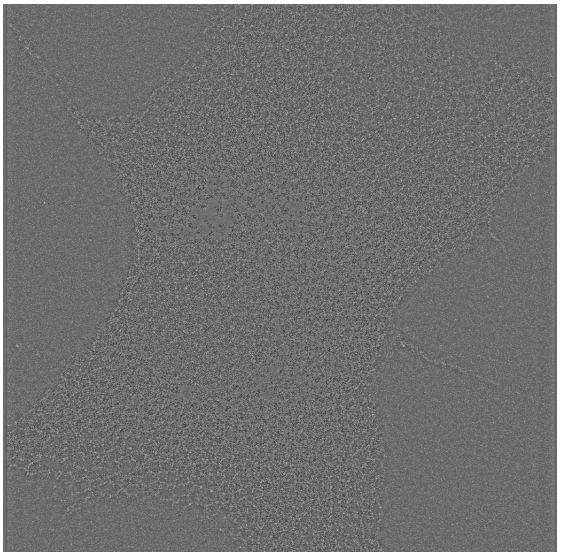

(d) Extracted noise

Figure 4.3 Denoised images in Figures 4.1(c) and 4.1(d) generated by using tuning parameters from ANOVA results

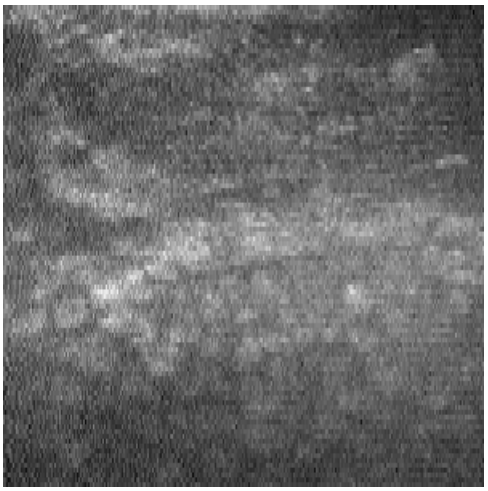

(a) Chicken Skin Cells. Pixel Size:300×300, $\sigma_a = 9.30$ and $Q_a = 7.18$

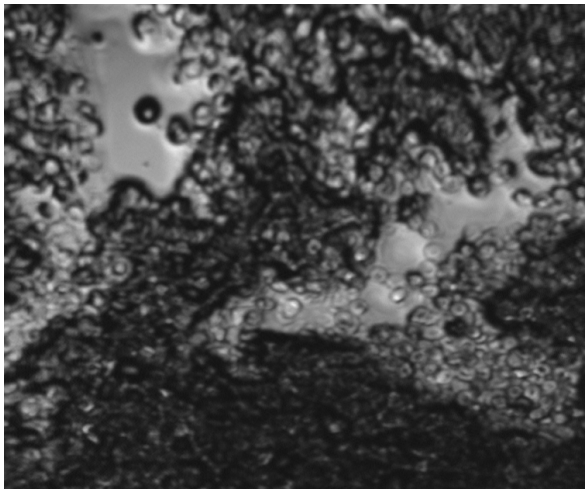

(b) Red Blood Cells. Pixel Size:625×750, $\sigma_b = 3.84$ and $Q_b = 7.99$

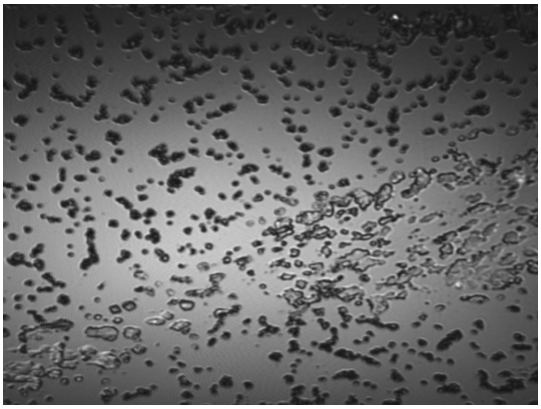

(c) Yeast Cells. Pixel Size:750×1000, $\sigma_c = 3.20$ and $Q_c = 9.86$

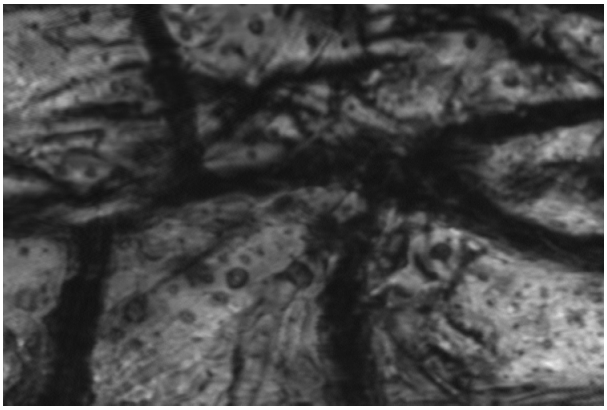

(d) Onion Epidermal Cells. Pixel Size:500×750, $\sigma_d = 2.26$ and $Q_d = 2.18$

Figure 4.4 Confocal Microscopy Images obtained from Optical Setup (Second Group)

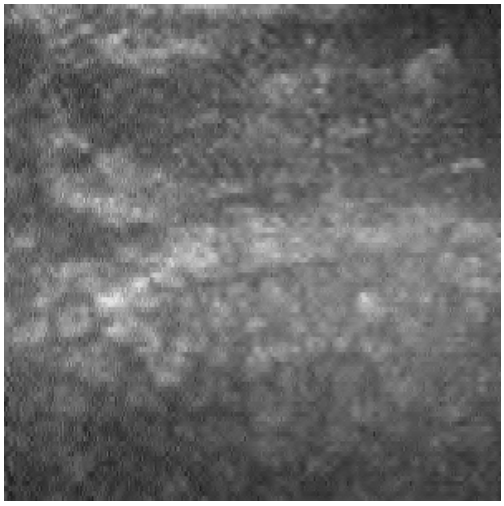

(a) Denoised Image with $\hat{\sigma}_a = 3.74$ and $\hat{Q}_a = 17.60$

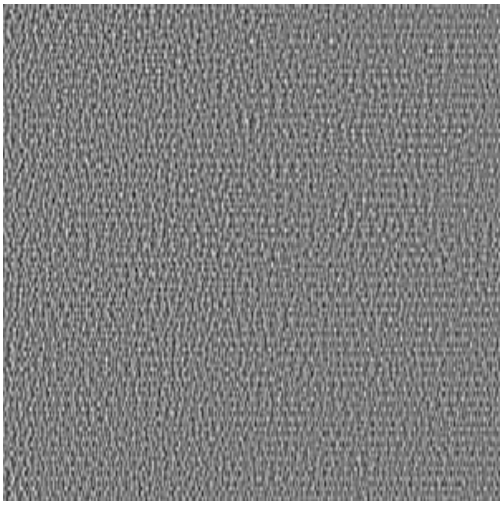

(b) Extracted noise

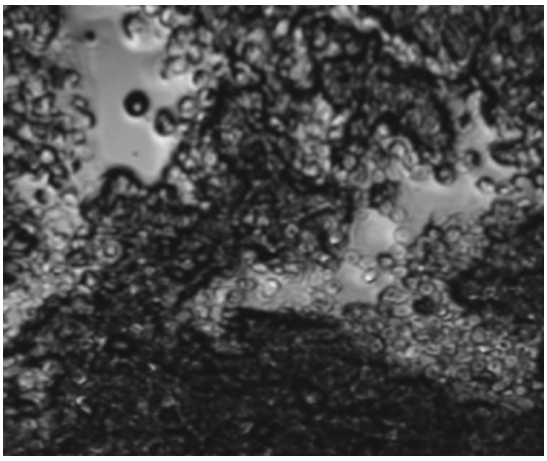

(c) Denoised Image with $\hat{\sigma}_b = 0.23$ and $\hat{Q}_b = 19.00$

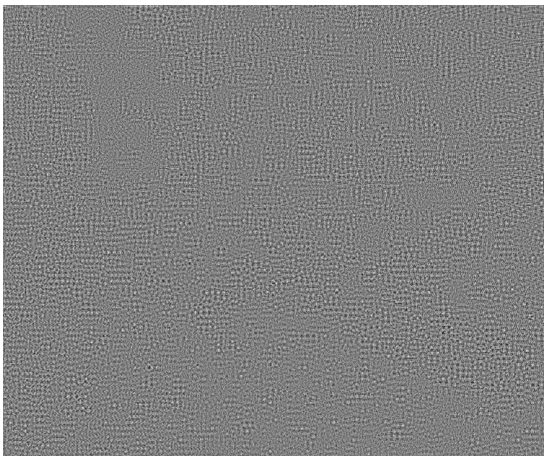

(d) Extracted noise

Figure 4.5 Denoised images in Figures 4.4(a) and 4.4(b) generated by using tuning parameters from ANOVA results

(a) Denoised Image with $\hat{\sigma}_c = 0.34$ and $\hat{Q}_c = 18.90$

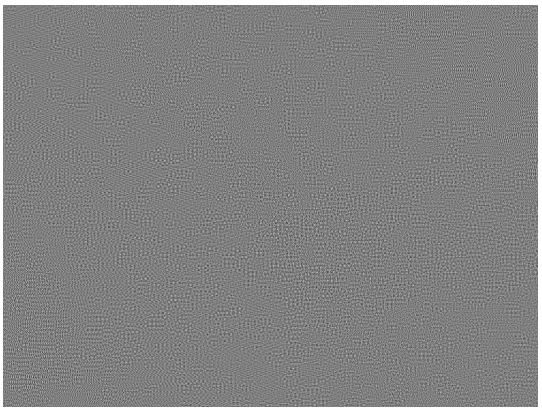

(b) Extracted noise

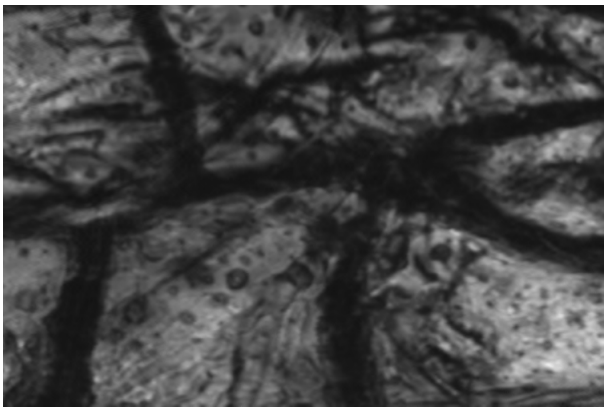

(c) Denoised Image with $\hat{\sigma}_d = 0.27$ and $\hat{Q}_d = 13.70$

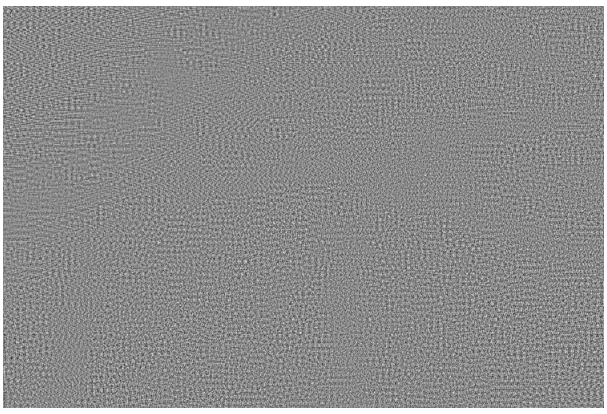

(d) Extracted noise

Figure 4.6 Denoised images in Figures 4.4(c) and 4.4(d) generated by using tuning parameters from ANOVA results

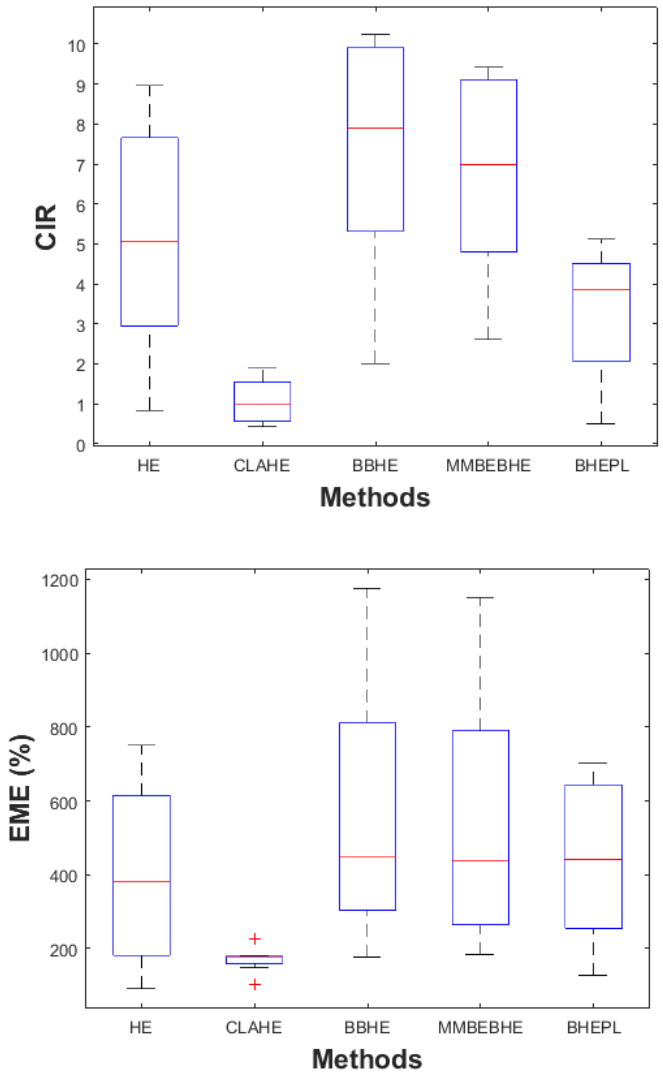

Figure 4.7 One-way ANOVA boxplot representation of performance measures CIR and EME(%)

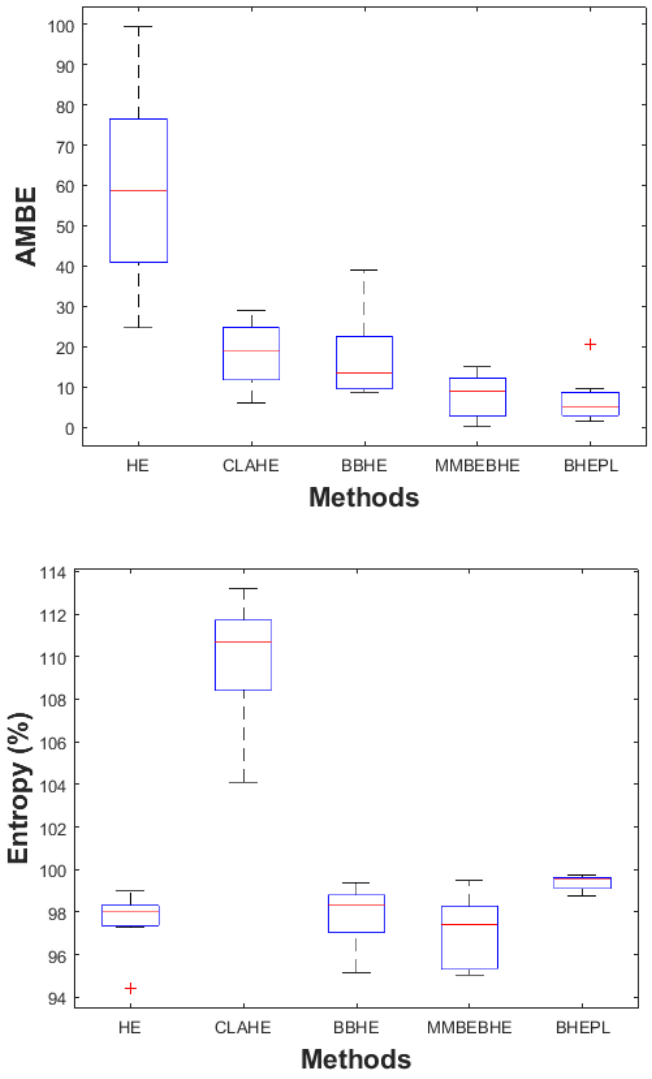

Figure 4.8 One-way ANOVA boxplot representation of performance measures AMBE and Entropy(%)

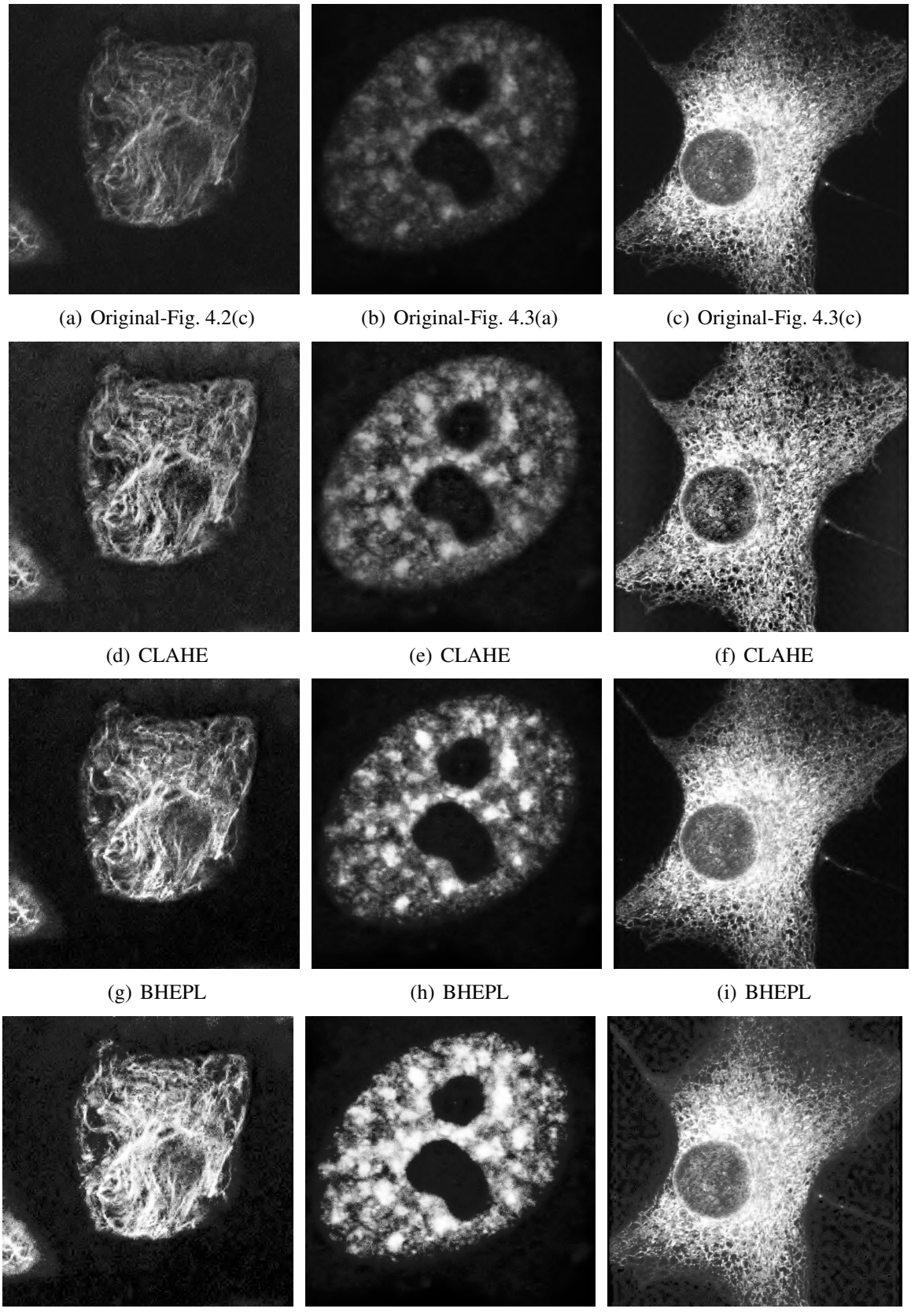

(a) Original-Fig. 4.2(c) (b) Original-Fig. 4.3(a) (c) Original-Fig. 4.3(c)

(d) CLAHE (e) CLAHE (f) CLAHE

(g) BHEPL (h) BHEPL (i) BHEPL

(j) BBHE (k) BBHE (l) BBHE

Figure 4.9 Contrast enhancement after denoising (First Group)

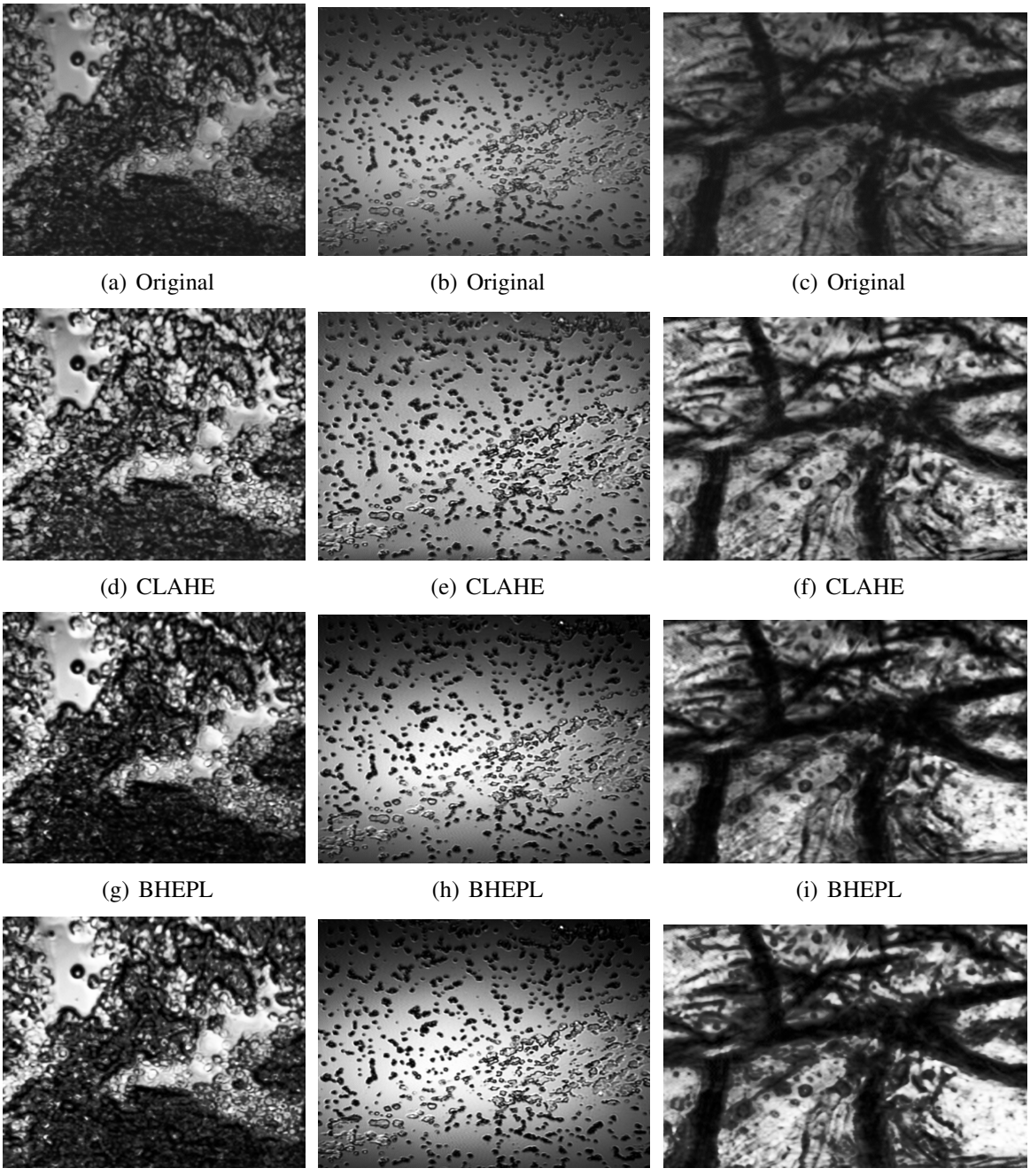

(a) Original (b) Original (c) Original

(d) CLAHE (e) CLAHE (f) CLAHE

(g) BHEPL (h) BHEPL (i) BHEPL

(j) BBHE (k) BBHE (l) BBHE

Figure 4.10 Contrast enhancement after 2D-DWT denoising (Second Group)

5. CONCLUSION and FUTURE WORKS

The CLSM system was described here has been built that has a positioning and dual-axis scanning mechanism. Our system demonstrates acceptable resolution and strength to obtain confocal images from specimens in real-time. The approach has been driven by the requirement that the collected image need a restoration process due to noise and contrast irregularities caused by various factors such as out-of-focus light, pinhole size, and PMT detector. In order to recover CLSM images, various methods and algorithms were implemented on real collected confocal images. The denoising operation is to take a noisy image and then to estimate clean image. The noise level in an image is a useful indicator to realize the performance of the denoising applications. Therefore, some proposed techniques are investigated to estimate noise level in a single image. The procedure proposed by [15] gave better results on both Lena and a real confocal image.

Due to better spatial and spectral representation of image formation and providing energy conservation during transformation, 2D-DWT is useful for image filtering. For that purpose, several thresholding methods proposed in the literature are evaluated on real CLSM images corrupted with AWGN. The performance of denoising methods is measured by using one no-reference, i.e. Q-Metric and three full-reference quality assessment metrics including HMD,SSIM and a more traditional approach such as PSNR. Since 2D-DWT based image denoising methods are complex, they demand for a good parametrization. There also seems lack of a systematic approach in the literature for tuning parameters of image wavelet denoising. A systematic study based on the design of experiments in tuning the denoising algorithm to the highest performance, which is defined by four different metrics. Comprehensive experiments are performed by using a real CLSM image and convincing results are obtained.

Decomposition level of 2D-DWT is the most important factor and with an increase in noise level it requires further levels for thresholding and effectively cleaning noise from input image. The number of two level decomposition ($J = 2$) seems to be sufficient. The second

one is the threshold calculation method. Based on experiments we can conclude that GCV, SURE and Universal-Soft are respectively the most effective candidates among the methods considered. The last important factor is the threshold type and it is observed that in the low levels of noise Global is more influential but along with the noise level the threshold type, Detail, supercedes Global. HMD results are the only exception that Level is slightly better. Wavelet base types played no main role in image denoising but once the Q-metric result indicated that bior6.8 is an attractive choice of wavelet base and significantly improves the results. As a result it was instructive to compare the performance of these parameters on real CLSM images following the criterion of their efficiency in different ways. The developed 2D-DWT method is applicable to real noisy CLSM images both in favor of noise suppression and image quality improvement. A potential application of the 2D-DWT based denoising includes a real time, adaptive and automatic parameter selection. Advanced wavelet denoising methods for mixed Gaussian-Poissonian noise should also be implemented under different evaluation metrics in the future.

As a second part of this thesis, contrast enhancement experiments on denoised CLSM images has been attempted. The objective comparison was made using two no-reference, i.e. EME and entropy, and two full-reference quality assessment metrics such as CIR and AMBE. In Table 4.7, p-values less than 0.05 indicate that all mean results for various methods are different from each other. Experimental results show that CLAHE with parameters, clip-limit=0.01 and the number of blocks=8×8, can enhance the real CLSM images with a better improvement in image details at the same time preserving the input brightness. In future CLAHE can be extended to an automatically parameter selecting algorithm and it can be implemented with different histogram shapes such as Rayleigh histogram. Additionally BHEPL did well on brightness preservation, contrast improvement and entropy measurement. Lastly BBHE provides better contrast improvement but its entropy is not as much as CLAHE and BHEPL.

In conclusion, we have presented an analytical method to determine the best methods for both image denoising and contrast enhancement. Restored CLSM images become visually more appealing. The validity of our approach in the field of CLSM was first verified by ANOVA results and then in the application of real CLSM images followed by measuring dif-

ferent image quality assessments. It should also be noted that while the microscopy system described here will be useful in an assortment of in vitro and in vivo applications and with the help of the image processing and computer-aided diagnosis, a full-featured commercial system can be created at a fraction of the cost.

5.1 List of publications produced from the thesis

1. Implementation of high-performance LSM using wavelet transformation analysis, F. Sansal, Y. E. Gokdag, H. Kizilcabel and Y. D. Gokdel *23nd Signal Processing and Communications Applications Conference (SIU)*, pp. 1321-1324, May. 3, 2015.

APPENDIX A. Complete ANOVA Analysis Figures

A.1 ANOVA Mean Plots of PSNR Results

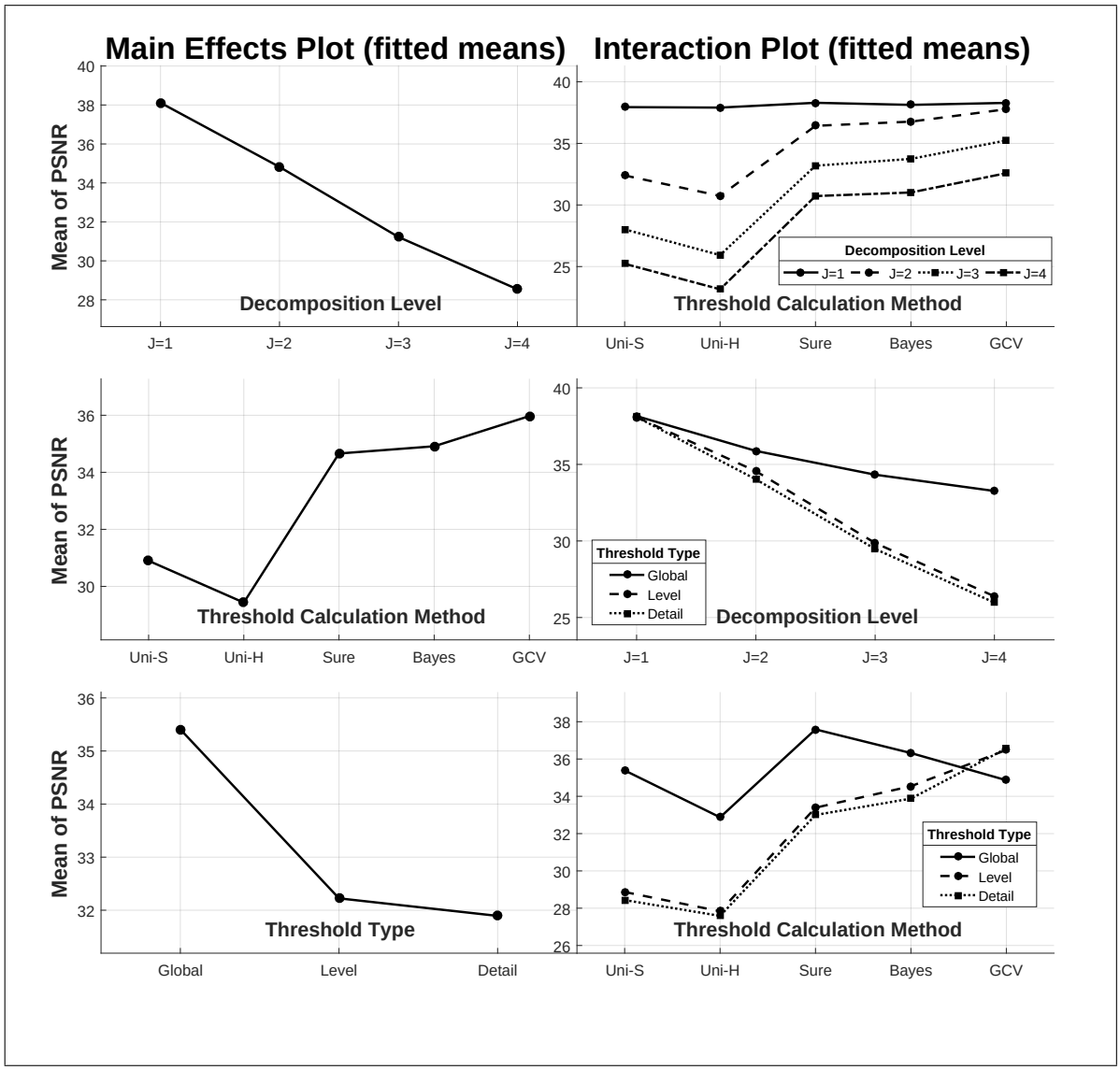

Figure A.1 PSNR: Different level averages of effective factors (left) and interactions (right) for decomposition level, threshold calculation method and threshold type for the **first** test case $\sigma = 5$

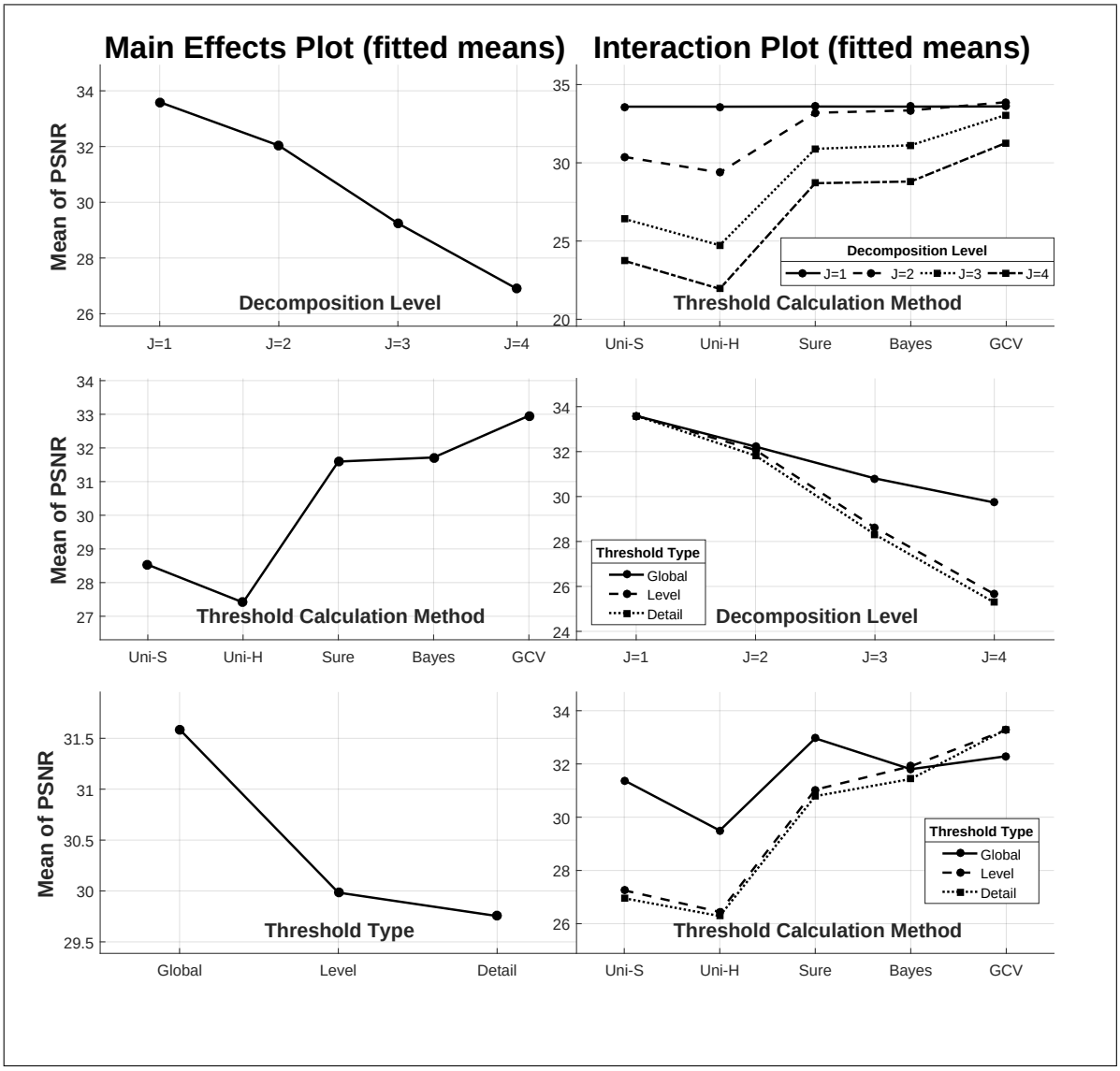

Figure A.2 PSNR: Different level averages of effective factors (left) and interactions (right) for decomposition level, threshold calculation method and threshold type for the **second** test case $\sigma = 10$

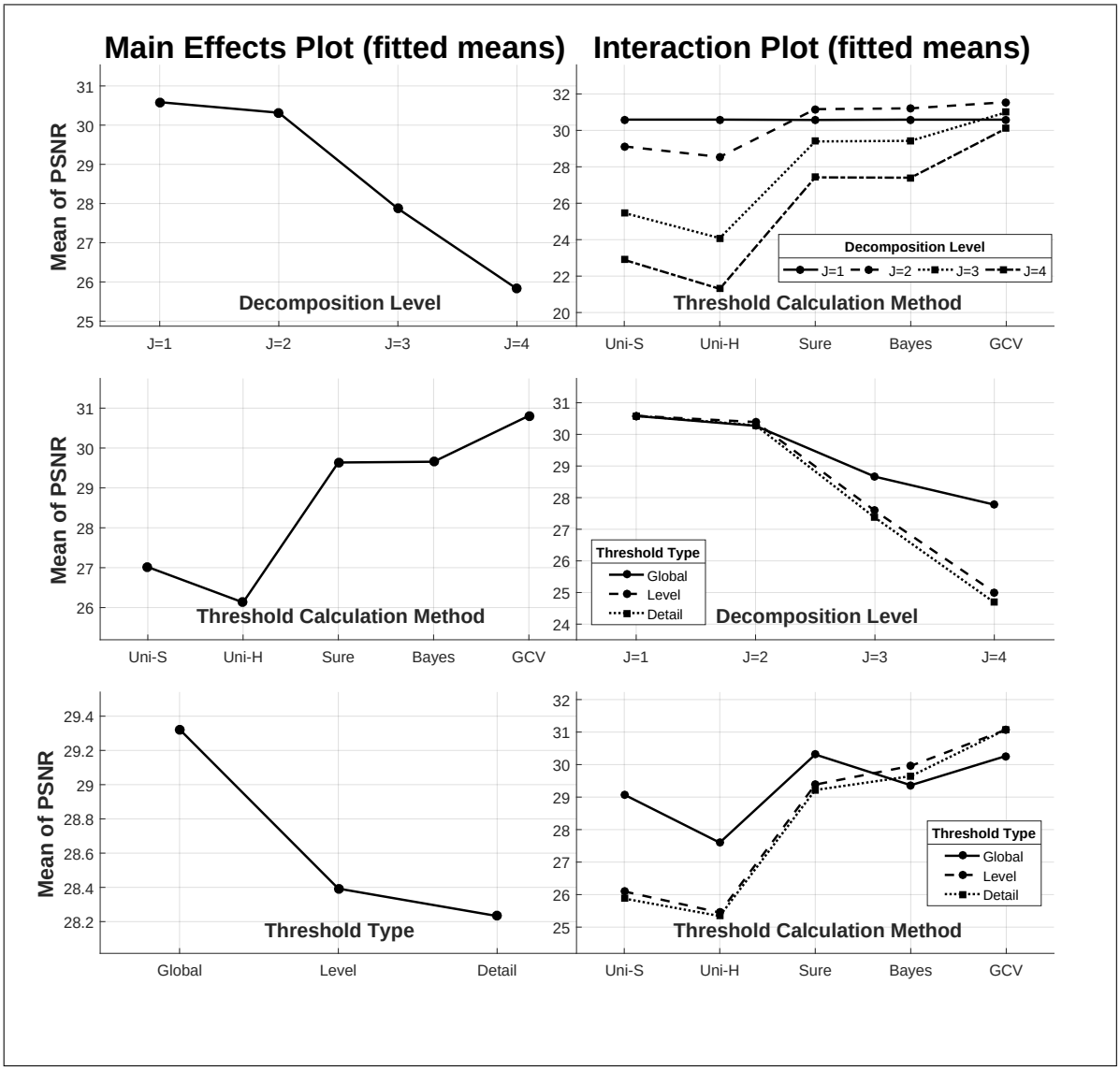

Figure A.3 PSNR: Different level averages of effective factors (left) and interactions (right) for decomposition level, threshold calculation method and threshold type for the **third** test case $\sigma = 15$

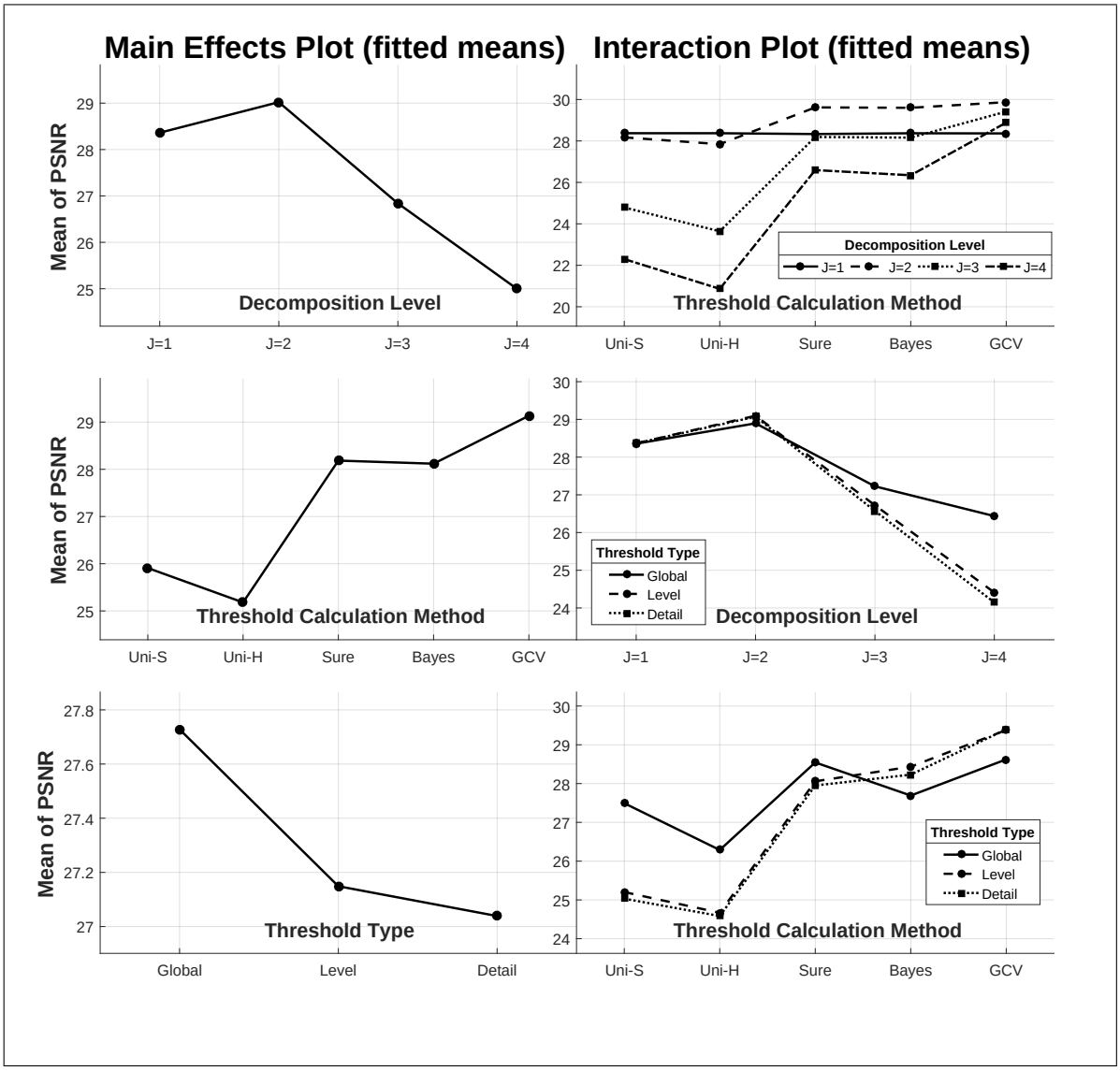

Figure A.4 PSNR: Different level averages of effective factors (left) and interactions (right) for decomposition level, threshold calculation method and threshold type for the **fourth** test case $\sigma = 20$

A.2 ANOVA Mean Plots of HMD Results

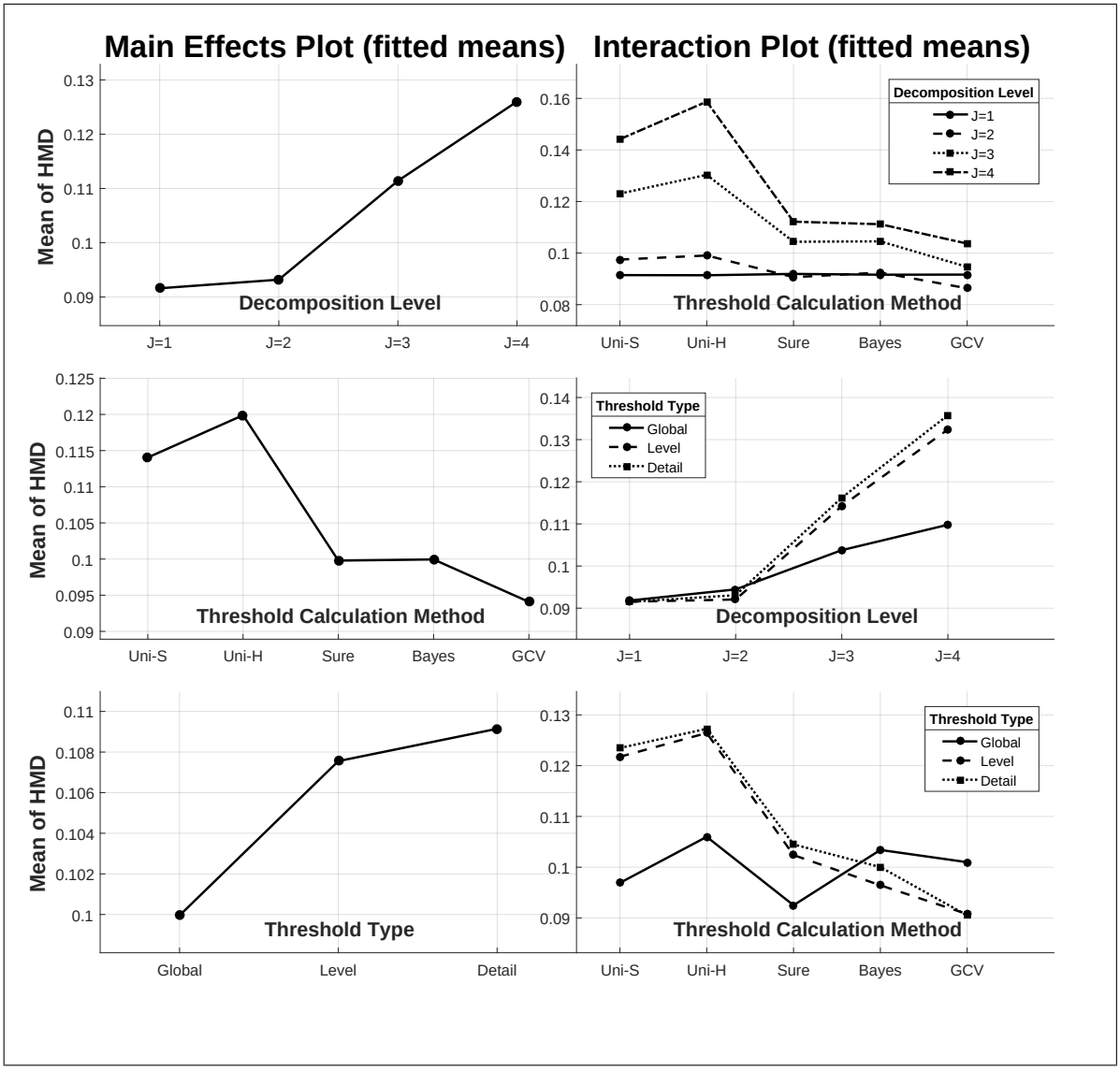

Figure A.5 HMD: Different level averages of effective factors (left) and interactions (right) for decomposition level, threshold calculation method and threshold type for the **first** test case $\sigma = 5$

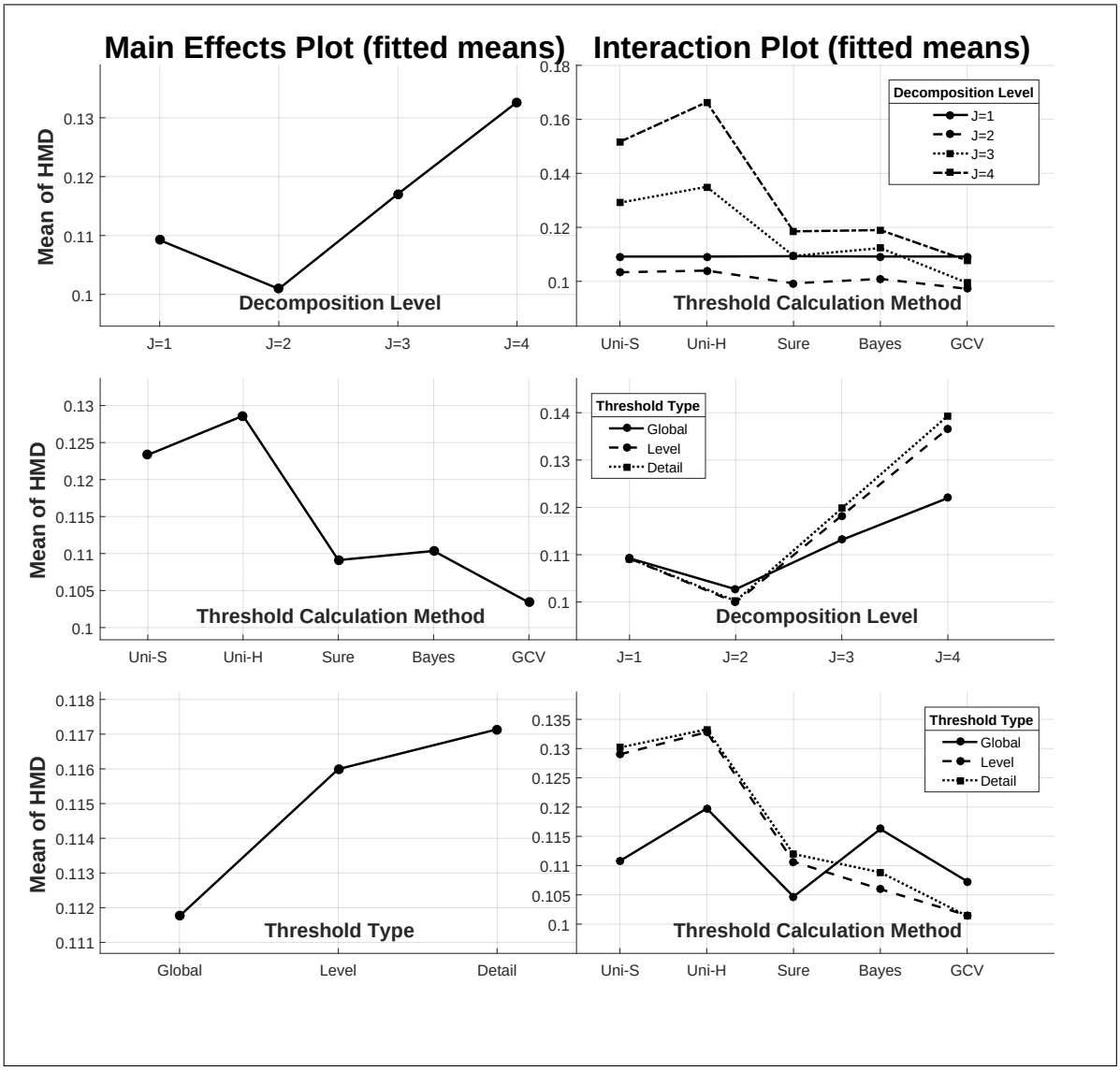

Figure A.6 HMD: Different level averages of effective factors (left) and interactions (right) for decomposition level, threshold calculation method and threshold type for the **second** test case $\sigma = 10$

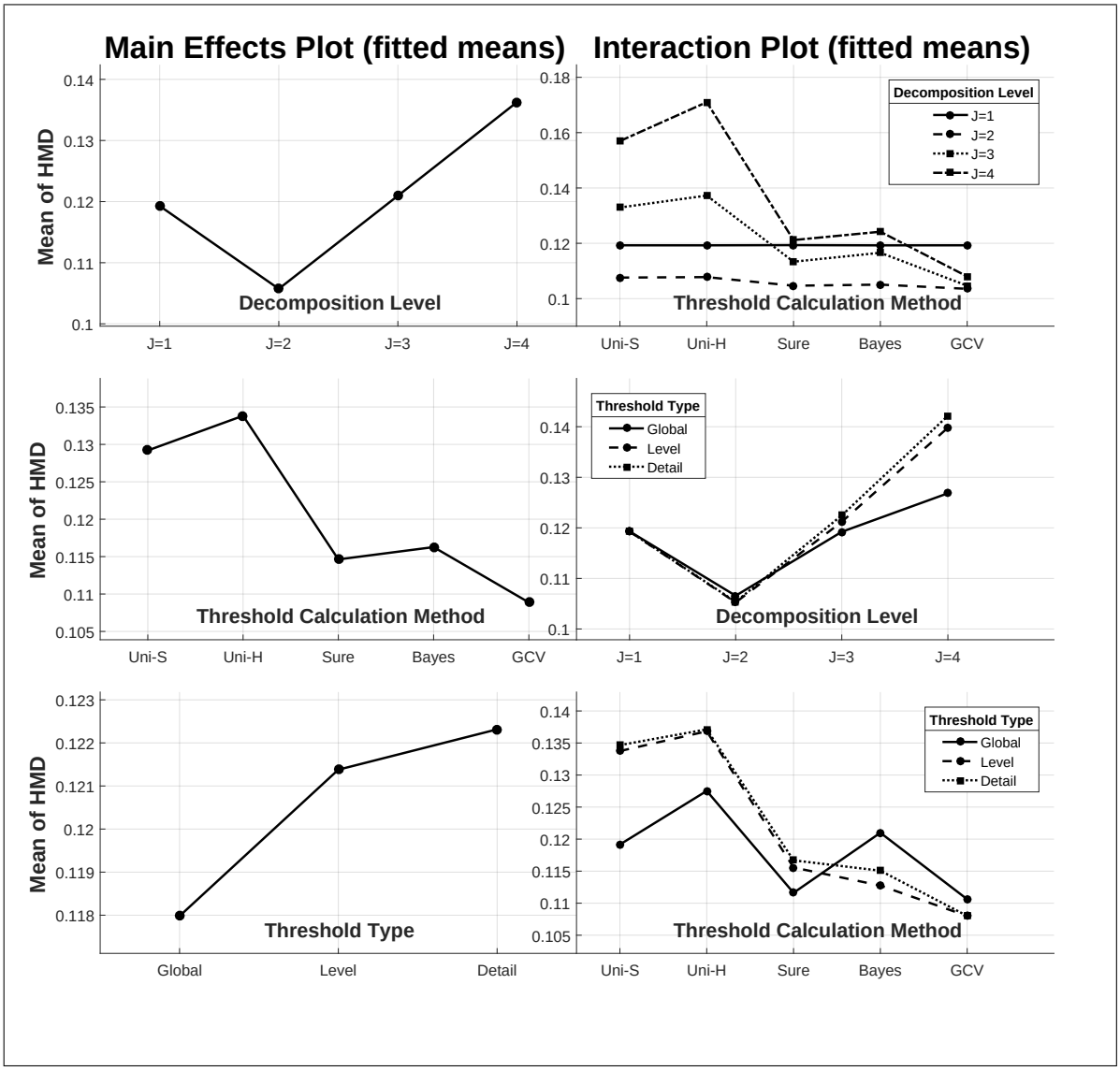

Figure A.7 HMD: Different level averages of effective factors (left) and interactions (right) for decomposition level, threshold calculation method and threshold type for the **third** test case $\sigma = 15$

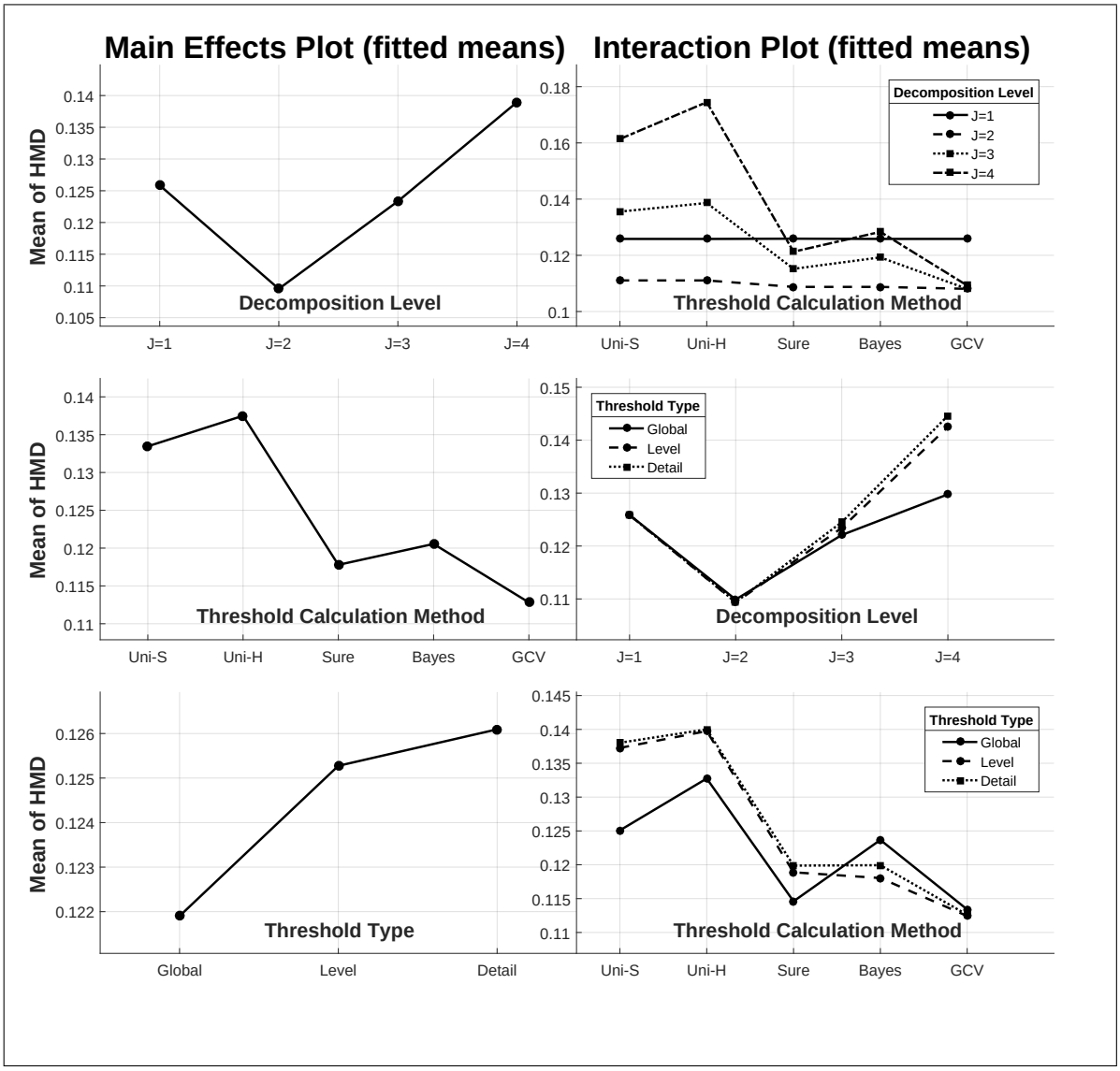

Figure A.8 HMD: Different level averages of effective factors (left) and interactions (right) for decomposition level, threshold calculation method and threshold type for the **fourth** test case $\sigma = 20$

A.3 ANOVA Mean Plots of Q-Metric Results

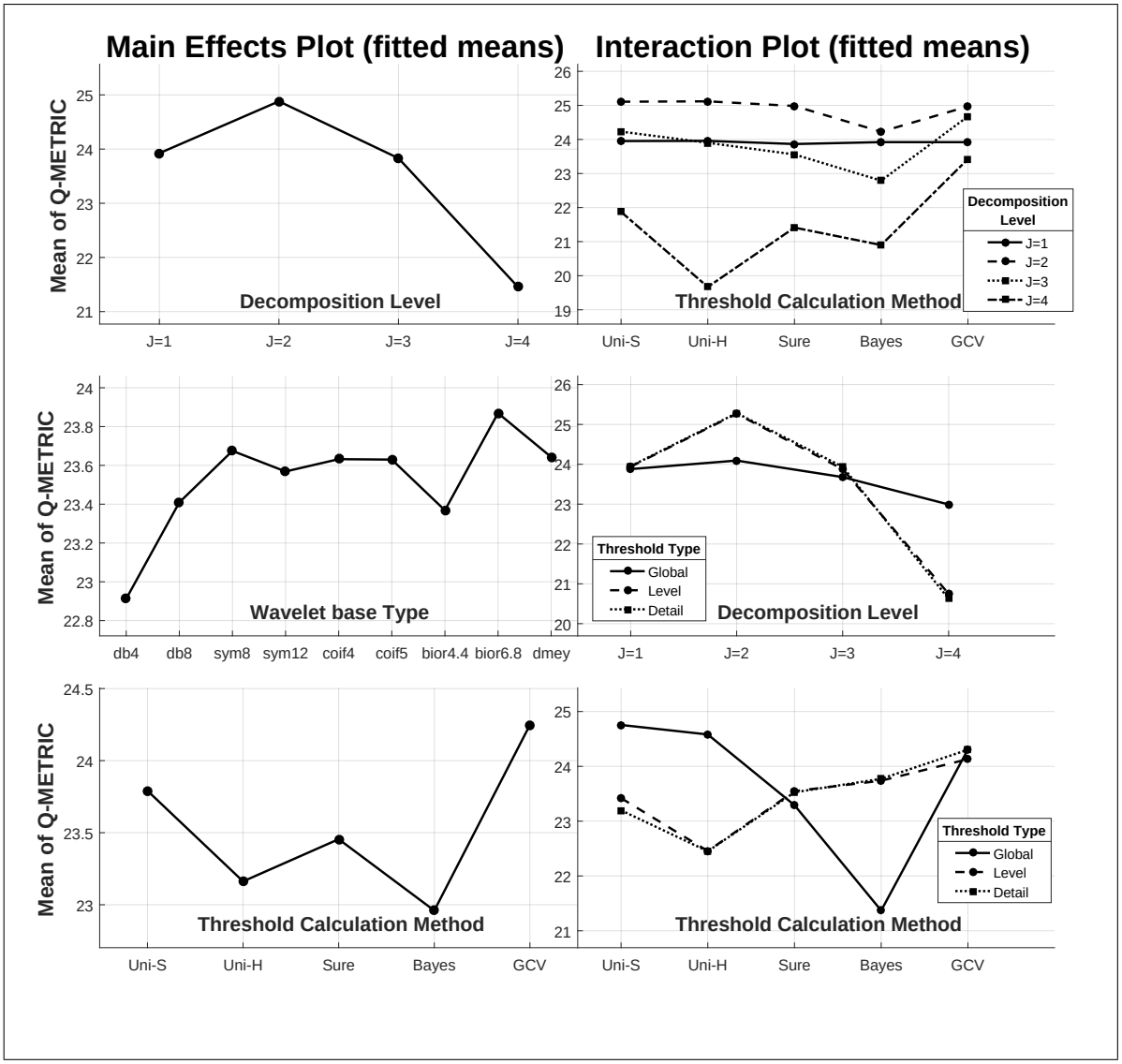

Figure A.9 Q-METRIC: Different level averages of effective factors (left) and interactions (right) for decomposition level, threshold calculation method and threshold type for the **first** test case $\sigma = 5$

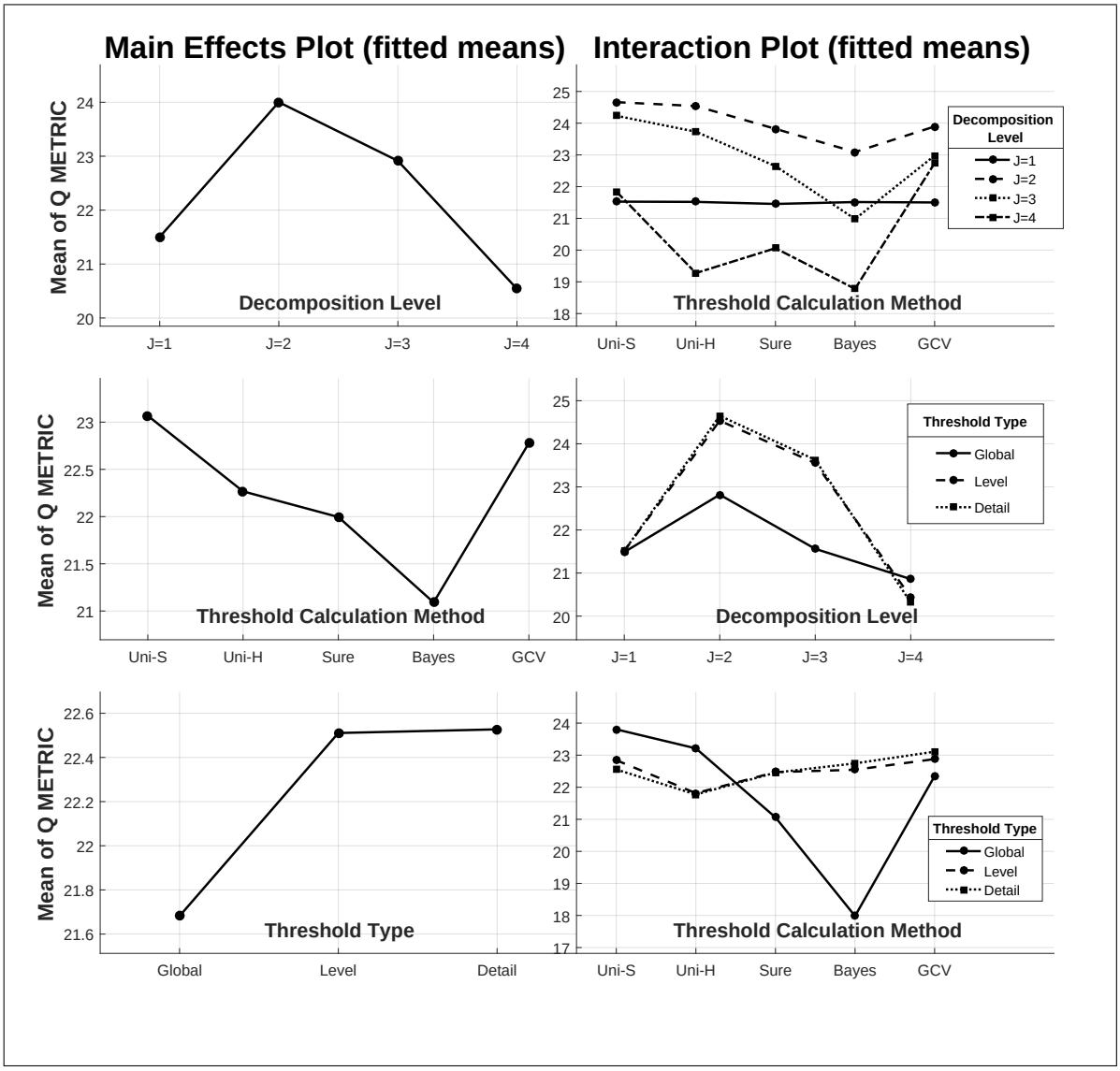

Figure A.10 Q-METRIC: Different level averages of effective factors (left) and interactions (right) for decomposition level, threshold calculation method and threshold type for the **second** test case $\sigma = 10$

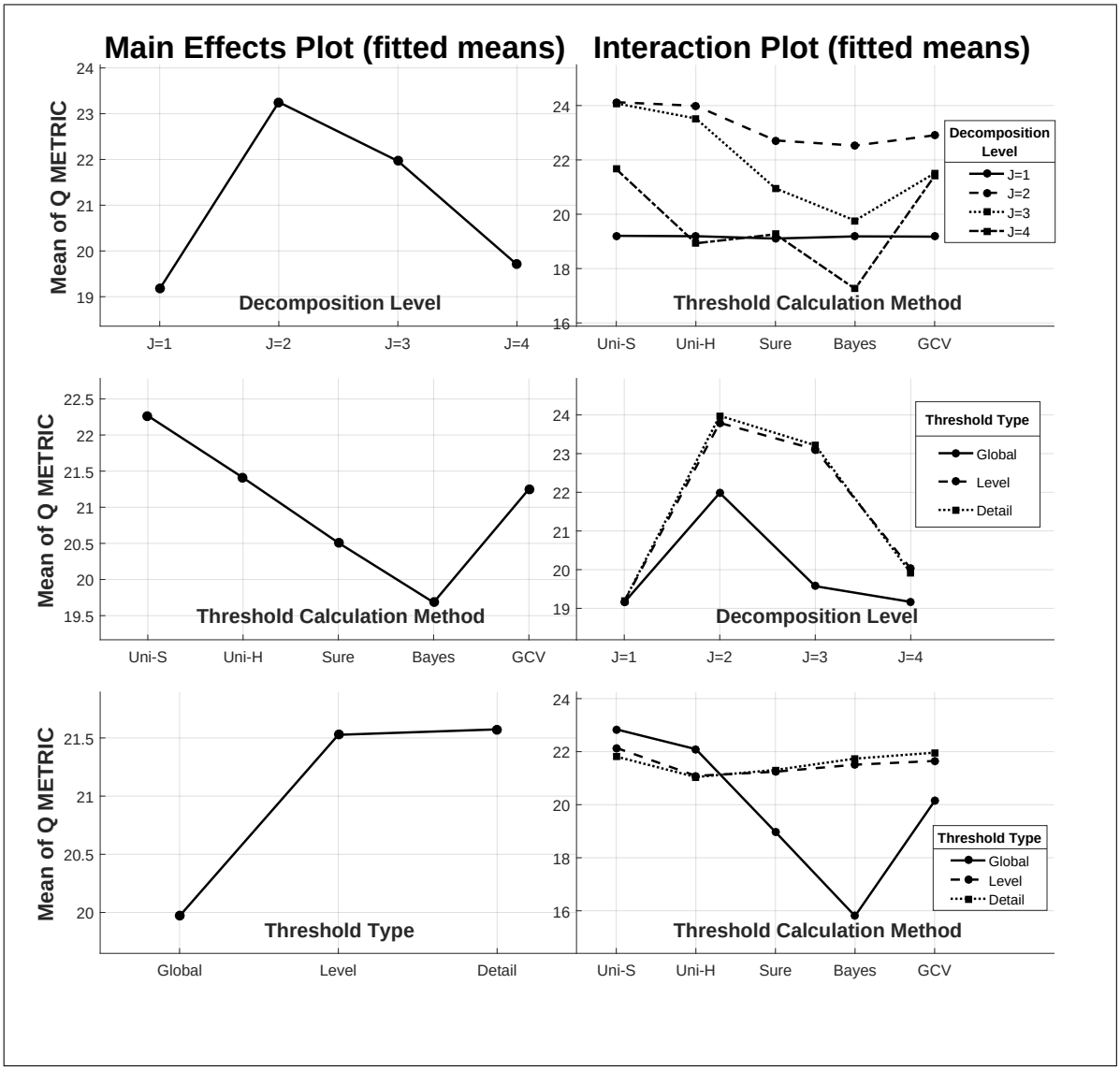

Figure A.11 Q-METRIC: Different level averages of effective factors (left) and interactions (right) for decomposition level, threshold calculation method and threshold type for the **third** test case $\sigma = 15$

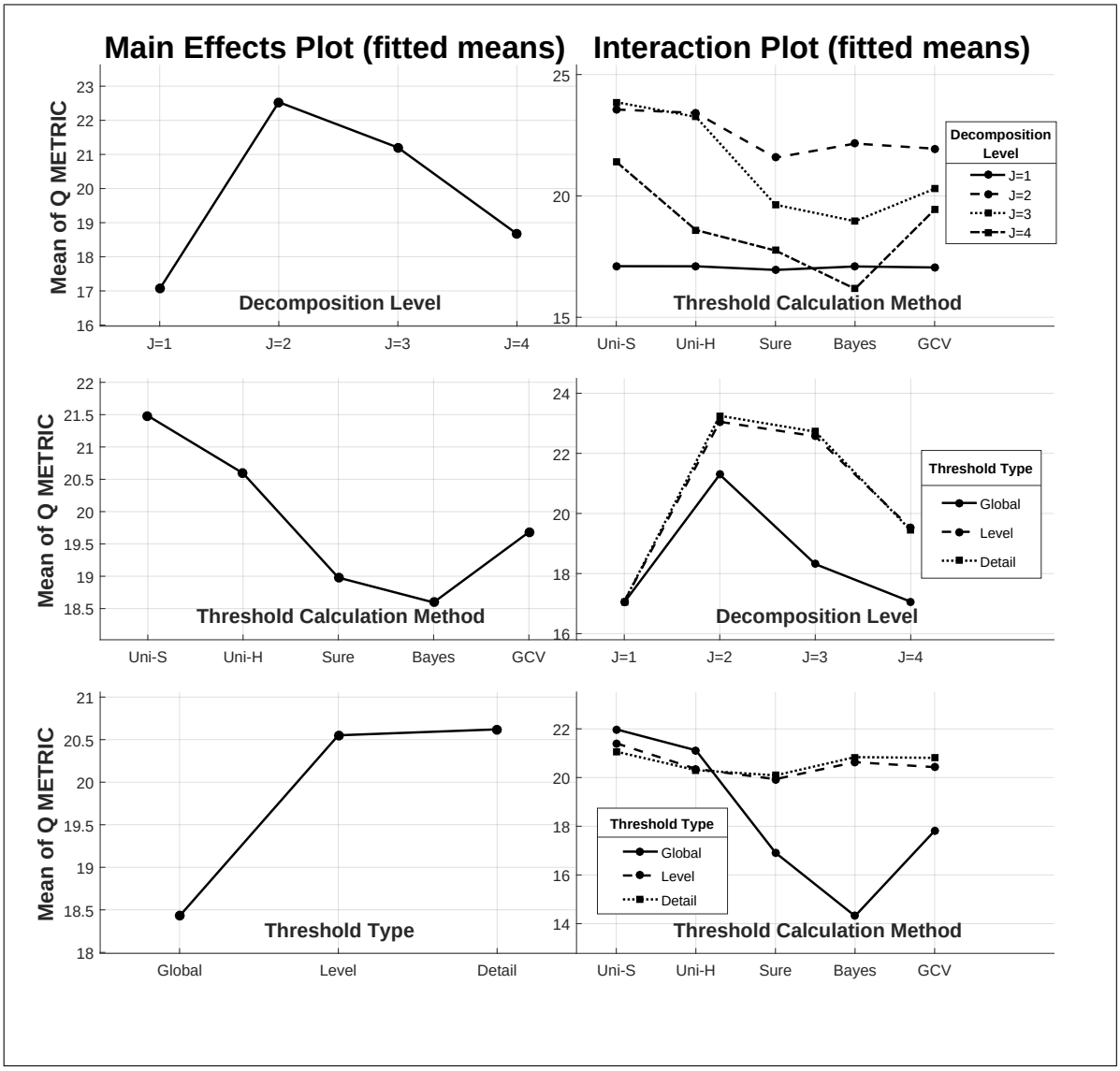

Figure A.12 Q-METRIC: Different level averages of effective factors (left) and interactions (right) for decomposition level, threshold calculation method and threshold type for the **fourth** test case $\sigma = 20$

A.4 ANOVA Mean Plots of SSIM Results

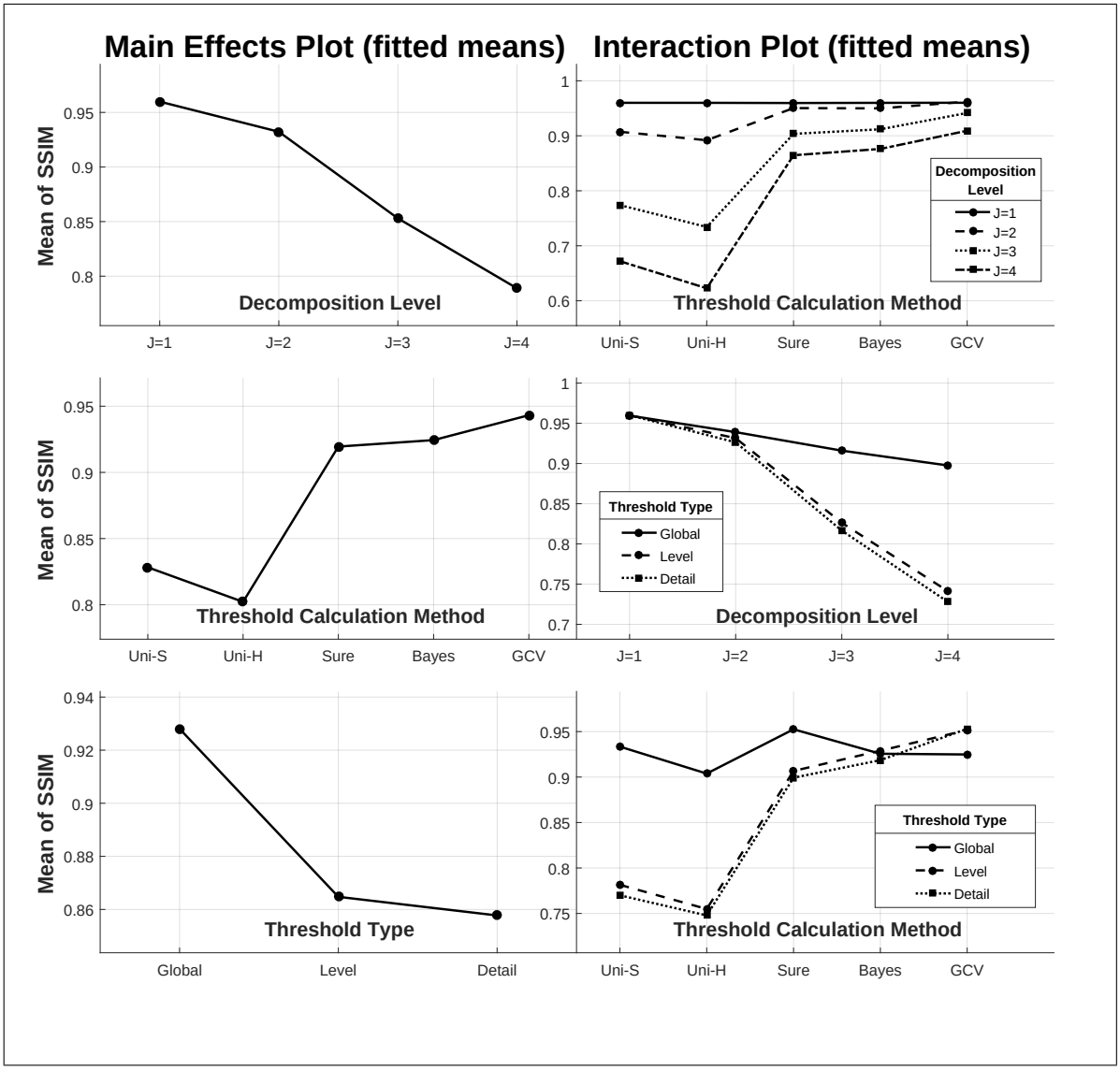

Figure A.13 SSIM: Different level averages of effective factors (left) and interactions (right) for decomposition level, threshold calculation method and threshold type for the **first** test case $\sigma = 5$

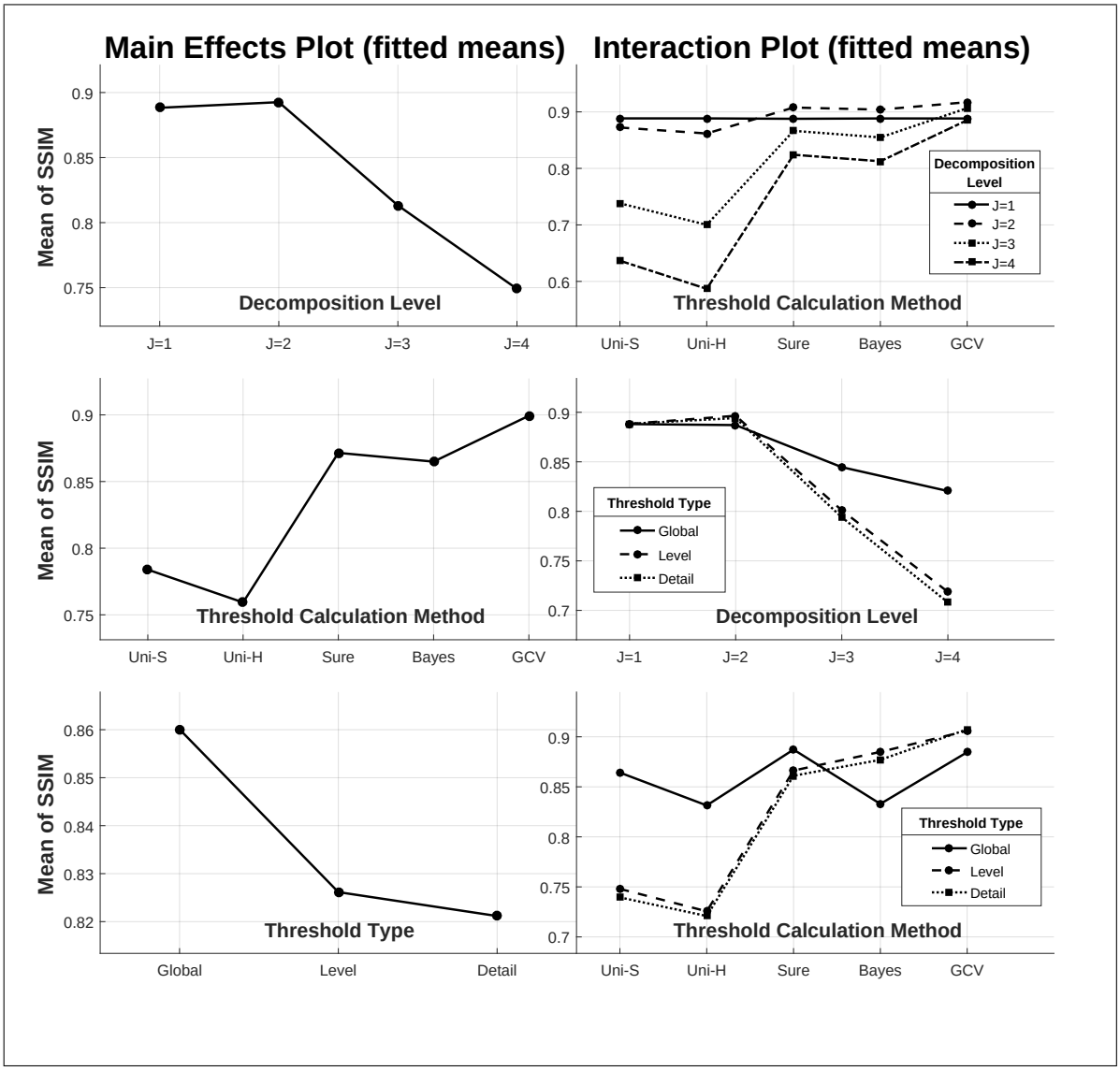

Figure A.14 SSIM: Different level averages of effective factors (left) and interactions (right) for decomposition level, threshold calculation method and threshold type for the **second** test case $\sigma = 10$

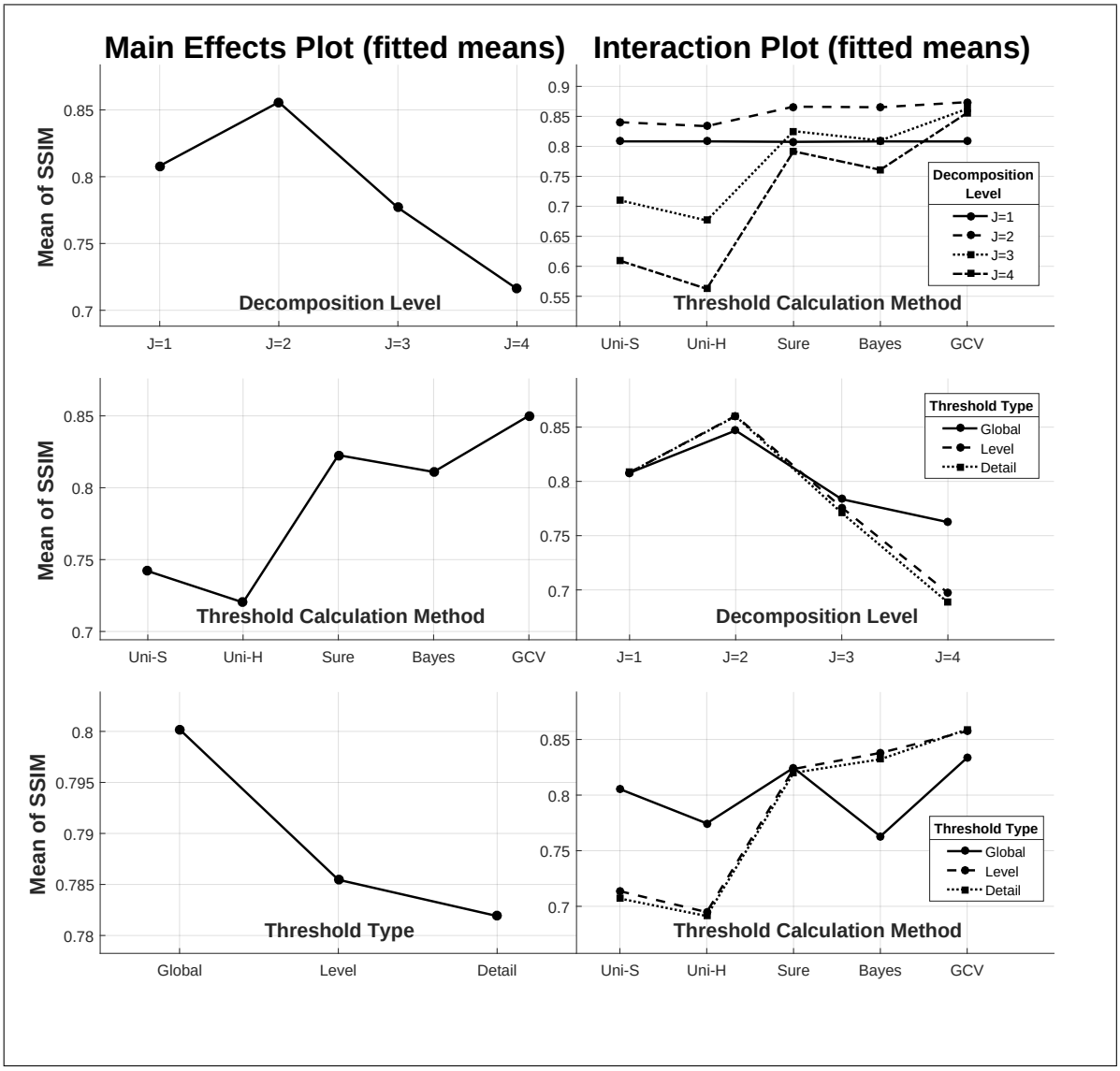

Figure A.15 SSIM: Different level averages of effective factors (left) and interactions (right) for decomposition level, threshold calculation method and threshold type for the **third** test case $\sigma = 15$

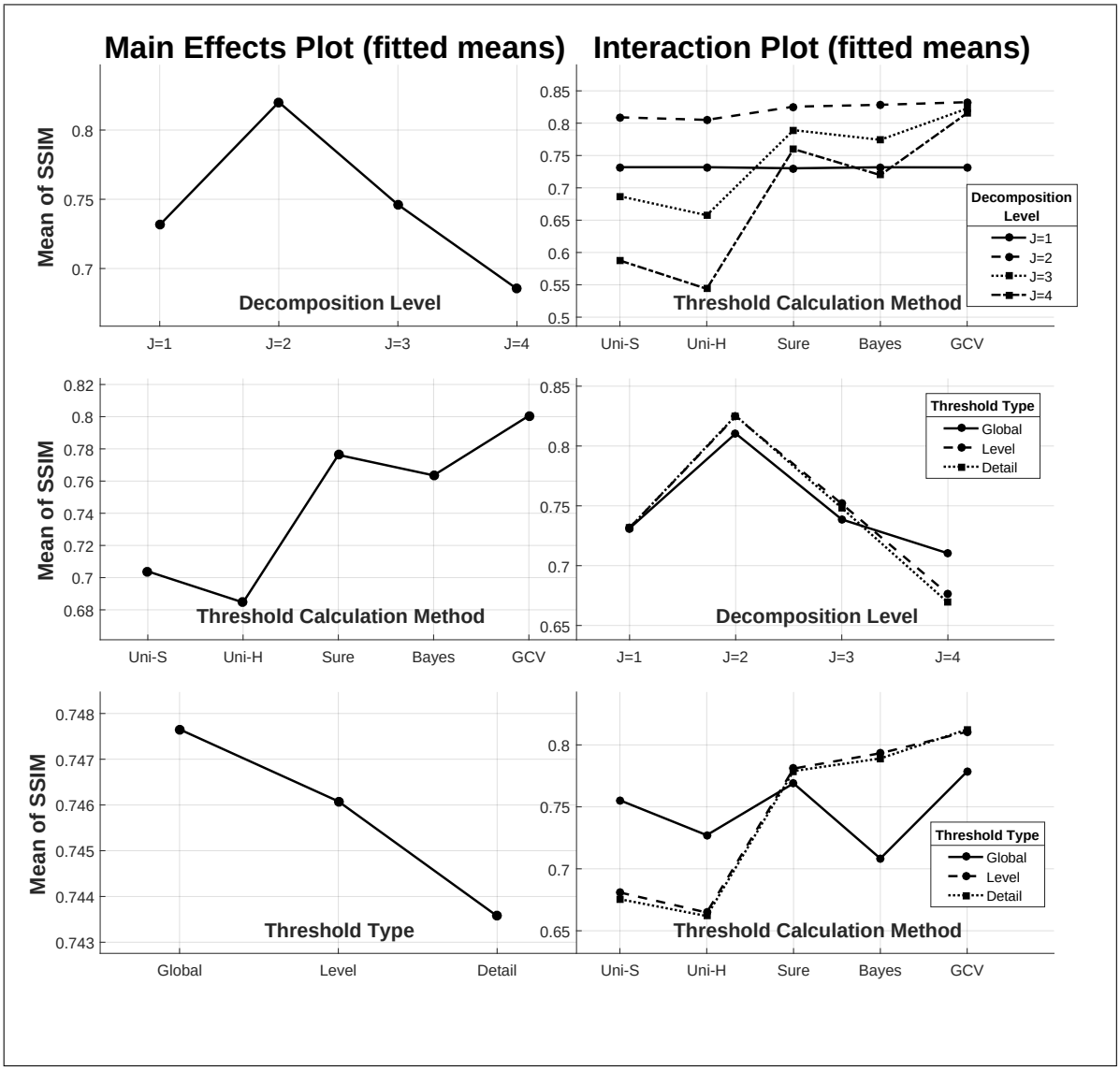

Figure A.16 SSIM: Different level averages of effective factors (left) and interactions (right) for decomposition level, threshold calculation method and threshold type for the **fourth** test case $\sigma = 20$

REFERENCES

1. Pawley, J. B., and B. R. Masters, *Handbook of biological confocal microscopy*, Vol. 13, 2008.

2. Kumar, K., R. Avritscher, Y. Wang, N. Lane, D. C. Madoff, T.-K. Yu, J. W. Uhr, and X. Zhang, "Handheld histology-equivalent sectioning laser-scanning confocal optical microscope for interventional imaging," *Biomedical microdevices*, Vol. 12, no. 2, pp. 223–233, 2010.

3. Dickensheets, D., and G. Kino, "Micromachined scanning confocal optical microscope," *Optics letters*, Vol. 21, no. 10, pp. 764–766, 1996.

4. Minsky, M., "Memoir on inventing the confocal scanning microscope," *Scanning*, Vol. 10, no. 4, pp. 128–138, 1988.

5. Semwogerere, D., and E. R. Weeks, "Confocal microscopy," *Encyclopedia of Biomaterials and Biomedical Engineering*, pp. 1–10, 2005.

6. Sheppard, C. J., X. Gan, M. Gu, and M. Roy, "Signal-to-noise ratio in confocal microscopes," in *Handbook of biological confocal microscopy*, pp. 442–452, Springer, 2006.

7. Wang, T. C., and N. B. Karayiannis, "Detection of microcalcifications in digital mammograms using wavelets," *Medical Imaging, IEEE Transactions on*, Vol. 17, no. 4, pp. 498–509, 1998.

8. Mihcak, M. K., I. Kozintsev, K. Ramchandran, and P. Moulin, "Low-complexity image denoising based on statistical modeling of wavelet coefficients," *Signal Processing Letters, IEEE*, Vol. 6, no. 12, pp. 300–303, 1999.

9. Lang, M., H. Guo, J. E. Odegard, C. S. Burrus, and R. Wells Jr, "Noise reduction using an undecimated discrete wavelet transform," *Signal Processing Letters, IEEE*, Vol. 3, no. 1, pp. 10–12, 1996.

10. Gençay, R., F. Selçuk, and B. J. Whitcher, *An introduction to wavelets and other filtering methods in finance and economics*, Academic press, 2001.

11. Chang, S. G., B. Yu, and M. Vetterli, "Adaptive wavelet thresholding for image denoising and compression," *Image Processing, IEEE Transactions on*, Vol. 9, no. 9, pp. 1532–1546, 2000.

12. Bultheel, A., "Wavelets with applications in signal and image processing," *Septiembre de*, pp. 157–162, 2003.

13. Zhu, X., and P. Milanfar, "Automatic parameter selection for denoising algorithms using a no-reference measure of image content," *Image Processing, IEEE Transactions on*, Vol. 19, no. 12, pp. 3116–3132, 2010.

14. Zhu, X., and P. Milanfar, "A no-reference sharpness metric sensitive to blur and noise," in *Quality of Multimedia Experience, 2009. QoMEx 2009. International Workshop on*, pp. 64–69, IEEE, 2009.

15. Roodt, Y., P. E. Robinson, A. Nel, and W. Clarke, "Robust single image noise estimation from approximate local statistics," IAPR, 2012.

16. Pisano, E. D., S. Zong, B. M. Hemminger, M. DeLuca, R. E. Johnston, K. Muller, M. P. Braeuning, and S. M. Pizer, "Contrast limited adaptive histogram equalization image processing to improve the detection of simulated spiculations in dense mammograms," *Journal of Digital imaging*, Vol. 11, no. 4, pp. 193–200, 1998.

17. Pizer, S. M., E. P. Amburn, J. D. Austin, R. Cromartie, A. Geselowitz, T. Greer, B. ter Haar Romeny, J. B. Zimmerman, and K. Zuiderveld, "Adaptive histogram equalization and its variations," *Computer vision, graphics, and image processing*, Vol. 39, no. 3, pp. 355–368, 1987.

18. Zuiderveld, K., "Contrast limited adaptive histogram equalization," in *Graphics gems IV*, pp. 474–485, Academic Press Professional, Inc., 1994.

19. Ooi, C. H., N. S. P. Kong, and H. Ibrahim, "Bi-histogram equalization with a plateau limit for digital image enhancement," *Consumer Electronics, IEEE Transactions on*, Vol. 55, no. 4, pp. 2072–2080, 2009.

20. Kim, Y.-T., "Contrast enhancement using brightness preserving bi-histogram equalization," *Consumer Electronics, IEEE Transactions on*, Vol. 43, no. 1, pp. 1–8, 1997.

21. Chen, S.-D., and A. R. Ramli, "Minimum mean brightness error bi-histogram equalization in contrast enhancement," *Consumer Electronics, IEEE Transactions on*, Vol. 49, no. 4, pp. 1310–1319, 2003.

22. Dima, A., M. Scholz, and K. Obermayer, "Semiautomatic quality determination of 3d confocal microscope scans of neuronal cells denoised by 3d wavelet shrinkage," in *AeroSense'99*, pp. 446–457, International Society for Optics and Photonics, 1999.

23. De Monvel, J. B., S. Le Calvez, and M. Ulfendahl, "Image restoration for confocal microscopy: improving the limits of deconvolution, with application to the visualization of the mammalian hearing organ," *Biophysical Journal*, Vol. 80, no. 5, pp. 2455–2470, 2001.

24. Bernad, G. P., L. Blanc-Faraud, and J. Zerubia, "A restoration method for confocal microscopy using complex wavelet transform," in *Acoustics, Speech, and Signal Processing, 2005. Proceedings.(ICASSP'05). IEEE International Conference on*, Vol. 2, pp. 621–624, IEEE, 2005.

25. Daubechies, I., *et al.*, *Ten lectures on wavelets*, Vol. 61, SIAM, 1992.

26. Mallat, S. G., "A theory for multiresolution signal decomposition: the wavelet representation," *Pattern Analysis and Machine Intelligence, IEEE Transactions on*, Vol. 11, no. 7, pp. 674–693, 1989.

27. Cvetkovic, D., E. D. Übeyli, and I. Cosic, "Wavelet transform feature extraction from human ppg, ecg, and eeg signal responses to elf pemf exposures: A pilot study," *Digital signal processing*, Vol. 18, no. 5, pp. 861–874, 2008.

28. Chun-Lin, L., "A tutorial of the wavelet transform," *NTUEE, Taiwan*, 2010.

29. Ismail, B., and A. Khan, "Image de-noising with a new threshold value using wavelets," *Journal of Data Science*, Vol. 10, pp. 259–270, 2012.

30. Tang, Y. Y., H. Ma, J. Liu, B. F. Li, and D. Xi, "Multiresolution analysis in extraction of reference lines from documents with gray level background," *Pattern Analysis and Machine Intelligence, IEEE Transactions on*, Vol. 19, no. 8, pp. 921–926, 1997.

31. Immerkaer, J., "Fast noise variance estimation," *Computer vision and image understanding*, Vol. 64, no. 2, pp. 300–302, 1996.

32. Liu, X., M. Tanaka, and M. Okutomi, "Noise level estimation using weak textured patches of a single noisy image," in *Image Processing (ICIP), 2012 19th IEEE International Conference on*, pp. 665–668, IEEE, 2012.

33. Liu, X., M. Tanaka, and M. Okutomi, "Single-image noise level estimation for blind denoising," *Image Processing, IEEE Transactions on*, Vol. 22, no. 12, pp. 5226–5237, 2013.

34. "The Cell Image Library, ccm-nodal cells of sprague-dawley rat, cil:48302." `http://www.cellimagelibrary.org/images/48302`. Accessed: 2016-05-27.

35. Ellinas, J., T. Mandadelis, A. Tzortzis, and L. Aslanoglou, "Image de-noising using wavelets," *TEI of Piraeus Applied Research Review*, Vol. 9, no. 1, pp. 97–109, 2004.

36. Guo, Q., and C. Zhang, "A noise reduction approach based on stein?s unbiased risk estimate," *Sci Asia*, Vol. 38, pp. 207–11, 2012.

37. Donoho, D. L., and J. M. Johnstone, "Ideal spatial adaptation by wavelet shrinkage," *Biometrika*, Vol. 81, no. 3, pp. 425–455, 1994.

38. Stein, C. M., "Estimation of the mean of a multivariate normal distribution," *The annals of Statistics*, pp. 1135–1151, 1981.

39. Donoho, D. L., and I. M. Johnstone, "Adapting to unknown smoothness via wavelet shrinkage," *Journal of the american statistical association*, Vol. 90, no. 432, pp. 1200–1224, 1995.

40. Jansen, M., M. Malfait, and A. Bultheel, "Generalized cross validation for wavelet thresholding," *Signal processing*, Vol. 56, no. 1, pp. 33–44, 1997.

41. Jansen, M., and A. Bultheel, "Multiple wavelet threshold estimation by generalized cross validation for images with correlated noise," *Image Processing, IEEE Transactions on*, Vol. 8, no. 7, pp. 947–953, 1999.

42. Gonzalez, R. C., and R. E. Woods, *Digital Image Processing*, Prentice hall, 2nd ed., 2002.

43. Zhang, Y., H. Cheng, J. Huang, and X. Tang, "An effective and objective criterion for evaluating the performance of denoising filters," *Pattern Recognition*, Vol. 45, no. 7, pp. 2743–2757, 2012.

44. Zhang, Y., H. Cheng, J. Huang, and X. Tang, "A novel metric for image denoising algorithms," in *Intelligence Science and Big Data Engineering*, pp. 538–545, Springer, 2013.

45. Sobel, I., and G. Feldman, "A 3x3 isotropic gradient operator for image processing," *a talk at the Stanford Artificial Project in*, pp. 271–272, 1968.

46. Shannon, C. E., "A mathematical theory of communication," *ACM SIGMOBILE Mobile Computing and Communications Review*, Vol. 5, no. 1, pp. 3–55, 2001.

47. Wang, Z., A. C. Bovik, H. R. Sheikh, and E. P. Simoncelli, "Image quality assessment: from error visibility to structural similarity," *Image Processing, IEEE Transactions on*, Vol. 13, no. 4, pp. 600–612, 2004.

48. Saremi, A., T. ElMekkawy, and G. Wang, "Tuning the parameters of a memetic algorithm to solve vehicle routing problem with backhauls using design of experiments," *International Journal of Operations Research*, Vol. 4, no. 4, pp. 206–219, 2007.

49. Luisier, F., T. Blu, B. Forster, and M. Unser, "Which wavelet bases are the best for image denoising?," in *Optics & Photonics 2005*, pp. 59140E–59140E, International Society for Optics and Photonics, 2005.

50. Donoho, D. L., and I. M. Johnstone, "Threshold selection for wavelet shrinkage of noisy data," in *Engineering in Medicine and Biology Society, 1994. Engineering Advances: New Opportunities for Biomedical Engineers. Proceedings of the 16th Annual International Conference of the IEEE*, pp. A24–A25, IEEE, 1994.

51. Wang, Y.-P., Q. Wu, K. R. Castleman, and Z. Xiong, "Chromosome image enhancement using multiscale differential operators," *Medical Imaging, IEEE Transactions on*, Vol. 22, no. 5, pp. 685–693, 2003.

52. Agaian, S. S., K. Panetta, and A. M. Grigoryan, "Transform-based image enhancement algorithms with performance measure," *Image Processing, IEEE Transactions on*, Vol. 10, no. 3, pp. 367–382, 2001.

53. "The Cell Image Library, a portion of dendrite and associated spines from a purkinje neuron of the rat cerebellum, cil:39951." `http://www.cellimagelibrary.org/images/39951`. Accessed: 2016-05-27.

54. "The Cell Image Library, polymerized actin localization in arpc2-distorted2 mutant arabidopsis thaliana leaf trichomes during the transition to branch elongation, cil:13201." `http://www.cellimagelibrary.org/images/13201`. Accessed: 2016-05-27.

55. "The Cell Image Library, hela cells stably expressing bac-encoded gfp-labeled snrnp protein hprp8, cil:26585." `http://www.cellimagelibrary.org/images/26585`. Accessed: 2016-05-27.

56. "The Cell Image Library, cos 7 cell expressing organelle lightstm er-gfp (invitrogen) consisting of the signal sequence of the er protein calreticulin and a kdel retention sequence, cil:722." `http://www.cellimagelibrary.org/images/722`. Accessed: 2016-05-27.